

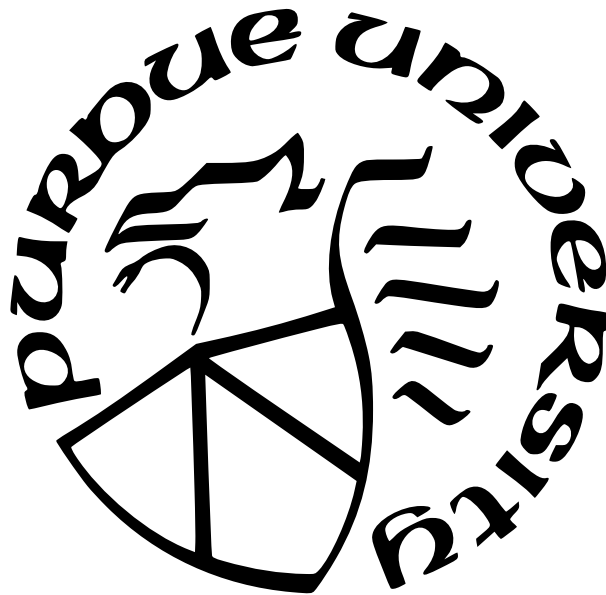
**DEVICE DESIGN AND CHARACTERIZATION FOR SILICON
NITRIDE ON-CHIP OPTICAL FREQUENCY COMB
APPLICATIONS**

by
Cong Wang

A Dissertation

*Submitted to the Faculty of Purdue University
In Partial Fulfillment of the Requirements for the degree of*

Doctor of Philosophy



School of Electrical and Computer Engineering

West Lafayette, Indiana

December 2021

**THE PURDUE UNIVERSITY GRADUATE SCHOOL
STATEMENT OF COMMITTEE APPROVAL**

Dr. Andrew M. Weiner, Chair

School of Electrical and Computer Engineering

Dr. Minghao Qi

School of Electrical and Computer Engineering

Dr. Zubin Jacob

School of Electrical and Computer Engineering

Dr. Tongcang Li

Department of Physics and Astronomy

Approved by:

Dr. Dimitrios Peroulis

Dedicated to my beloved parents.

ACKNOWLEDGMENTS

First and foremost, I am deeply grateful to my thesis advisor, Professor Andrew M. Weiner for his support and encouragement in my Ph.D work. And I would like to express my sincere gratitude to Dr. Daniel E. Leaird and Professor Minghao Qi for the help in the research. I would also like to thank Professor Zubin Jacob and Professor Tongcang Li for the instructions and comments on the thesis work.

Additionally, I would like to extend my sincere thanks to all the members in Ultrafast Optics and Optical Fiber Communications Laboratory; Dr. Xiaoxiao Xue, Dr. Pei-Hsun Wang, Dr. Chengying Bao, Dr. Jose Jaramillo-Villegas, Dr. Andrew Metcalf, Dr. Yang Liu, Eric Topel, Dr. Ogaga Odele, Dr. Bohao Liu, Dr. Poolad Imany, Dr. Oscar Sandoval, Ziyun Kong, Keith McKinzie, Dr. Abdullah Al Noman Ovi, Dr. Hsuan-Hao (Peach) Lu, Nathan O'Malley, Dr. Navin Lingaraju, Alexandria Moore, Suparna Seshadri, Karthik V.Myilswamy, Lucas Cohen, Saleha Fatema, Michael Kickbush and Ryan Schneider. I would like to thanks our collaborators from Professor Minghao Qi's group; Dr. Sangsik Kim, Dr. Yi Xuan, Dr. Kyunghun Han, Yun Jo Lee. I would also like to thanks our collaborators from Chalmers University of Technology, Professor Victor Torres-Company , Dr. Zhichao Ye and Marcello Girardi.

Finally, I would like to offer my special thanks to my parents for their support all the time.

TABLE OF CONTENTS

LIST OF TABLES	11
LIST OF FIGURES	12
LIST OF SYMBOLS	16
ABBREVIATIONS	17
ABSTRACT	18
1 INTRODUCTION	20
1.1 Microring Resonators	20
1.1.1 Silicon Nitride Microresonators	20
1.1.2 Light Propagation in the Microring Resonator	22
1.1.3 Free Spectral Range of a Microring Resonator	23
1.1.4 Microring Resonator Waveguide Group Velocity Dispersion	24
1.2 Kerr Frequency Comb	25
1.2.1 Four Wave Mixing in Microresonators	25
1.2.2 Modeling for Comb Generation	27
1.2.3 Lugiato-Lefever Equation	27
1.3 Two Coherent States in Different Dispersion Regimes	28
1.3.1 Bright Soliton in the Anomalous Dispersion Regime	28
1.3.2 Dark Pulse in the Normal Dispersion Regime	29
1.4 Device Design for Microring Resonators	29

1.5	Thesis Outline	30
2	INVESTIGATION OF COHERENT KERR FREQUENCY COMB GENERATION	33
2.1	Dark Pulse Generation	33
2.2	Modeling of Dark Pulse Generation	33
2.2.1	Mode Interaction in the Normal Dispersion Dark Pulse Generation . .	34
2.3	Comb Conversion Efficiency Characterization	36
2.3.1	SiN Microring Device for Normal Dispersion Dark Pulse Generation .	37
2.3.2	Comb Generation	37
2.3.3	Comb Power Characterization	38
2.3.4	Dark Breather	40
2.3.5	Example of Dark Breather	41
2.4	Summary	42
3	INVESTIGATION OF THE THERMAL TUNING OF KERR FREQUENCY COMB	43
3.1	Simulation for Thermal Tuning of On-chip Frequency Comb	43
3.1.1	Thermal Tuning Coefficients	43
3.1.2	Verification of Thermo-optic Coefficient of Waveguide Material . . .	44
3.1.3	Estimation of Thermal Tuning Efficiency of Resonance Frequency based on Simulation	45
3.2	Design and Characterization of Microheater	47
3.2.1	Structure of On-chip Microheater	49

3.2.2	Characterization of Microheater Resistance	49
3.2.3	Characterization of Resonance Frequency Tuning Efficiency: Titanium Heater	50
3.2.4	Characterization of Resonance Frequency Tuning Efficiency: Platinum Heater	52
3.2.5	Characterization of Resonance Frequency Tuning Efficiency: Heater Width	54
3.3	Characterization of On-chip Microheater Reliability	55
3.3.1	Failure of On-chip Microheater: Type I	56
3.3.2	Failure of On-chip Microheater: Type II	56
3.3.3	Approaches to Increase Heater Reliability	57
3.3.4	Improvement of Heater Uniformity	58
4	DISPERSION ENGINEERING FOR OCTAVE-SPANNING SOLITON GENERATION	61
4.1	Stabilization of Kerr Frequency Comb	61
4.1.1	f-2f Self-referencing	62
4.1.2	Towards the on-chip f-2f Self-referencing	62
4.2	Design for Octave-spanning Bandwidth	63
4.2.1	Kerr Comb Bandwidth	63
4.2.2	Ring Waveguide Design Parameters	63
4.2.3	Ring Waveguide Simulation for GVD Optimization	64

4.2.4	Ring Waveguide Cross Section Dimensions	65
4.2.5	Ring Radius	66
4.2.6	Summary	68
4.3	Dispersive Wave Generation to Enhance Comb Line Amplitude	68
4.3.1	Dispersive Wave for f-2f self-referencing	69
4.3.2	Dispersive Wave Generation in Ring Resonator	70
4.3.3	Effect of Refractive Index	70
4.3.4	Waveguide Design for Dispersive Wave Generation	71
4.4	Design for Low Carrier Offset Frequency	73
4.4.1	Waveguide Design Targeting Low Carrier Offset Frequency	73
4.4.2	Offset Between Simulated and Experimental Device Parameters	77
4.5	Design Parameter Sensitivity for Dispersion Engineering	78
4.5.1	Parameter Sensitivity in the device design	78
4.5.2	Compensations for the Offset Between Simulation and Fabrication	79
4.6	Realization of Octave-spanning Kerr Soliton	80
4.6.1	Device for Octave-spanning Frequency Comb Generation	80
4.6.2	Octave-spanning Soliton Generation	82
4.7	Discussion	82
5	OPTICAL DIVISION OF OCTAVE-SPANNING SOLITON ON AN ALL-SILICON NITRIDE PLATFORM	85

5.1	Optical Division of a Large Repetition Rate Comb	85
5.1.1	Conventional Optical Division Methods	85
5.1.2	Integrated Optical Division Methods	85
5.1.3	Integrated Optical Division on All-SiN Platform	86
5.2	Optical Division Scheme with a Low Repetition Rate Auxiliary Ring	88
5.2.1	Retrieving Large Repetition Rate via Beat Signal	88
5.3	Devices for Optical Division	88
5.3.1	Device1: Octave-spanning Device	88
5.3.2	Device2: 25 GHz Device	89
5.4	Demonstration of Optical Division of 900 GHz Octave-spanning soliton with a 25 GHz soliton	90
5.4.1	Simultaneous Soliton Generation via Fast Pump Tuning	90
5.4.2	Overlap Beat Detection	91
5.4.3	Verification of Repetition Rate via Electric-optic Modulation	92
5.5	Summary	94
6	OPTICAL DIVISION OF OCTAVE-SPANNING SOLITON WITH A VERNIER BROADBAND SOLITON	95
6.1	Optical Division with a Vernier Soliton	95
6.1.1	Retrieve Repetition Rate via Beat Notes	95
6.1.2	Choice of Repetition Rate Difference	96
6.2	Device Design for Vernier Pairs	98

6.2.1	Requirements for Vernier Pairs	98
6.2.2	Waveguide Dimension for Vernier Pairs	98
6.2.3	Ring Radius for Vernier Ring	99
6.3	Vernier Soliton Generation	99
6.3.1	Heater Parameters Characterization	100
6.3.2	Simultaneous Soliton Generation	102
6.3.3	Measurement of Overlap Beat	102
6.4	Discussion	104
6.4.1	Comparison Between Two Optical Division Schemes	104
7	SUMMARY	107
7.1	Summary	107
7.2	Outlook	108
	REFERENCES	109
	PUBLICATIONS	117

LIST OF TABLES

2.1	Experimental Measured Mode Interaction Parameter Values for Different Modes on a 230 GHz Repetition Rate Normal Dispersion SiN Microring	35
3.1	Measured and Simulated Parameters for Thermo-optic Coefficients Calculation [51]).	46
3.2	Measured and Estimated Properties of Ti Microheater	51
3.3	Measured and Estimated Properties of Pt Microheater on 1 THz SiN Microring Resonators.	54
3.4	Measured and Estimated Properties of Pt Microheater on 500 GHz SiN Microring Resonators.	54
3.5	Measured and Estimated Properties of the Pt Microheaters on 1 THz SiN Microring Resonators with Different Ring Heater Widths	55
4.1	Comparison of Designed and Measured Repetition Rate of Microring Resonator with $\sim 25 \mu\text{m}$ Radius	78
4.2	Parameters Sensitivity. DW 1: Dispersiv Wave 1. DW 2:Dispersive Wave 2.	79
6.1	Parameters of On-chip Heater	100

LIST OF FIGURES

1.1	Example of a SiN Microring Resonator. (A) Ring waveguide structure. (B) Picture of a 100 μm radius SiN microring.	21
1.2	Schematic diagram of Light Propagation in the Microring Resonator. (1) Input port. (2) Evanescent coupling from bus waveguide to ring waveguide. (3) Light propagates in the ring. (4) Light couples from ring waveguide to bus waveguide. (5) Output port.	23
1.3	Schematic diagram of resonant modes spacing in different dispersion regimes. (a) normal dispersion regime (b) anomalous dispersion regime	25
1.4	Schematic diagram of degenerate FWM and non-degenerate FWM. Red: Pump. Solid Blue: Generated sideband. Dash Blue: Other comb lines.	26
1.5	Examples of soliton simulation result of 230 GHz ring resonator in the different dispersion regime. Left: Bright soliton in the anomalous dispersion regime. Right: Dark soliton in the normal dispersion regime. Upper figure: Time-domain intra-cavity waveform. Bottom figure: Frequency domain intra-cavity waveform.	28
1.6	Example of Bright Soliton. (a) Time domain and frequency domain spectral of single soliton (b) Time domain and frequency domain spectral of two solitons	29
1.7	Sample Layout for Microring Resonators and Location Markers	31
2.1	Examples of Mode Interaction Induced Resonance Frequency Shift. Red Dots: Resonance frequency offset from equal distance grid. Blue Curve: Parabolic fitting results.	34
2.2	Examples of Comparison Between Simulated Optical Spectrum and Experimental Results	36
2.3	Device Layout for Normal Dispersion Dark Pulse Generation [40].	38
2.4	Mode Interaction Position. Blue line represents the fundamental TE mode and green line indicates the higher TE mode. The red circle is the mode interaction region we choose to pump [40].	39
2.5	Comb spectrum. (a) Comb evolution process while tuning into resonance. The left side shows the optical spectra and the right side shows the intensity noise spectra. Blue lines show the intensity noise of comb and red lines show the background when pump off-resonance. State 1: Initiation of Comb. State 2: Single FSR low noise comb. State 3: 2 FSR low noise comb.. (b) The final comb state, Upper: comb spectrum at the through port, Bottom: comb spectrum at the drop-port.[40]	40

2.6	Comb spectrum and RF signal measurement. (a) Coherent dark pulse state. (b) Breather state. (c) Comb RF spectrum measured by electrical spectrum analyzer. (d) Single line power breathing	41
3.1	Schematic Diagram of Calculating Simulated Resonance Frequency	47
3.2	Simulation of Resonance Frequency and Repetition Rate Tuning with Temperature Dependent Refractive Indices	48
3.3	Example Layout of Micro Heater. Orange: microheater. Blue: Waveguide	49
3.4	Example Layout of Test Structure for Contact Resistance Estimation	50
3.5	Resonance Shift from Blue to Red by Microheater with Increasing Voltage (Devices fabricated by Abdullah Al Noman)	51
3.6	Degradation Process of Ti Microheater as the Voltage Increases. df represents the corresponding resonance frequency shift.	52
3.7	Resonance Shift by Microheater with Different Voltage of Pt Microheater on a 500 GHz SiN Ring resonator (Devices fabricated by Abdullah Al Noman)	53
3.8	Resonance Shift by Microheater with Different Voltage of Pt Microheater on a 1 THz SiN Ring resonator (Devices fabricated by Abdullah Al Noman)	53
3.9	Microheater Layout with Different Ring Heater Widths	54
3.10	Degradation of Microheater While Heating	57
3.11	Corresponding Thermal Tuning Range During the Degradation of Microheater	58
3.12	Scheme of Heater Metal Deposition	59
3.13	Revised Microheater Design to Minimize Overlap Between SiN Waveguide and Heater	60
4.1	Examples of Important Parameters of Ring Waveguide in Device Design. (a) Example of waveguide core. (b) Definition of ring radius.	63
4.2	Map for GVD Value vs. SiN Waveguide dimension for Waveguide with large bending radius. The intensity color plot represents GVD, D (ps/nm/km).	65
4.3	D_2 for Different Film Thickness and Ring Waveguide Widths	65
4.4	Waveguide Loss Comparison Between TE0 mode and TE1 mode. (a) Ring Waveguide Dimension (740 nm (thick) \times 2000 nm (wide) (b) Ring Waveguide Dimension (740 nm (thick) \times 1600 nm (wide)	66
4.5	Map for GVD Value vs. SiN Waveguide dimension for Waveguide with 45 μ m ring radius. The intensity color plot represents GVD, D (ps/nm/km).	67
4.6	Map for GVD Value vs. SiN Waveguide dimension for Waveguide with 25 μ m ring radius. The intensity color plot represents GVD, D (ps/nm/km).	68

4.7	Optical Spectra of Bright Soliton with or without Dispersive Wave. (a) Bright soliton without dispersive wave (b) Bright soliton with dispersive wave. . . .	69
4.8	Phase Matching Condition for Simulations with Different SiO ₂ Refractive Index	72
4.9	Phase Matching Condition for Simulations with Different SiN Refractive Index	73
4.10	Phase Matching Condition Sweep for Dispersive Wave Generation around 740 nm thick and 1600 nm wide SiN Waveguide.	74
4.11	Phase Matching Condition Sweep for Dispersive Wave Generation around 745 nm thick and 1600 nm wide SiN Waveguide.	74
4.12	Phase Matching Condition Sweep for Dispersive Wave Generation for 680 nm thick waveguide with large bending radius	75
4.13	Phase Matching Condition Sweep for Dispersive Wave Generation for 690 nm thick waveguide with large bending radius	75
4.14	Simulated Pump Parameters vs. Ring Radius. (a) Resonance Frequency of the Mode Closest to 1550 nm vs. Ring Radius. (b) FSR of corresponding resonance vs. Ring Radius. (c) Carrier offset frequency vs. Ring Radius. . .	76
4.15	SiN Wafer Thickness Map. (a) Measured thickness across the wafer (b) Chip Distribution Locations on the SiN wafer. The thickness map is measured by Abdullah Al Noman	80
4.16	Chaotic Broadband Frequency Comb Generated on SiN Microring Resonators Wafer 335. The devices are fabricate by Zhichao Ye (Chalmers University of Technology). (Image courtesy: Mohammed S. Alshaykh)	81
4.17	Octave-spanning Solitons Generated on Various of SiN Devices (Image courtesy: Nathan O'Malley)	83
4.18	Octave-spanning Solitons Generated on Various of SiN Devices around Succeeded Parameters in Last Fabrication Run (Devices Fabricated by Marcello Girardi)	84
5.1	Conventional Schemes of Optical Division. (a) Electro-optic modulation of a frequency comb via a low repetition rate RF modulation signal. (b) Beat frequency comb with a low repetition rate fiber-based frequency comb	86
5.2	Overlap for Octave-spanning Comb and Auxiliary Comb with Common Pump	87
5.3	Image of SiN Microring Resonator for Optical Division of Octave-spanning Soliton Fabricated by Zhichao Ye. Left: Device 1 (900 GHz SiN Microring). Right: Device 2 (25 GHz SiN Microring) [65].	90

5.4	Set-up for optical division with a low repetition rate microcomb. TLS: tunable laser. SSB: single-sideband. VCO: voltage control oscillator. AWG: arbitrary waveform generator. PC: polarization controller. Amp: optical amplifier. CWDM: coarse wavelength division multiplexer. DWDM: dense wavelength division multiplexer.	91
5.5	Optical Spectra of Simultaneous Pumping Solitons. Blue: Octave-spanning soliton. Red: Low repetition rate soliton	92
5.6	Electric Spectra of Beat notes. a) Measurement of repetition rate of 25 GHz soliton b) Measurement of overlap beat note between Octave-spanning soliton and 25 GHz soliton [65].	93
5.7	Set-up for EO Comb Verification. CH: channel port of CWDM. REF: reflecting port of CWDM. BPF: bandpass filter. PD: photodetector. ESA: electric spectrum analyzer.	93
6.1	Vernier Approach of Optical Division. Blue: Comb 1 (Octave-spanning comb). Red: Comb 2 (Auxiliary Comb) (a) Low frequency overlap between two combs. (b) High frequency overlap between two combs. (c) Optical spectra example of two combs	96
6.2	Repetition Rate Difference vs. Overlap Wavelength. The red dash line is the repetition rate we choose.	97
6.3	Choosing the Design Parameters of Vernier Pairs when Device 1 is chosen as 738 nm × 1620 nm. The device 1 is designed for octave-spanning soliton generation. The device 2 is designed for a corresponding Vernier ring.	100
6.4	SiN Microring With Platinum Heater Fabricated by Zhichao Ye (Chalmers University of Technology)	101
6.5	Schematic Diagram of the experimental setup of the Vernier beat measurement.	103
6.6	Measurement Results of Vernier Solitons. a) the optical spectra of two Vernier solitons (blue: comb 1, red: comb 2) b) electrical spectrum of df_{rep} . c) Electrical spectrum of the overlap beat d) Overlap beat of the EO comb verification[69]	104
6.7	Two Schemes of Optical Division. a) Optical division with a low repetition rate narrow soliton. b) Optical division with a high repetition rate broadband soliton. Blue: Comb 1 (Octave-spanning Comb). Red: Comb 2 (Auxiliary Comb).	105

LIST OF SYMBOLS

c	Velocity of Light in Vacuum
D	Dispersion Coefficient
f_{ceo}	Carrier Envelope Offset Frequency
f_{res}	Resonance Frequency
f_{rep}	Repetition Rate
H_h	Ring Heater Height
L	Cavity Length
$n_{cladding}$	Refractive Index of Waveguide Cladding
n_{core}	Refractive Index of Waveguide Core
n_{eff}	Effective Index
n_g	Group Index
P_E	Electric Power
Q	Quality Factor
S_h	Ring Heater Cross Section Area
T	Temperature
v_g	Group Velocity
W_h	Ring Heater Width
α	Loss Coefficient
γ	Nonlinear Coefficient
η	Comb Power Conversion Efficiency
μ	Mode Number
ω	Angular Frequency
κ	Coupling Coefficient

ABBREVIATIONS

AlN	Aluminium Nitride
BPF	Bandpass Filter
CW	Continuous-wave
CWDM	Coarse Wavelength Division Multiplexer
DWDM	Dense Wavelength Division Multiplexer
E-beam	Electric Beam Lithography
ESA	Electrical Spectrum Analyzer
FSR	Free Spectral Range
FWM	Four-wave mixing
GVD	Group Velocity Dispersion
LLE	Lugiato-Lefever Equation
LNA	Low Noise Amplifier
MRR	Microring Resonator
PC	Polarization Controller
PD	Photo Detector
PDE	Finite-Difference Eigenmode
Pt	Platinum
RF	Radio Frequency
SHG	Second-harmonic Generation
Si	Silicon
SiN	Silicon Nitride
SiO ₂	Silicon Dioxide
TE	Transverse Electric
Ti	Titanium
TM	Transverse Magnetic
WDM	Wavelength Division Multiplexing
WGM	Whispering-gallery Mode

ABSTRACT

Kerr frequency comb, a sequence of equally spaced sharp lines in frequency domain generated via four-wave mixing process, has multiple applications such as spectroscopy, metrology, and atomic clocks. Conventional frequency combs generated from mode-locked laser have the limitations of low repetition rate and large volume. One novel platform, silicon nitride (SiN) microring resonator (MRR), can overcome such disadvantages. The SiN MRR is a low loss waveguide resonator and has good reliability and capacity for on-chip integration, which enables a portable solution for Kerr frequency comb.

This thesis focuses on the design and characterization of the SiN MRR to optimize the important performance characteristics for the applications.

In Kerr comb applications, phase coherence between the comb lines is required to eliminate unwanted signals in the systems. Therefore, the investigation of the coherent state in MRR based comb generation can benefit the development of comb generation techniques. In particular, dark pulses exhibit much higher comb conversion efficiency than the single soliton combs.

The tunability of Kerr comb is another important performance characteristic of the applications, which is useful for multiple applications, such as matching the comb line spacing to the wavelength multiplexing grid for coherent communication or aligning the on-chip laser wavelength and MRR resonance frequency during the integration. The theoretic analysis of thermal tuning and experimental characterization of resonance frequency tuning via an on-chip microheater are performed in this thesis to explore the thermal tuning efficiency and its limitation.

Another important performance characteristics of the frequency comb is the comb bandwidth. Large bandwidth comb will be beneficial for application like dual comb spectroscopy. In addition, octave-spanning Kerr comb is desired due to its capacity of f - $2f$ self-referencing for comb line frequencies stabilization for the applications like atomic clocks. To demonstrate on-chip octave-spanning Kerr soliton, the dispersion engineering is utilized in the device design to optimize the pump dispersion and dispersive wave generation simultaneously. The octave-spanning solitons are achieved on SiN MRRs with around 900 GHz repetition rate.

Finally, two optical division approaches are demonstrated to read out the large repetition rate of the octave-spanning soliton on all-SiN platform with auxiliary combs to enable the locking of undetectable repetition rate with less complexity in the fabrication and integration. The first approach uses a 25 GHz soliton; whose repetition rate is directly detectable via a photodiode. The second approach employs a Vernier scheme with an 880 GHz soliton to provide an alternative optical division scheme with lower requirements in fabrication ultra-high Q MRRs. The divided repetition rate can be locked to enable the fully stabilization of frequency comb to provide an on-chip high stability and low noise frequency comb source.

1. INTRODUCTION

The optical frequency comb, a set of precisely equidistant sharp lines in the frequency domain, can serve as a stable reference source for metrology [1], [2], atomic clocks [3], or a light source for wavelength division multiplexing (WDM) applications such as long-haul applications [4]–[6], radio frequency (RF) filtering [7], [8] and light detection and ranging (LiDAR) [9], [10].

In the past 30 years, mode-locked lasers have been intensely studied for comb generation [11]–[15]. However, the utilization of individual comb lines is difficult to realize since frequency combs generated by mode-locked laser are difficult to achieve GHz-level large repetition rates (f_{rep}). Additionally, the size and complexity of the mode-locked laser systems limit the employment of combs outside the laboratory. The recent progresses in integrated photonics components enable the fabrication of low loss microresonators, providing a new path to overcome the two major concerns of a portable frequency comb source; the large volume and high power.

1.1 Microring Resonators

1.1.1 Silicon Nitride Microresonators

Microcavity resonators are a new strategy for chip-scale coherent frequency comb generation. There are two main types of microresonators, whispering-gallery mode (WGM) resonators and microring resonators (MRR).

In WGM resonators such as microtoroids [16] and microdisk [17], [18], light is coupled to the WGM resonators through tapered optical fibers. Then the waves are guided along the circle cavity by total internal reflection.

On the other hand, microring resonators are comprised of a micrometer scale transmission bus waveguide coupled with a closed waveguide loop (ring waveguide). Light is confined in the waveguide due to the refractive index difference between core and cladding. When light is pumped into the MRR bus waveguide, a fraction of the light can couple to the ring waveguide through evanescent coupling.

In these platforms, the light can build up in the cavity due to ultra low loss in the cavity. Comb generation is based on a nonlinear parametric process, four wave mixing (FWM), and on the combination of the optical Kerr effect and dispersion to manipulate the phase matching condition.

For the MRR, the ring and bus waveguide are fixed in the same plane which allows integration with other devices such as on-chip pulse-shaper or on-chip laser. Therefore, we focus on the MRR because of its capability of on-chip integration.

A MRR can be made of several materials, such as Silicon Nitride (SiN) [19], Silicon (Si) [20], Lithium Niobate (LN) [21] and Aluminum Nitride (AlN) [22]. In particular, SiN exhibits low loss feature which can enable >10 million quality factor [23]–[26] and is CMOS-compatible. These features make SiN a promising material for on-chip microcomb generation.

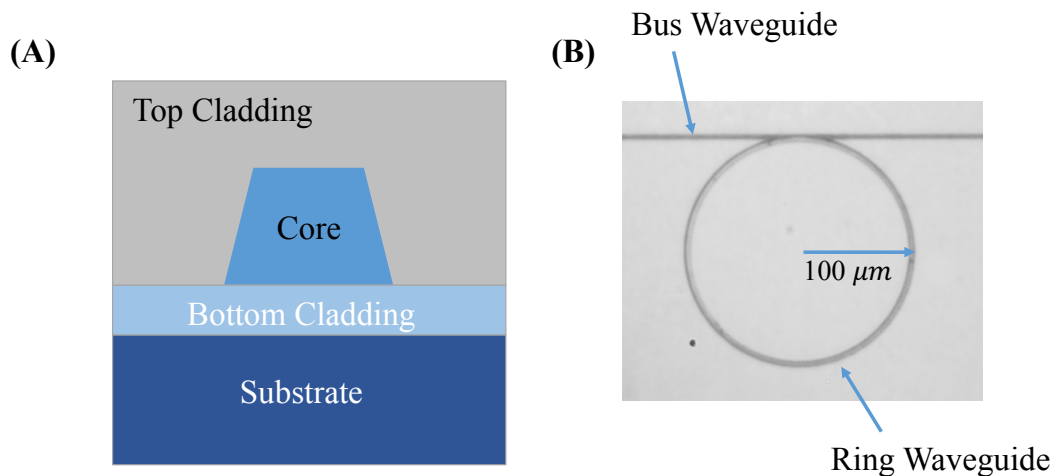


Figure 1.1. Example of a SiN Microring Resonator. (A) Ring waveguide structure. (B) Picture of a $100\ \mu\text{m}$ radius SiN microring.

Fig. 1.1(A) shows a typical waveguide cross section of a SiN MRR which consists of SiO_2 or air top cladding, SiN core, SiO_2 bottom cladding, and Si substrate. When the top cladding is SiO_2 , the advantages are good reliability and the capability of heater deposition, which enables the tunability of frequency combs. When the top cladding is air, the advantages are

easier fabrication process and better light confinement due to the high contrast of refractive index between SiN ($n \approx 2$ near 1550 nm) and air ($n = 1$).

Fig. 1.1(B) shows a photo taken of a 100 μm radius SiN Microring under an optical microscope. The straight line is the bus waveguide and the ring is the ring resonator.

It is worth mentioning that the shape of the ring waveguide does not need to be a circle. Any shape that is a closed loop allowing low loss propagation of light is feasible.

1.1.2 Light Propagation in the Microring Resonator

Fig. 1.2 shows a schematic diagram of light propagation in the microring resonator in 5 steps.

1. The pump light is coupled to the input port of the bus waveguide via a tapered and lensed fiber with a fiber-waveguide insertion loss. In SiN waveguide, the insertion loss is typically around 2 to 4 dB per facet.
2. The light is coupled to ring waveguide via evanescent coupling. The coupling strength is described via coupling coefficient (κ_e^2) or coupling quality factor (Q_e).
3. The light is propagating in the ring resonator. Due to the low propagation loss of the ring waveguide, the photon lifetime is long enough to allow the build up of intracavity power of the resonance modes. The propagation loss is described via intrinsic loss (κ_i^2) or intrinsic quality factor (Q_i).
4. The light is coupled back to bus waveguide via evanescent coupling
5. The output light is coupled from waveguide to output fiber.

Typically, the ring waveguide and bus waveguide are symmetric. The coupling between ring waveguide and bus waveguide in step 2 and step 4 are of the same value. When $\kappa_e^2 < \kappa_i^2$, the ring and bus waveguide is under-coupled. When $\kappa_e^2 > \kappa_i^2$, the ring and bus waveguide is over-coupled. When $\kappa_e^2 = \kappa_i^2$, the ring and bus waveguide is critical-coupled and the resonance modes would exhibit the highest extinction ratio.

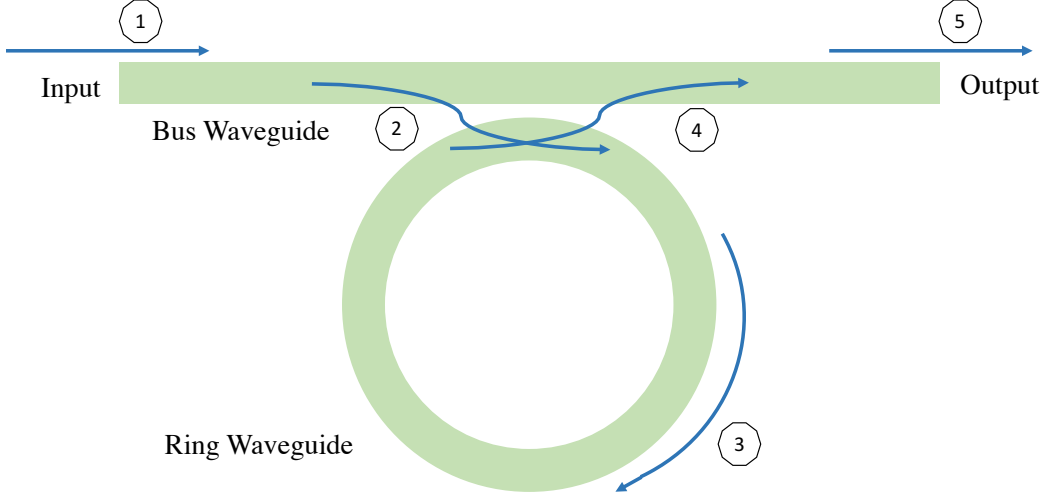


Figure 1.2. Schematic diagram of Light Propagation in the Microring Resonator. (1) Input port. (2) Evanescent coupling from bus waveguide to ring waveguide. (3) Light propagates in the ring. (4) Light couples from ring waveguide to bus waveguide. (5) Output port.

1.1.3 Free Spectral Range of a Microring Resonator

Free spectral range is the spacing between two neighboring modes in the resonator. The repetition rate (f_{rep}) of the generated frequency comb is the spacing between two frequency comb lines, which is determined by the FSR at pump frequency (f_{res}). f_{rep} can be calculated as Eq. 1.1. c , n_g , L represents the speed of light in vacuum, the waveguide group index and the cavity length, respectively.

$$f_{rep} = \frac{c}{n_g L} \quad (1.1)$$

For circle-shape ring resonator, the cavity length is $2\pi R_{ring}$, where R_{ring} is the ring radius. Therefore, for a given waveguide dimension, we can simulate the corresponding group index and then calculate the required ring radius.

During the comb generation process, the repetition rate can be modified due to different pump power and pump detuning (a frequency difference between pump frequency and

resonance frequency) [27]. Then the comb repetition rate would be different than the ring resonance FSR.

The frequency of a comb line can be expressed as $f_{res} \pm m \times f_{rep}$, where m represents the relative mode number to the pump mode. Alternatively, it can be written as $f_{ceo} + n \times f_{rep}$, where f_{ceo} is the carrier offset frequency. f_{ceo} represents the offset of a resonance modes to the equal spacing grid.

1.1.4 Microring Resonator Waveguide Group Velocity Dispersion

The value of a microring resonator FSR is not a constant at different wavelengths due to the wavelength dependent waveguide indices. Light of different frequency propagates with different speed in the optical waveguide, which is the dispersion of the waveguide. The dispersion relationship can be expressed as Eq. 1.2 [28].

$$\beta(\omega_1) = \beta(\omega_0) + \frac{\partial\beta}{\partial\omega}(\omega_1 - \omega_0) + \frac{1}{2!} \frac{\partial^2\beta}{\partial\omega^2}(\omega_1 - \omega_0)^2 + \frac{1}{3!} \frac{\partial^3\beta}{\partial\omega^3}(\omega_1 - \omega_0)^3 + \dots \quad (1.2)$$

In Eq. 1.2, $\beta(\omega_1)$ is the propagation constant of the resonances. ω_0 is the pump frequency and ω_1 is the angular frequency of a resonance in the mode family that ω_0 belongs to.

The derivative β_n satisfies the relation $\beta_n = \frac{\partial^n\beta}{\partial\omega^n}$. In particular, $\beta_1 = \frac{\partial\beta}{\partial\omega}$ is equal to $1/v_g$ (v_g is the group velocity at frequency ω_0) and β_2 is the derivative of group velocity. We call β_2 group velocity dispersions (GVD). GVD can also be expressed as a dispersion parameter D [28] as Eq. 1.4 .

$$\frac{\partial^2\beta}{\partial\omega^2} = \frac{\partial(\frac{1}{v_g})}{\partial\omega} = \frac{1}{c} \cdot \frac{\partial n_g}{\partial\omega} \quad (1.3)$$

$$D = \frac{\partial(v_g^{-1})}{\partial\lambda} = \frac{-2\pi c\beta_2}{\lambda^2} = \frac{-\lambda}{c} \frac{d^2n}{d\lambda^2} \quad (1.4)$$

The dispersion can be observed in the resonant modes spacing change along the propagating wavelength Fig. 1.3. In the normal dispersion regime ($\beta_2 > 0$), the group index keeps decreasing when the wavelength increases, therefore the corresponding FSR is increas-

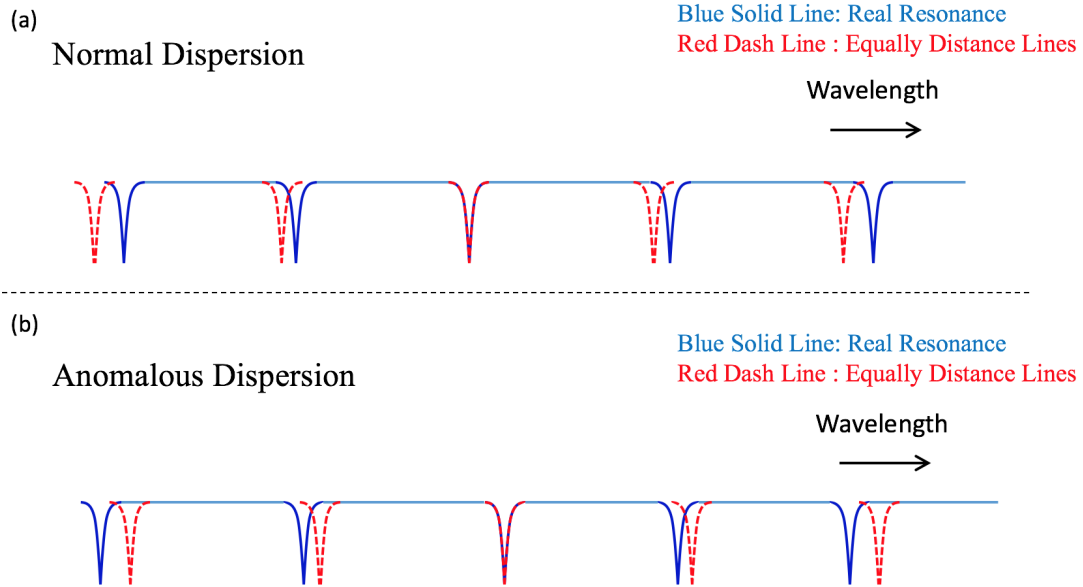


Figure 1.3. Schematic diagram of resonant modes spacing in different dispersion regimes. (a) normal dispersion regime (b) anomalous dispersion regime

ing (Fig. 1.3.(a)). In the anomalous dispersion regime ($\beta_2 < 0$), the FSR is changing in an opposite direction.

1.2 Kerr Frequency Comb

1.2.1 Four Wave Mixing in Microresonators

During the propagation in the ring resonator, the frequency comb can be generated based on four-wave mixing (FWM) process, which is a third-order nonlinear effect (Kerr effect).

When we pump the resonator with a continuous-wave (CW) laser, the comb starts due to degenerate FWM process (see Fig. 1.4 (a)). Two pump photons with identical frequency (ω_0) generate two new photons; one with lower frequency (ω_1) and one with higher frequency (ω_2) to the pump frequency when $2\omega_0 = \omega_1 + \omega_2$ and the phase matching condition are satisfied. Also, the photons from sideband ω_2 and from the pump ω_0 , can generate new frequency components, ω_3 and ω_4 via non-degenerate FWM (See Fig. 1.4 (b)). The cascaded FWM

process leads to the comb generation. Since the frequency comb generation rely on the Kerr effect, the generated comb are called Kerr Frequency comb.

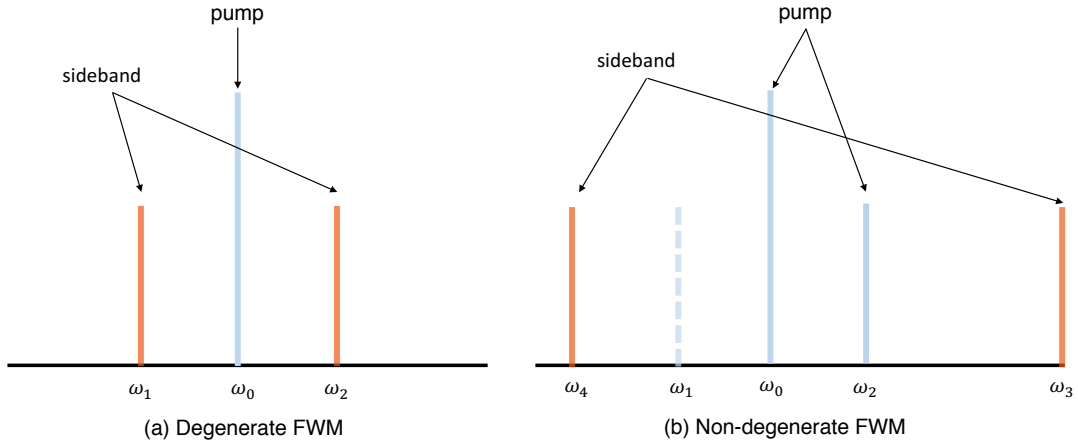


Figure 1.4. Schematic diagram of degenerate FWM and non-degenerate FWM. Red: Pump. Solid Blue: Generated sideband. Dash Blue: Other comb lines.

During the whole FWM process, the phase of each comb line is randomly selected with the exception of two cases. The first is when only degenerate FWM is involved in the process, we call this a type I comb [29]. Otherwise, we call this a type II comb, which is generated by the combination of degenerate and non-degenerate FWM during the process.

For type II comb, the phase coherence relies on the mode-locking transition based on the equilibrium between dispersion, nonlinearity, input power and loss in the condition of certain input power, pump detuning (the offset between pump frequency and resonance frequency).

There are mainly two coherent states in the Kerr microcomb generated in different dispersion regimes. We will discuss the details of those two coherent states later in this chapter.

The mechanisms for comb excitation in the different dispersion regimes are different. Here we mainly discuss soft excitation, where the comb arises from noise without the presence of a pump photon in the cavity [30]. In the anomalous dispersion regime, where $\beta_2 < 0$, comb generation starts due to modulation instability. The position of the first sideband is

determined by the balance between group velocity dispersion (GVD) and the nonlinear Kerr effect. In the normal dispersion regime, where $\beta_2 > 0$, comb generation starts due to mode interaction [31] or structure [32] induced local dispersion change or injection-locking [33].

1.2.2 Modeling for Comb Generation

To make an estimation of comb spectrum generated on the designed devices, a good numerical model is required to perform the simulation. The generalized Lugiato-Lefever equation (LLE) is found to be in good agreement with simulation and experimental results [34].

1.2.3 Lugiato-Lefever Equation

The LLE is the nonlinear Schrodinger equation with damping and driving terms to simulate the slow-varying electrical field envelope in the ring cavity [34]. This equation can be solved with dispersion and coupling coefficient measured from characterization of MRR. The Eq. 1.5 shows the LLE with Raman effect [27].

$$(t_R \frac{\partial}{\partial t} + \frac{\alpha + \kappa}{2} + i \frac{\beta_2 L}{2} \frac{\partial^2}{\partial \tau^2} + i\delta)E - \sqrt{\kappa} E_i n = i\gamma L (E \int_{-\infty}^{+\infty} R(\tilde{\tau}) E(t, \tau - \tilde{\tau})^2 d\tilde{\tau}) \quad (1.5)$$

In Eq. 1.5, t_R is the round trip time, α is loss coefficient, κ is coupling coefficient, L is cavity length, δ is pump detuning, γ is nonlinear coefficient and $R(\tilde{\tau})$ is the nonlinear response of resonator including the Ramen effect [27]. The pump tuning process in the comb generation process is simulated with fixed pump power and continuously changing detuning. The detuning term δ (the difference between pump frequency and resonance frequency) is set to be linearly increasing in the first 2 μ s and then held constant at its maximum value for the another 2 μ s to simulate the pump laser tuning process.

We can retrieve the comb spectrum, both in frequency domain and time domain from the simulation results to estimate the final state for a given input power and detuning in the different dispersion regimes.

Fig. 1.5 is an example of simulation results when the same parameters are applied except for dispersion β_2 to describe the comb generation results in the different dispersion regimes.

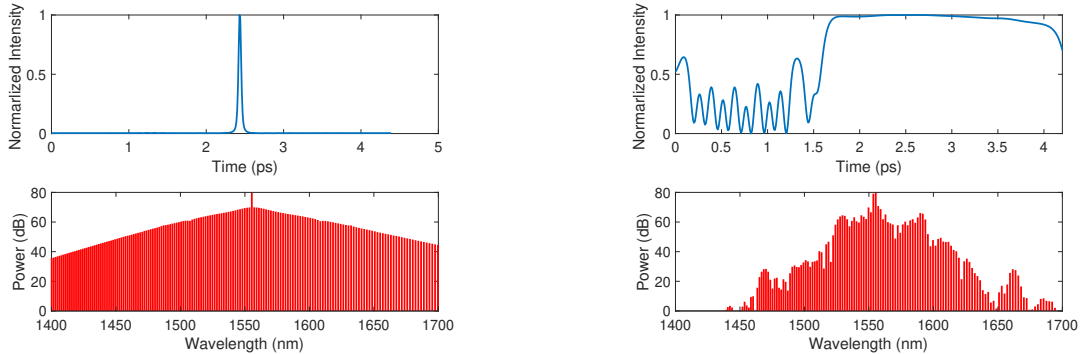


Figure 1.5. Examples of soliton simulation result of 230 GHz ring resonator in the different dispersion regime. Left: Bright soliton in the anomalous dispersion regime. Right: Dark soliton in the normal dispersion regime. Upper figure: Time-domain intra-cavity waveform. Bottom figure: Frequency domain intra-cavity waveform.

1.3 Two Coherent States in Different Dispersion Regimes

1.3.1 Bright Soliton in the Anomalous Dispersion Regime

When $\beta_2 < 0$, we call it anomalous dispersion regime. In the anomalous dispersion regime, the coherent state is a bright soliton [35]–[38]. The soliton state is a mode-locked state with low phase difference between comb lines. Unlike the fiber solitons, Kerr solitons are dissipative solitons that require balance between dispersion versus nonlinearity and input power versus loss.

Single-soliton states, where only one pulse in a roundtrip time (See Fig. 1.6 (a)), exhibit a smooth envelope following the sech^2 function in the frequency domain. In the time domain, the waveform is a short pulse.

The multi-soliton states, which refer to several pulses in one roundtrip time, have much better performance in power conversion efficiency from the pump line to comb lines with the larger power variation between the nearby comb lines compared to single-soliton states (see Fig. 1.6 (b)).

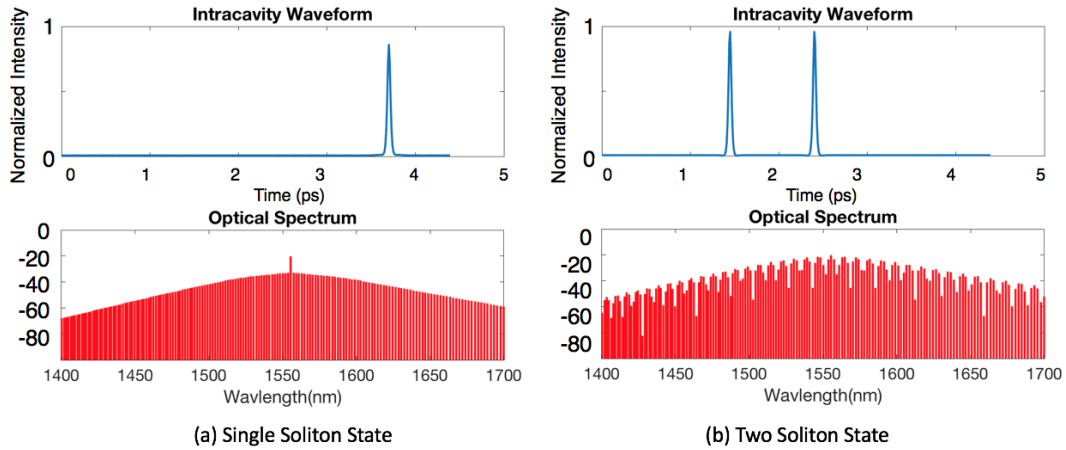


Figure 1.6. Example of Bright Soliton. (a) Time domain and frequency domain spectral of single soliton (b) Time domain and frequency domain spectral of two solitons

1.3.2 Dark Pulse in the Normal Dispersion Regime

As shown in Fig. 1.5, dark pulses exhibit a dip in the background. The envelope of a single FSR dark pulse is not smooth like the single soliton. However, the dark pulse exhibit much higher comb conversion efficiency comparing to the single soliton state, which is desired to provide more power in each comb line while limiting the pump power. We would discuss the details of dark pulse in Chapter 2.

1.4 Device Design for Microring Resonators

SiN microring resonators can be fabricated via the electric beam lithography (e-beam) technique. The e-beam machine writes the user-defined device pattern with the lithography.

To design a ring waveguide, we need to decide the ring radius and waveguide cross section dimensions to meet the requirements required by their applications. For example, to match the grid of communication channels, the FSR of ring resonator utilized in telecommunication is usually chosen as a fixed number such as 50 GHz. We can determine ring FSR by choosing proper waveguide group index and ring radius. We would discuss the details about device

parameter optimization to meet the requirements for various applications in the following sections of the thesis.

After choosing the target devices parameters, we define a chip layout (see an example in Fig. 1.7) with a fine sweep of devices parameters to compensate the possible offset between the simulation and fabrication. Several location markers are also included on the corners of a chip to help the alignment in the fabrication process.

1.5 Thesis Outline

In Chapter 2, we focus on the frequency comb applications requiring high comb line amplitude. We will discuss the dark pulse generation in normal dispersion regimes, which exhibits much higher comb power conversion efficiency than the heavily researched single soliton combs. The low repetition rate and high power conversion efficiency dark pulse is demonstrated to provide a compact source for telecommunication or radio frequency filtering. Then the breathing dark pulse state is discussed to provide a better understanding of dark pulse.

In Chapter 3, we will discuss the modeling and demonstration of thermal tuning in the SiN microring resonators for the tunability of Kerr frequency comb. The tuning of resonance frequency and repetition rate is discussed both in simulation and experimental characterization. The simulation provides an approach to predict on-chip thermal tuning efficiency before the device fabrication. The experimental characterization explores the choices of ring heater material and width towards large resonance frequency shift. Additionally, the test of microheater reliability is performed to explore the limitation of thermal tuning.

In Chapter 4, we will discuss the dispersion engineering in the SiN waveguide design for octave-spanning soliton generation to enable an on-chip fully-stabilized comb source. Waveguide simulation is conducted to optimize waveguide dimension to attain low pump dispersion and dispersive wave generation for octave-spanning frequency comb generation. The corresponding strategy of waveguide design is discussed. Then the approach to reduce carrier offset frequency of microcombs is discussed. Finally, the experimental demonstration of octave-spanning solitons is presented.

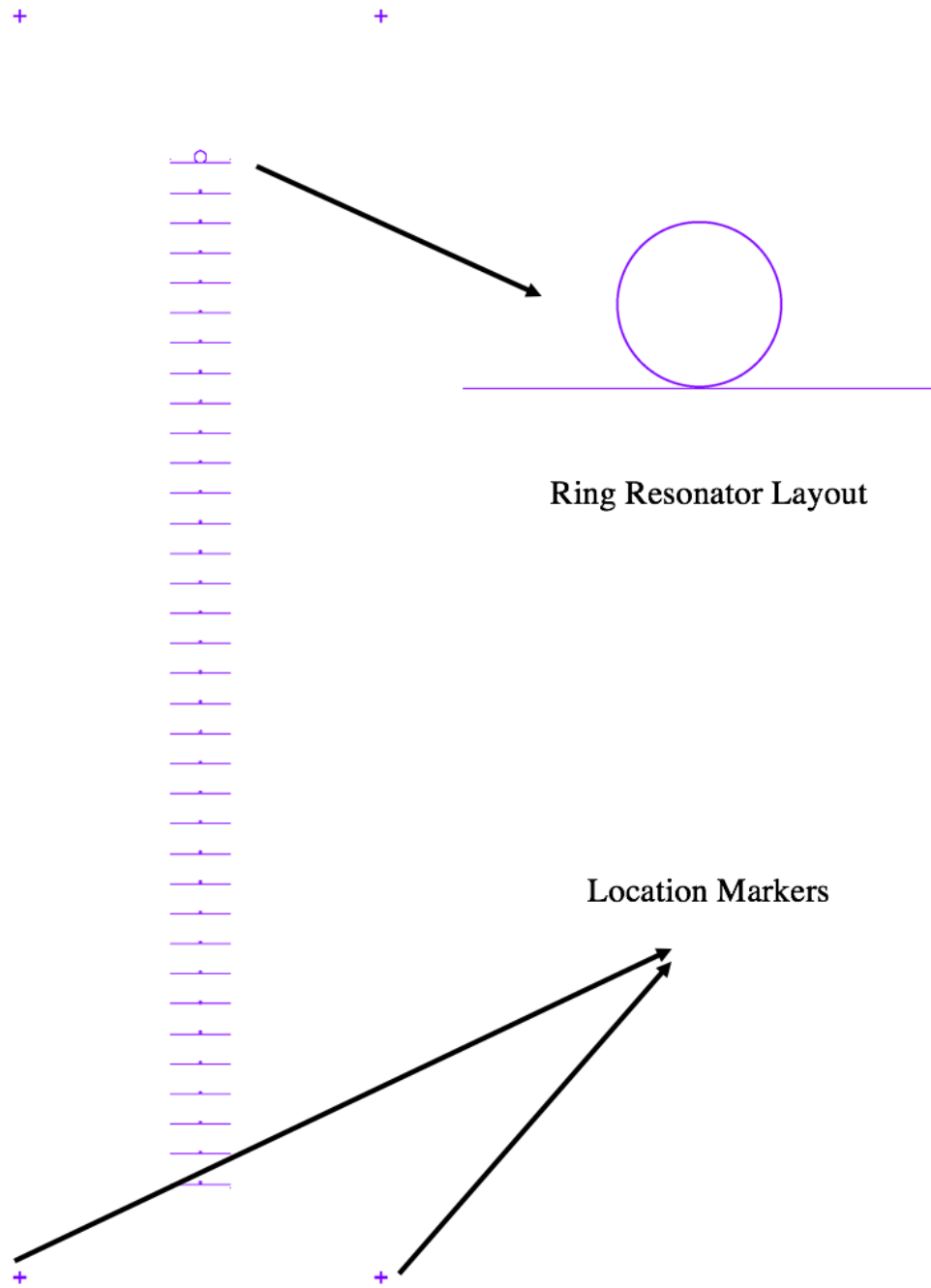


Figure 1.7. Sample Layout for Microring Resonators and Location Markers

In Chapter 5, we will discuss the optical division of a 900 GHz octave-spanning soliton with a 25 GHz microcomb fully based in SiN platform. The repetition rate of the microcomb

is designed to be around 900 GHz to achieve octave-spanning bandwidth. However, the large repetition rate is far beyond the electronic detectable range. To retrieve the repetition rate of the octave-spanning microcomb, an auxiliary soliton with low repetition rate is employed to provide a divided version of the high repetition rate. The experimental demonstration is realized on an all-SiN platform to reduce the difficulty in integration.

In Chapter 6, we will discuss another approach of optical division of a 900 GHz octave-spanning soliton. In this chapter, the auxiliary comb is a Vernier broadband soliton with \sim 880 GHz repetition rate. The comparison of two optical division approaches is discussed in the last section.

Finally, we summarize the works in this thesis.

2. INVESTIGATION OF COHERENT KERR FREQUENCY COMB GENERATION

For the applications of microcombs, the phase coherence is the most important requirement to avoid unwanted signals and phase noise in the system. In this chapter, we will discuss the coherent Kerr frequency combs generation in the normal dispersion regime. The investigation of bright solitons in the anomalous dispersion regime will be discussed in the following chapters.

2.1 Dark Pulse Generation

Within the two coherent states in the different dispersion regimes, dark pulses have two major advantages.

The first advantage is the less complexity in the fabrication process. The dispersion parameters are mainly determined by the dimension of the ring waveguide, ring width (w_r) and thickness (h_r), when the material and the structure of the waveguide are the same. For the common waveguide structure we are working with, the SiN core embedded in the SiO₂ cladding, the normal dispersion devices require much thinner SiN film thickness compared to the anomalous dispersion devices. Extra efforts is needed for the fabrication of anomalous dispersion rings due to the potential cracking arising from stress on the lower layer [39].

The second advantage is the high comb conversion efficiency, which represents the ratio of power converted from pump to comb lines. Dark pulses can achieve above 30% conversion efficiency [40]–[44] while the heavily researched single bright solitons only convert less than 1% of power to the comb lines. This feature will be discussed in detail in the following sections.

2.2 Modeling of Dark Pulse Generation

To predict the dark pulse spectrum of a fabricated devices, the simulation based on the LLE is performed on the normal dispersion microresonators. As mentioned before, dark pulse generation can rely on the mode interaction to excite the first sideband. Therefore,

except for choosing the right sign of the dispersion terms β_2 , the important adaptation for the LLE in the normal dispersion regime is adding the mode interaction phase.

2.2.1 Mode Interaction in the Normal Dispersion Dark Pulse Generation

Mode interaction, or mode coupling, occurs when the resonances from different mode families overlap with each other. Typically, this coupling happens between two modes from the same transverse polarization, such as the fundamental and higher order mode. In some cases, the TE mode can also interact with the TM mode [45].

For resonators, we can write the dispersion relation in the terms of resonances (the higher order dispersion terms are ignored) and mode number (the pump resonance is set to be mode 0).

$$\omega(\mu) = \omega_0 + D_1\mu + \frac{1}{2}D_2\mu^2 \quad (2.1)$$

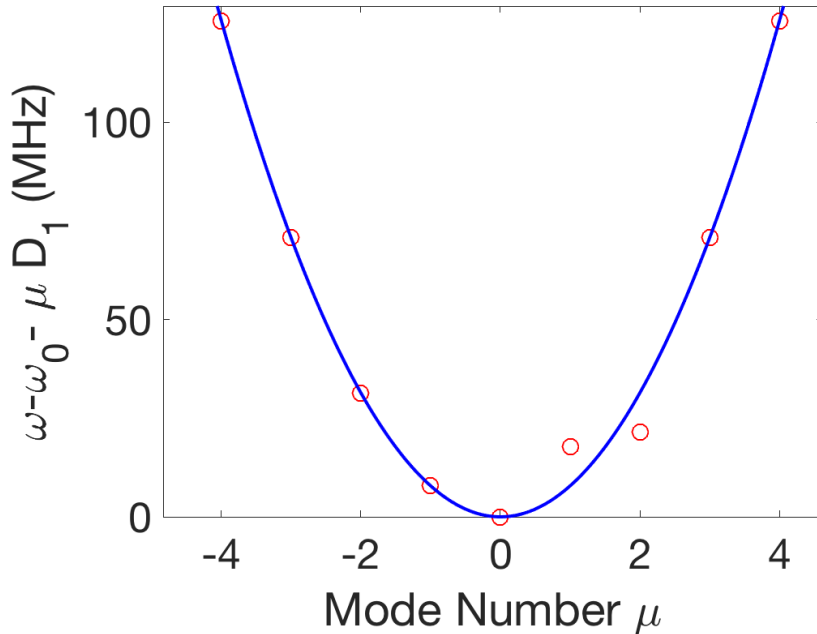


Figure 2.1. Examples of Mode Interaction Induced Resonance Frequency Shift. Red Dots: Resonance frequency offset from equal distance grid. Blue Curve: Parabolic fitting results.

When mode interaction occurs, the resonance frequency is shifted away from the Parabolic relation in Eq. 2.1 (see Fig. 2.1). So a delta function in Eq. 2.2 is used to represent the mode interaction induced phase change [27], [46]. Parameter a_i reveals the mode interaction strength and ω_i represents the mode interaction frequency for i -th mode counting from the pump resonance. Typically, two modes are involved in the mode interaction process. For the two neighbor modes that involved in the mode interaction, the absolute value of the mode interaction strength for the two modes are very close. However, the signs of frequency shift from parabolic fitting for these two modes are different (as shown in Fig. 2.1). In the experiments, the value of coefficient a_i can be calculated based on the retrieved offset between mode interaction resonance frequency and parabolic fitting.

$$\phi(\omega) = \frac{a_i}{\omega - \omega_i} \quad (2.2)$$

After defining the mode interaction induced phase, we can use the modified LLE to simulate the dark pulse generation. To verify whether the modification phase term (Eq. 2.2) can help the prediction of the dark pulse combs via LLE, the LLE with parameter a_i for each mode i retrieved from a dark pulse microresonator is solved based on split step Fourier method.

Table 2.1. Experimental Measured Mode Interaction Parameter Values for Different Modes on a 230 GHz Repetition Rate Normal Dispersion SiN Microring

Mode Number i	-2	-1	0	+1	+2	+3
$a_i(\times 2\pi \text{ GHz})$	1.02	0.82	-0.50	-2.02	2.84	2.63

Fig. 2.2 shows the comparison between experimental and simulated comb spectrum for dark pulse generation in a 230 GHz ring resonator. The blue lines are optical spectrum measured by optical spectrum analyzer and the red curve is simulated intracavity spectrum in frequency domain. Split Fourier method is used to solve the equation with random generated noise. The dispersion coefficient $\beta_2 = 106ps^2/km$ and mode interaction coefficient a_i is calculated by fitting results from linear transmission data (see Table. 2.1). For this

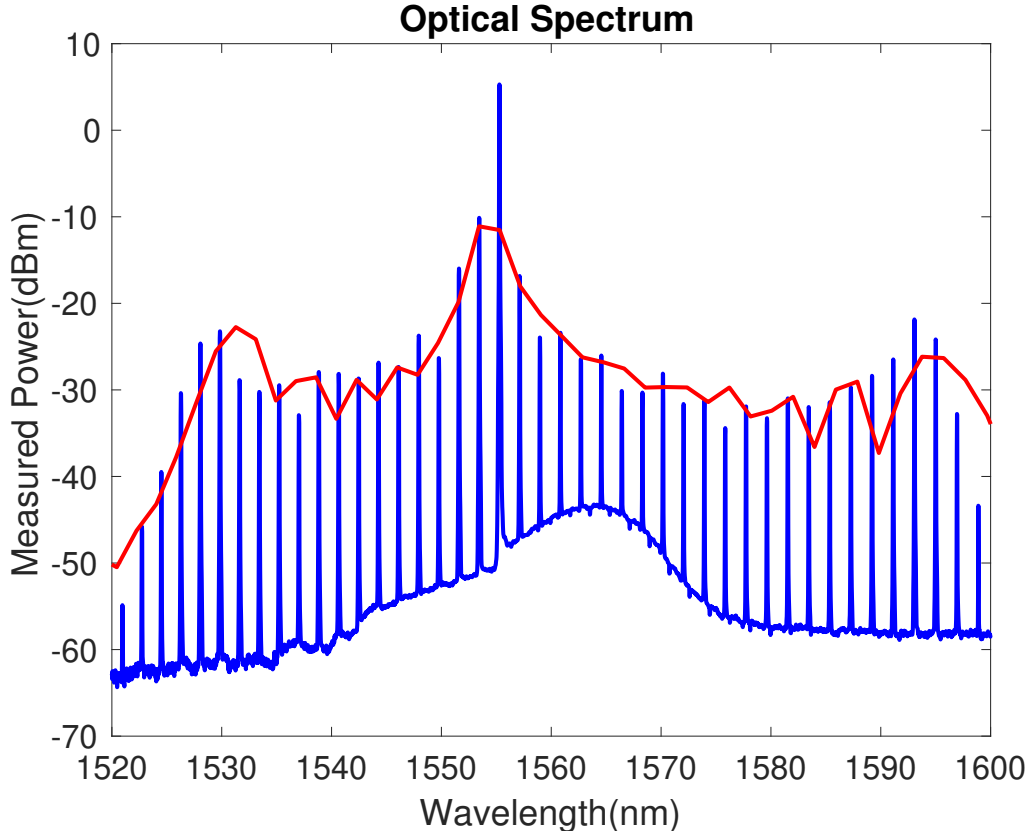


Figure 2.2. Examples of Comparison Between Simulated Optical Spectrum and Experimental Results

resonator, six modes near the pump are involved in the mode interaction process. The pump is single frequency CW laser with 800 mW on-chip power around 1555.3 nm.

The simulation is fit well with the experiment data except the discrepancy near 1555 nm due to pump residue in the bus waveguide. The other power mismatch may due to the dispersion profile. In overall, the simulation results fit well with the experiment data. Therefore, we can use this method to study the effect of mode interaction on the dark pulse generation.

2.3 Comb Conversion Efficiency Characterization

For potential commercial applications, power conversion efficiency is an essential concern especially for coherent communication [4] and RF filtering [7] due to the desire for indepen-

dent utilization of each comb line. In this section, the characterization of a 50 GHz dark pulse comb is performed to reveal the advantage of dark pulse with the respect of comb conversion efficiency¹.

Here we define the comb power conversion efficiency as the ratio between the comb power in the output bus waveguide (excluding the pump line) and the input pump power in the bus waveguide (see Eq. 2.3).

$$\eta_{comb} = P_{comb}^{bus} / P_{pump}^{bus} \quad (2.3)$$

Here, η_{comb} is the comb conversion efficiency, P_{comb}^{bus} is the comb power (excluding pump) in the bus waveguide and P_{pump}^{bus} is the input pump power in the bus waveguide.

2.3.1 SiN Microring Device for Normal Dispersion Dark Pulse Generation

The microring we use here has a waveguide cross section of $560 \text{ nm} \times 2 \text{ } \mu\text{m}$. This dimension is designed to reach the normal dispersion. The free spectral range of the ring is 48.3 GHz and the loaded Q factor is measured to be 1.8×10^6 . The ring consists of a drop port to filter out the pump for further comb flattening (see Fig. 2.3). The ring cavity is a "J" shape to avoid crossing the e-beam writing fields. Crossing the e-beam writing fields can result in extra loss from e-beam movement stitching error in the waveguides.

2.3.2 Comb Generation

Since the dark pulses can be excited by the mode interaction. The first step is to find mode interaction regions via the linear characterization, which is the low input power transmission scan of the ring resonances. Fig. 2.4 shows the plot of FSR versus pump wavelength of the fundamental TE mode (blue) and higher order TE mode (green). The mode interaction frequency is marked with a red circle. An abrupt change in the FSR occurs in the mode interaction regime and results in the local dispersion change, which excites the comb generation. After mapping out the mode interaction region (as shown in Fig. 2.4), we pump

¹The results shown in this section was published in [40]

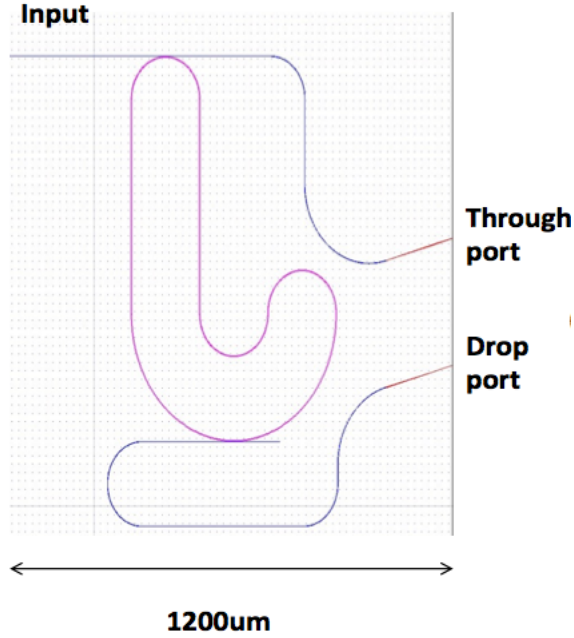


Figure 2.3. Device Layout for Normal Dispersion Dark Pulse Generation [40].

a resonance in the mode interaction region with an on-chip power of 273 mW. By tuning the pump wavelength from blue to red, we are able to generate the comb.

When further tuning the wavelength into the resonance, we can get a noisy single-FSR comb at the pump wavelength of 1556.429 nm. The comb gets broader but becomes a 2-FSR comb when increasing the pump wavelength to 1556.440 nm. By further tuning the pump wavelength to 1556.447 nm, we can reach the final broad low-noise comb, as shown in Fig. 2.5. The comb maintains low-noise operation when tuning into the final comb state (State 4 in Fig. 2.5 (b)). The final comb state exhibits high conversion efficiency from the pump into the converted comb lines.

2.3.3 Comb Power Characterization

P_{comb} is the summation of the power of the converted comb lines (excluding the pump line) and P_{bus} is the input pump power. The fiber-to-chip coupling loss is 3.75 dB per facet. Fig. 2.5(b) shows the comb generation when the pump is at 1556.4 nm with 273 mW

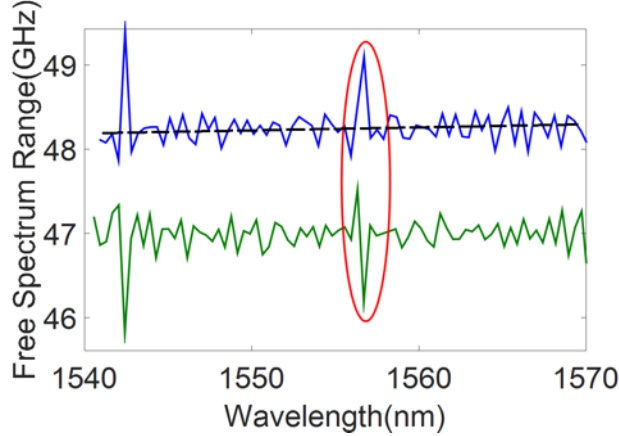


Figure 2.4. Mode Interaction Position. Blue line represents the fundamental TE mode and green line indicates the higher TE mode. The red circle is the mode interaction region we choose to pump [40].

in the bus waveguide. The comb power (excluding the pump power) on the through port is 93.3 mW (34% of the input power). An additional 9.13 mW (3.3% of the input power) emerges from the drop port, which has weaker coupling. The total converted comb power in the through and drop port yields 37% conversion efficiency from the pump.

In many experiments, most of the power remains at the pump frequency. For example, for Kerr combs in the anomalous dispersion microresonators comprising single cavity solitons, the conversion efficiency into the comb may be less than 1% [36]. Recently, examples of high conversion efficiency combs have been reported. In the mid-IR region, 40% comb conversion efficiency has been achieved with a 127 GHz repetition rate, anomalous dispersion silicon microring [38]. This comb operated in the multiple cavity soliton regime, which increases power conversion compared to single cavity soliton combs at the cost of strong line-to-line variations in the comb power. Also, 31.8% conversion efficiency has been reported in the lightwave communication band (C band) with a 231 GHz repetition rate, normal dispersion SiN microring [43]. This comb operated in the mode-locked dark pulse regime, which provides relatively smooth line-to-line power.

Here, the low repetition rates (50 GHz) dark pulse allows four times more channels for C band communication than previous case (231 GHz) while maintains the equally high comb conversion efficiency.

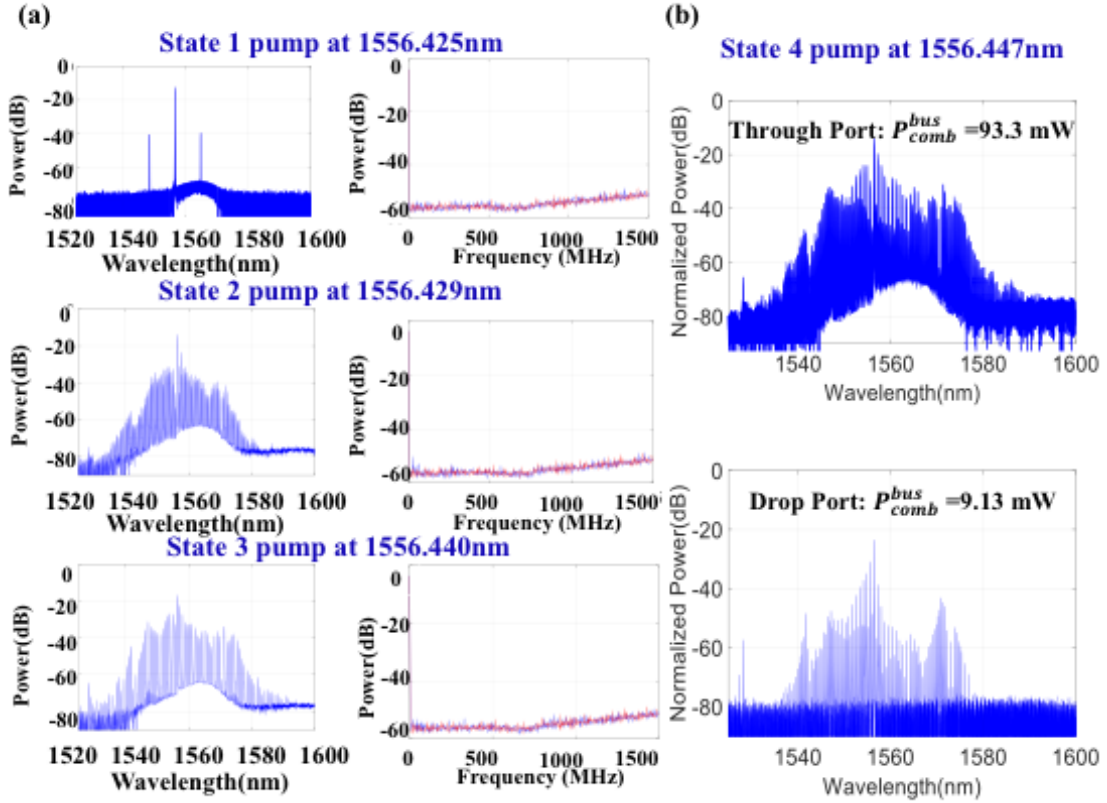


Figure 2.5. Comb spectrum. (a) Comb evolution process while tuning into resonance. The left side shows the optical spectra and the right side shows the intensity noise spectra. Blue lines show the intensity noise of comb and red lines show the background when pump off-resonance. State 1: Initiation of Comb. State 2: Single FSR low noise comb. State 3: 2 FSR low noise comb.. (b) The final comb state, Upper: comb spectrum at the through port, Bottom: comb spectrum at the drop-port.[40]

2.3.4 Dark Breather

Alternatively to the coherent state frequency comb, another interesting state is the breathing state which is a localized wave that exhibits periodic evolution. The breathing states can be reached by increasing the pump power slightly from the coherent states such as bright soliton and dark pulse. In the application of the coherent frequency combs such as coherent telecommunication [4], [6] and atomic clocks [2], breathing instability is expected to be avoided. Therefore, the investigation of the breathing state is important to reveal the dynamics and methods to prevent the breathing state.

In the anomalous dispersion regime, breathing solitons have been reported and characterized [47]–[49]. In the normal dispersion regime, on-chip dark breather (DB) need further study to help reveal the physical dynamic of dark pulse generation [50].

2.3.5 Example of Dark Breather

The 230 GHz ring resonator mentioned in section 2.2.1 is used in the dark breather investigation. The first step is to generate stable dark pulse. When the pump wavelength is set to be one FSR away from mode interaction region between two modes in TE polarization, the type 1 comb is generated at a low noise state (Fig. 2.6(a)). The phase coherence is verified by the line by line shaping and autocorrelation (AC) [29]. In Fig. 2.6 (c) inset, the experimental data after line by line shaping (blue line) fits well with the theoretical data (red dots) which assuming zero phase difference between comb lines.

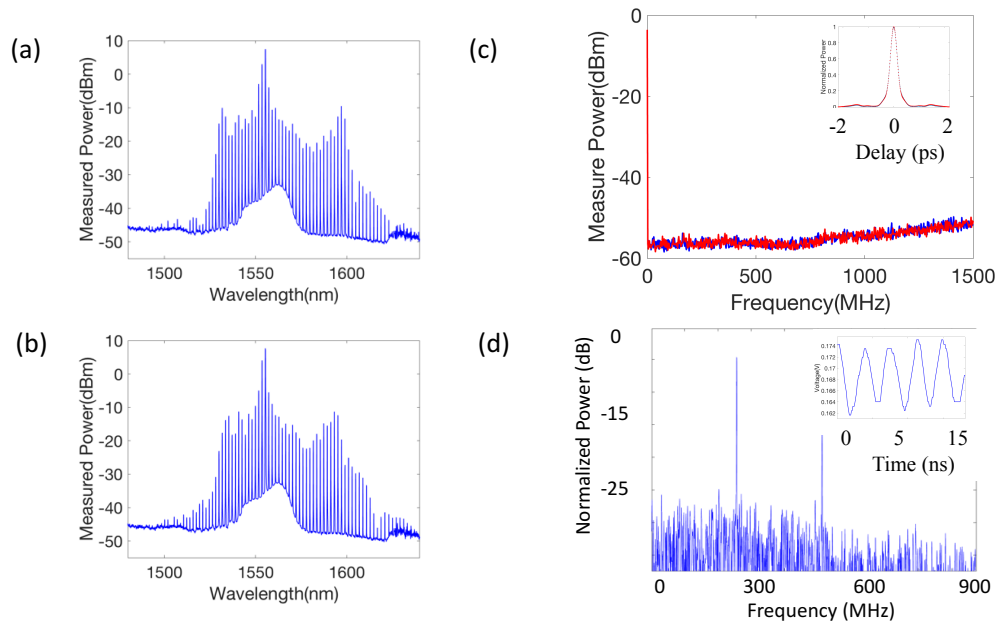


Figure 2.6. Comb spectrum and RF signal measurement. (a) Coherent dark pulse state. (b) Breather state. (c) Comb RF spectrum measured by electrical spectrum analyzer. (d) Single line power breathing

Then the pump power is carefully increased with slight detuning changes to generate a breathing dark pulse (Fig. 2.6 (b)). The sharp beating note can be detected when the comb

signal is sent to an electrical spectrum analyzer via photo diode (Fig. 2.6 (d)). The existence of radio frequency (RF) tones indicate the breathing feature of the comb power and show the breathing frequency (260 MHz). Then the single comb lines are sent to the photo detector to measure the power variation of the single comb lines (Fig. 2.6 (d) inset). The variation period in Fig. 2.6 (d) inset is around 3.8 ns, which is inconsistent with 260 MHz breathing frequency.

The demonstration of the dark breather provide a safe pump power and detuning range of the stable dark pulse.

2.4 Summary

In this Chapter, we demonstrate the coherent dark pulse and investigate the comb conversion efficiency. The breathing dark pulse generation is also discussed to provide a way to switching between breathing and stable states of dark pulse and a safe pump range for dark pulse generation.

Another coherent state, bright solitons in anomalous dispersion regime will be discussed in the following chapters.

3. INVESTIGATION OF THE THERMAL TUNING OF KERR FREQUENCY COMB

In the applications of coherent microcombs, the tunability of frequency comb is critical to the integration. For example, during the process of assembling an on-chip laser and a microring, thermal tuning provides an extra knob of aligning the laser frequency and microring resonance mode. For applications requiring high precision, octave-spanning frequency comb is required to provide a fully-stabilized reference source. Thermal tuning can provide additional tunability of carrier offset frequency to allow f-2f self-referencing.

Therefore, it is crucial to have a good understanding of the mechanism, efficiency as well as the limitation of the thermal tuning. In this chapter, we will discuss the theory and simulation method of modeling the thermal tuning of Kerr frequency comb. Then the characterization of fabricated on-chip heater will be conducted and discussed.

3.1 Simulation for Thermal Tuning of On-chip Frequency Comb

3.1.1 Thermal Tuning Coefficients

When the microresonators are heated up by an external heat source, such as on-chip microheaters, the material refractive indices of the waveguide core and cladding are modified due to the thermo-optic effect. As a result, the waveguide effective index and group index change accordingly and shift the ring resonator resonance frequencies and repetition rates¹.

Here, we focus on the analysis of SiN waveguide buried in SiO₂ cladding. For a microring resonator, the resonance frequency, f_{res} and repetition rate f_{res} can be expressed as Eq. 3.1 and Eq. 1.1 .

$$2\pi f_{res} = \frac{k2\pi c}{n_{eff}L} \quad (3.1)$$

In Eq. 3.1, k represents an integer mode number and n_{eff} represents the effective index of waveguide.

¹The results shown in section 3.1 was published in [51]

When the temperature of a SiN microring resonator increases, n_{eff} and n_g increase due to the thermo-optic effects. The waveguide cross-section dimension and ring cavity length will also change due to the thermal expansion. However, the thermal expansion is relatively small ($3 \sim 4 \times 10^{-6}/^\circ C$ for SiN [52]) compared to the thermo-optic coefficient ($3 \sim 4 \times 10^{-5}/^\circ C$ for SiN [53]). Hence we only take the thermo-optic effects on the refractive indices into account and ignore the small change in the waveguide dimensions.

Then the relation between temperature dependence coefficients, such as df_{res}/dT , df_{rep}/dT , df_{ceo}/dT and dn_{eff}/dT , dn_g/dT could be derived as Eq. 3.2 to Eq. 3.4 [51].

$$\frac{df_{res}}{dT} = -\frac{dn_{eff}}{dT} \cdot \frac{f_{res}}{n_g} \quad (3.2)$$

$$\frac{df_{rep}}{dT} = -\frac{dn_g}{dT} \cdot \frac{f_{rep}}{n_g} \quad (3.3)$$

$$\frac{df_{ceo}}{dT} = \frac{df_{res}}{dT} - m \cdot \frac{df_{rep}}{dT} \quad (3.4)$$

3.1.2 Verification of Thermo-optic Coefficient of Waveguide Material

To calculate dn_{eff}/dT and dn_g/dT , the thermo-optic coefficients of core material (SiN) and cladding material (SiO₂) are required to be measured before the device fabrication, which is typically not accomplished. Therefore, we retrieve the thermo-optic coefficients (dn_{SiN}/dT and dn_{SiO_2}/dT) based on the combination of experimental measurements and simulated parameters and compare the value with reported data to verify the thermo-optic coefficients in our devices.

The resonance frequency tuning coefficient $\frac{df_{res}}{dT}$ can be expressed as Eq. 3.5 with the derivative of n_{core} and $n_{cladding}$. n_{core} and $n_{cladding}$ represents the refractive index of waveguide core and cladding, respectively.

$$\frac{df_{res}}{dT} = -\frac{f_{res}}{n_g} \left(\frac{\partial n_{eff}}{\partial n_{core}} \cdot \frac{dn_{core}}{dT} + \frac{\partial n_{eff}}{\partial n_{cladding}} \cdot \frac{dn_{cladding}}{dT} \right) \quad (3.5)$$

Since we have two unknown variables (dn_{core}/dT and $dn_{cladding}/dT$), $\frac{df_{res}}{dT}$ are measured both in TE polarization and TM polarization with fundamental modes to provide enough equations. The corresponding equations can be written as Eq. 3.6 [51].

$$\frac{df_{TE}}{dT} = -\frac{f_{TE}}{n_{g,TE}} \left(\frac{\partial n_{eff,TE}}{\partial n_{core}} \cdot \frac{dn_{core}}{dT} + \frac{\partial n_{eff,TE}}{\partial n_{cladding}} \cdot \frac{dn_{cladding}}{dT} \right) \quad (3.6)$$

$$\frac{df_{TM}}{dT} = -\frac{f_{TM}}{n_{g,TM}} \left(\frac{\partial n_{eff,TM}}{\partial n_{core}} \cdot \frac{dn_{core}}{dT} + \frac{\partial n_{eff,TM}}{\partial n_{cladding}} \cdot \frac{dn_{cladding}}{dT} \right) \quad (3.7)$$

In Eq. 3.6., $n_{g,TE}$, $n_{g,TM}$, $n_{eff,TE}$, $n_{eff,TM}$, n_{core} , $n_{cladding}$ represent TE mode group index, TM mode group index, TE mode effective index, TM mode effective index, waveguide core index and waveguide cladding index, respectively.

The resonance tuning efficiencies and resonance frequencies ($\frac{df_{res}}{dT}$ and f_{res}) of fundamental TE and TM modes are measured in the experiments and the waveguide effective index sensitivity ($\frac{\partial n_{eff}}{\partial n_{core}}$ and $\frac{\partial n_{eff}}{\partial n_{cladding}}$) are simulated via a open source software package, MIT Photonic Band [54].

In the simulation, the room temperature refractive index of SiN and SiO₂ are taken from the measurement data from lab in Birck nanotechnology center (measuring a wafer with similar SiN deposition recipe and process) and literature [55], respectively. The measured and simulated data are presented in Table. 3.1[51]. The corresponding thermo-optic coefficients for SiN and SiO₂ can be solved as $2.96 \times 10^{-5}/^{\circ}\text{C}$ and $0.61 \times 10^{-5}/^{\circ}\text{C}$, which are comparable to literature previously reported value [53].

3.1.3 Estimation of Thermal Tuning Efficiency of Resonance Frequency based on Simulation

During the design for a photonic integrated circuit, it is required to obtain an estimation of the temperature range of a device to check the necessity of thermal isolation. Therefore, the estimation of thermal tuning efficiencies in the simulation is critical to predict the required temperature change.

Table 3.1. Measured and Simulated Parameters for Thermo-optic Coefficients Calculation [51]).

Parameters	Value
Measured f_{TE}, f_{TM}	~ 193.5 THz
Measured $\frac{df_{TE}}{dT}$	-2.632 GHz/°C
Measured $\frac{df_{TM}}{dT}$	-2.330 GHz/°C
Simulated $n_{g,TE}$	2.059
Simulated $n_{g,TM}$	2.076
Simulated $n_{eff,TE}$	1.774
Simulated $n_{eff,TM}$	1.706
Simulated $\frac{\partial n_{eff,TE}}{\partial n_{core}}$	0.915
Simulated $\frac{\partial n_{eff,TE}}{\partial n_{cladding}}$	0.155
Simulated $\frac{\partial n_{eff,TM}}{\partial n_{core}}$	0.770
Simulated $\frac{\partial n_{eff,TM}}{\partial n_{cladding}}$	0.365

In the simulation, we can estimate the thermal tuning efficiencies via Eq. 3.5 if we can retrieve the simulated ring resonance frequency.

To calculate the resonance frequency of a ring resonator based on waveguide simulation, we rewrite Eq. 3.1 as Eq. 3.8. The effective index can be simulated with finite element eigenmode solver such as Lumerical MODE with different propagation wavelengths. We can plot a product of calculated k versus frequency as Fig. 3.1.

$$\frac{L}{c} \cdot (f_{res} n_{eff}) = k \quad (3.8)$$

For example, we simulate a SiN waveguide with cross section 750 nm \times 2000 nm (height \times width) and 100 μ m ring radius. When we are calculating a resonance frequency around 193.5 THz, the value of k should be 744 since k should be an integer. Then we can fit the curve to retrieve corresponding resonance frequency for k = 744. In this case, the calculated resonance frequency around 193.5 THz is 193.43 THz.

It is worth mentioning that we assume the cladding is uniform in Eq. 3.5, i.e. the top cladding and bottom cladding are the same type of SiO₂. However, in some SiN waveguide fabrication recipes, there are different layers of cladding using different types of SiO₂, which exhibits small discrepancy in refractive index (typically less than 2% around 1550 nm).

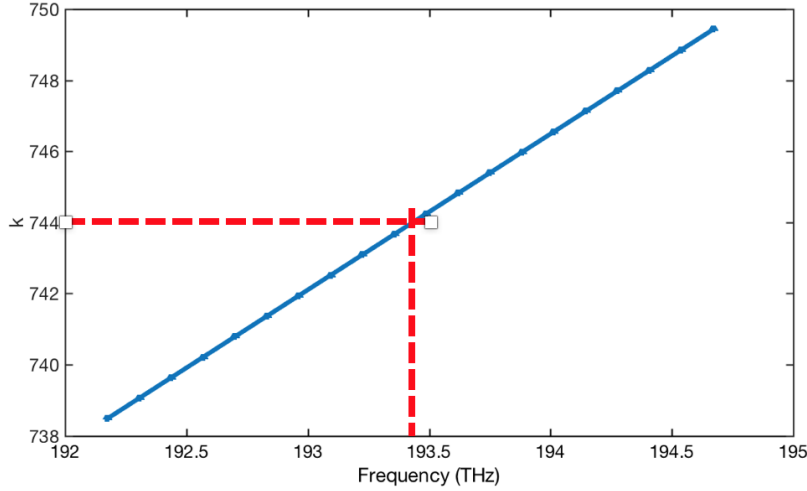


Figure 3.1. Schematic Diagram of Calculating Simulated Resonance Frequency

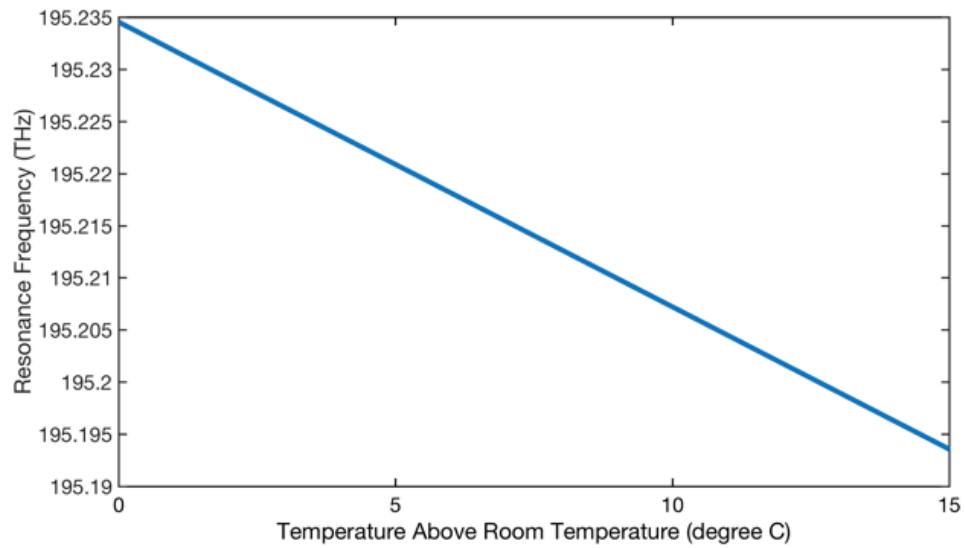
To improve the simulation accuracy, the simulation can be conducted using temperature-dependent refractive index to calculate f_{res} and f_{rep} , correspondingly. Then the thermal tuning efficiency can be calculated by fitting the curve of f_{res} versus temperature (see Fig. 3.2). This simulation is conducted with temperature-dependent refractive index of SiN and SiO₂. The temperature is increased from room temperature to 15 °C above room temperature. The ring radius is 23 μm .

As shown in Fig. 3.2 (a), the resonance frequency shifts to longer wavelength side when the temperature increases. The resonance frequency tuning efficiency is about 2.73 GHz/°C. The repetition rate tuning efficiency is about 15.3 MHz/°C.

3.2 Design and Characterization of Microheater

The temperature of the microring resonators can be increased via an on-chip microheater, which is a thin layer (\sim several hundreds of nanometer) of metal deposited on top of the optical waveguide. The common materials of heater are gold (Au), titanium (Ti), platinum (Pt) or aluminum (Al). To avoid oxidation of SiN, on-chip heater is not suitable for the air-cladding waveguides. To investigate the microheater tuning efficiency and feasibility, we conduct characterization of the microheater deposited on top of the SiN microring resonators.

(a)



(b)

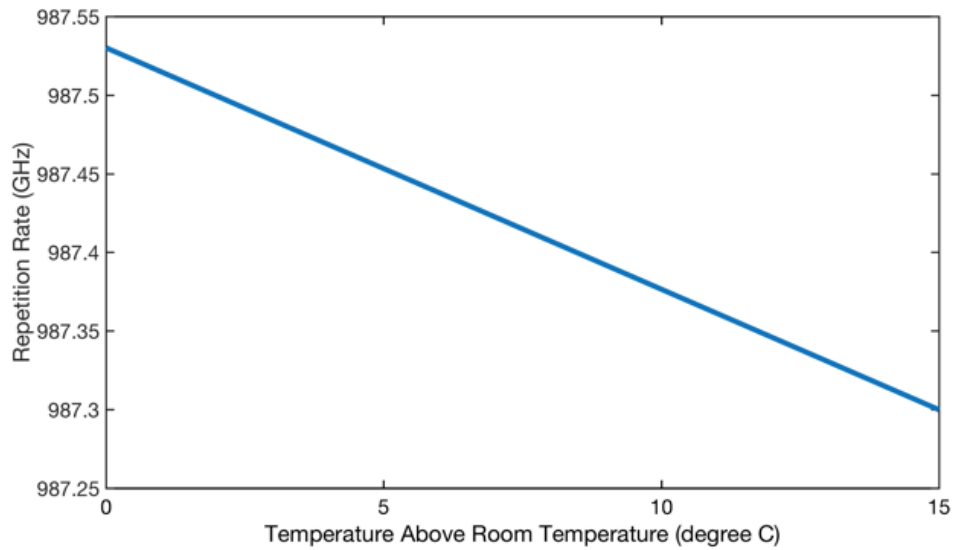


Figure 3.2. Simulation of Resonance Frequency and Repetition Rate Tuning with Temperature Dependent Refractive Indices

To optimize the microheater performance, the effect of microheater material, ring heater width are investigated in this chapter.

3.2.1 Structure of On-chip Microheater

A microheater consists of two contact pads and a ring heater as shown in Fig. 3.3. The contact pads provide the room for probing the microneedles. The ring heater follows the shape of ring resonators to supply efficient heat.

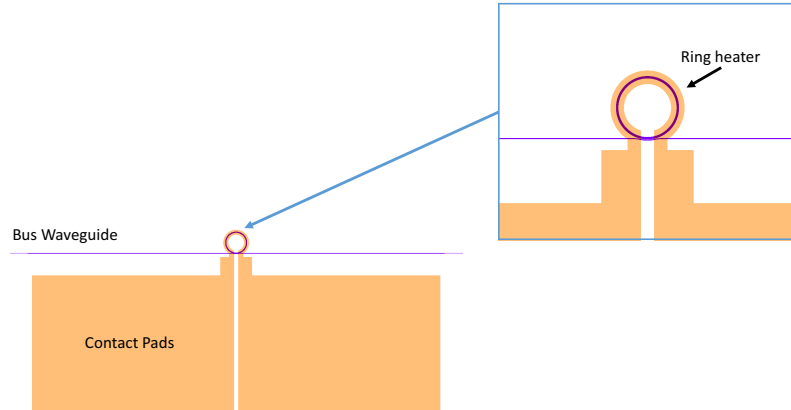


Figure 3.3. Example Layout of Micro Heater. Orange: microheater. Blue: Waveguide

3.2.2 Characterization of Microheater Resistance

The resistance of microheater contains two parts; contact resistance and ring heater resistance. The total resistance of a microheater can be measured by a multi-meter or a current source (voltage source). But the ring heater resistance can not be directly measured.

To separate the ring heater resistance from the total resistance, a test structure is prepared at the spare space on the chip as shown in Fig. 3.4. The test structure is a pair of connected contact pads without ring heater part. Since the test structure and the real contact pads are fabricated using the same metal deposition process on the same chip. The contact resistance of the real microheater can be estimated by measuring the resistance of the test structure. Then the ring heater resistance can be calculated by total resistance minus the contact resistance.

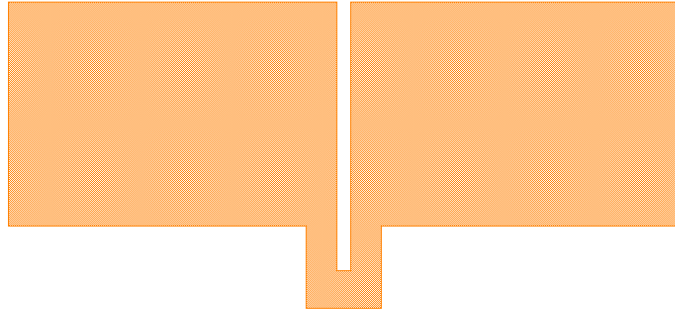


Figure 3.4. Example Layout of Test Structure for Contact Resistance Estimation

3.2.3 Characterization of Resonance Frequency Tuning Efficiency: Titanium Heater

After measuring the electric properties of the microheaters, thermal tuning of ring resonance frequency is conducted to estimate the required electric power for shifting one FSR of the ring resonator. During the integration of the microcavities, the total power requirement is a concern for a portable system. Therefore, we need an estimation of anticipated electric power for thermal tuning.

The resonance frequency tuning efficiency can be measured via linear transmission scan with different electric powers applied on the microheater. During the transmission scans, the input power level is kept below -30 dBm to avoid resonance broadening.

In this section, a titanium (Ti) heater deposited on a 500 GHz SiN ring resonator is characterized as shown in Fig. 3.5. The different colors represent the frequencies of a micro ring resonance mode at corresponding voltage. As the supplied voltage increases, the resonance is tuned from blue to red.

For a heater with consistent resistance, the electric power should be proportional to the square of the applied voltage and the microheater should provide significant more heat when the voltage keeps increasing. However, as shown in Fig. 3.5. The resonance shift after 2 V decreases as the voltage increasing. This is consistent with what we observed in the heater damage process under the optical microscope as shown in Fig. 3.6. Starting around

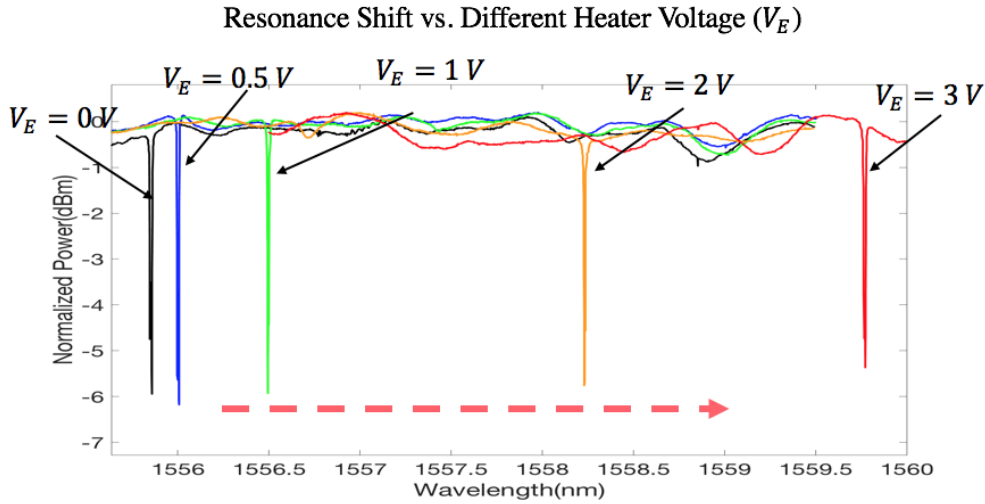


Figure 3.5. Resonance Shift from Blue to Red by Microheater with Increasing Voltage (Devices fabricated by Abdullah Al Noman)

2 V, visible damages start to appear on the ring heater and keep expanding as the voltage increases. At 3 V, the heater is burnt and its resistance becomes infinity.

Several microheaters are tested and the test data are summarized in Table. 3.2. The contact resistances have around 1Ω variation depending the microneedle probing locations. The maximum achieved resonance tuning is defined as the maximum tuning range right before the microheater is burnt. Since the full FSR shifting in resonance frequency is not achieved, the electric power required for 1 FSR tuning is estimated based on the maximum tuning range and corresponding electric power.

Table 3.2. Measured and Estimated Properties of Ti Microheater

Parameters	Value
Measured Contact Resistance	1 to 3 Ω
Estimated Ring Heater Resistance	7 to 12 Ω
Measured Maximum Achieved Resonance Tuning	488 GHz
Estimated Electric Power Requirement to Shift one FSR	500 to 650 mW

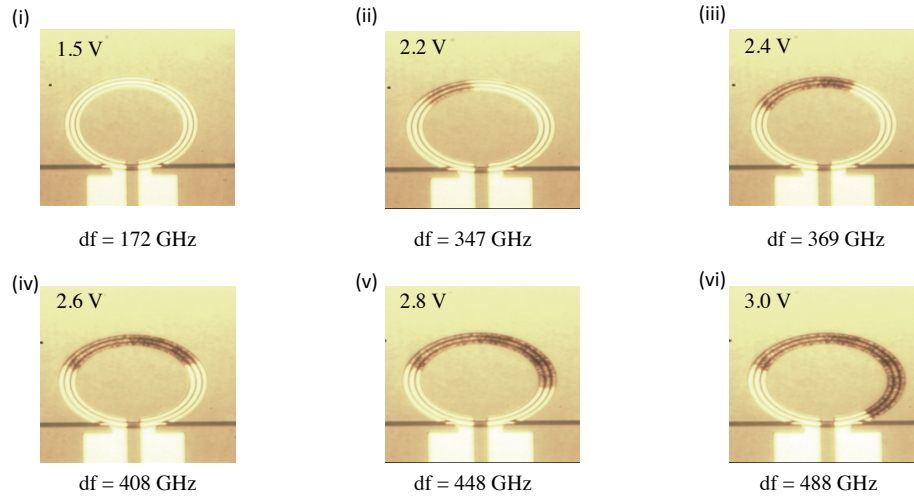


Figure 3.6. Degradation Process of Ti Microheater as the Voltage Increases. df represents the corresponding resonance frequency shift.

3.2.4 Characterization of Resonance Frequency Tuning Efficiency: Platinum Heater

Due to the limited resonance tuning range, the heater material is changed to platinum (Pt) to explore the potential larger tuning range and higher tuning efficiency. The resonance tuning test is performed on both 500 GHz and 1 THz SiN ring resonator as shown in Fig. 3.7 and Fig. 3.8. In those plots, neighbor resonances have been removed in the figures to avoid confusion.

For Pt heater, the maximum tuning range of 1 THz ring and 500 GHz ring is 963 GHz and 1184 GHz, respectively. The measured and estimated parameters are summarized in Table. 3.3 and Table. 3.4. For Pt microheaters, the resistance increases when the metal temperature increases, so the ring resistances are reported with applied voltage.

The Pt microheaters exhibit about twice the maximum tuning range on the SiN microresonators with even lower electric power requirements for the similar SiN waveguide design (500 GHz rings). Therefore, we choose Pt as the heater material to provide better resonance frequency tuning.

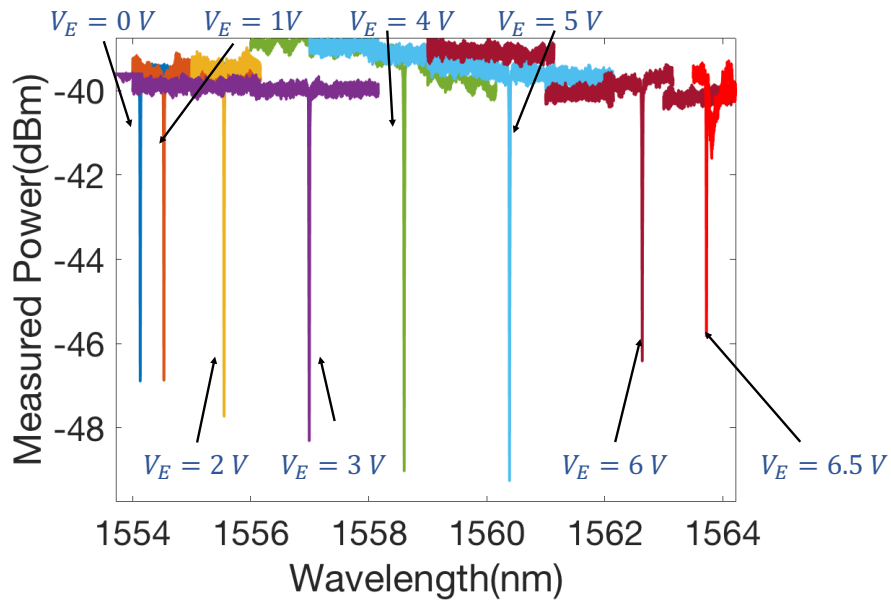


Figure 3.7. Resonance Shift by Microheater with Different Voltage of Pt Microheater on a 500 GHz SiN Ring resonator (Devices fabricated by Abdullah Al Noman)

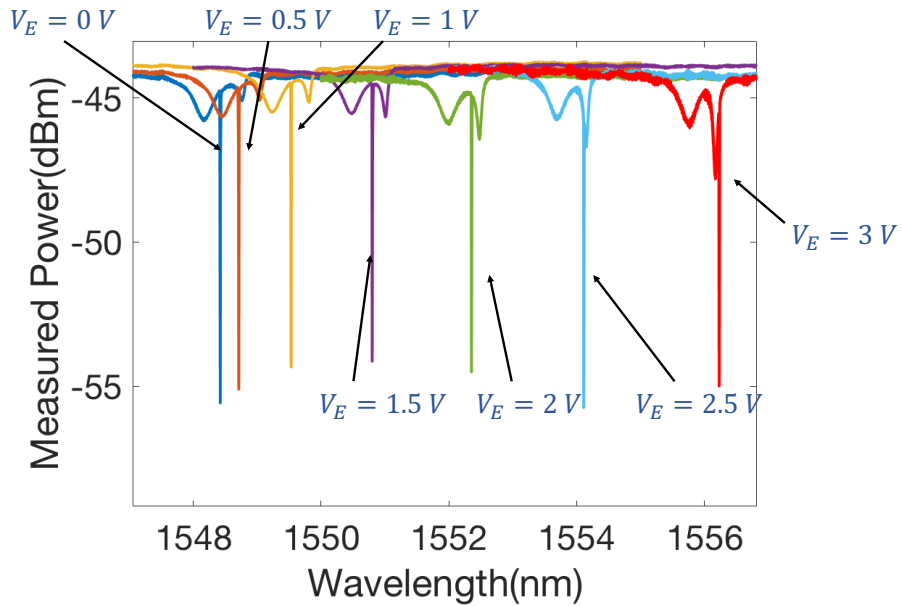


Figure 3.8. Resonance Shift by Microheater with Different Voltage of Pt Microheater on a 1 THz SiN Ring resonator (Devices fabricated by Abdullah Al Noman)

Table 3.3. Measured and Estimated Properties of Pt Microheater on 1 THz SiN Microring Resonators.

Parameters	Value
Measured Contact Resistance	5.4 Ω
Estimated Ring Heater Resistance	10.5 Ω (0 V)/21.6 Ω (3 V)
Measured Maximum Achieved Resonance Tuning	963 GHz
Estimated Electric Power Requirement to Shift one FSR	450 mW

Table 3.4. Measured and Estimated Properties of Pt Microheater on 500 GHz SiN Microring Resonators.

Parameters	Value
Measured Contact Resistance	5.4 Ω
Estimated Ring Heater Resistance	20.1 Ω (0 V)/37.4 Ω (4 V)
Measured Maximum Achieved Resonance Tuning	1184 GHz
Estimated Electric Power Requirement to Shift one FSR	380 mW

3.2.5 Characterization of Resonance Frequency Tuning Efficiency: Heater Width

Except for the microheater material, the ring heater width is also an important parameter affecting the resonance frequency tuning efficiency. To investigate the affect of ring heater width, a set of microheaters are designed and fabricated with different ring heater widths. Other parameters such as SiN waveguide dimension, heater thickness are kept same. The layouts of the test heaters are shown in Fig. 3.9.

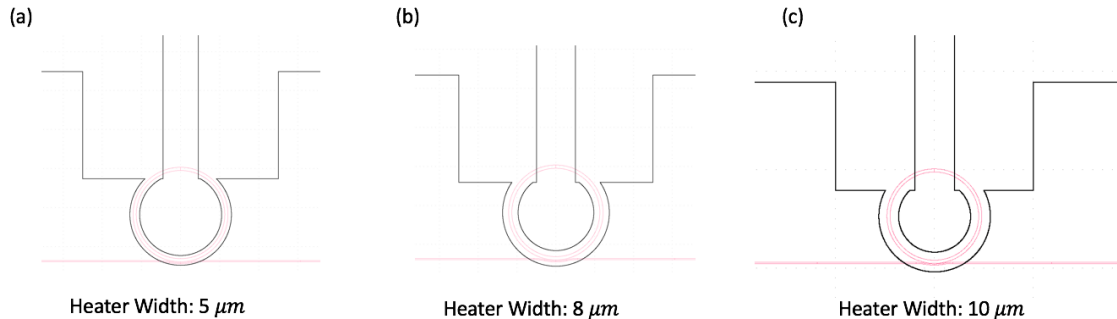


Figure 3.9. Microheater Layout with Different Ring Heater Widths

The resonance tuning experiments are conducted on 3 different ring heater widths and the test results are summarized in Table. 3.5. The maximum achieved resonance tuning ranges are similar for the microheaters with different ring heater widths. But the narrow ring heater exhibits 30% improvement in the required electric power. For wider ring heater, most of generated heat is wasted instead of heating up the waveguide core when the width is too large compared the ring waveguide width.

Ideally, we can use 5 μm ring heater width to increase the thermal tuning efficiency. However, during the microheater fabrication, the SiN waveguide and metal heater layer are fabricated with different process. The misalignment between the positions of SiN microring resonators and microheaters can be a few micron. To reduce the risk of heater misalignment, the wider heaters are needed (ring heater width = 10 μm).

Another reason to choose the wider ring heater width is to increase the heater reliability, which will be discussed in the following section.

Table 3.5. Measured and Estimated Properties of the Pt Microheaters on 1 THz SiN Microring Resonators with Different Ring Heater Widths

Heater Widths	5 μm	8 μm	10 μm
Estimated Ring Heater Resistance	18 Ω	12 Ω	10 Ω
Measured Maximum Achieved Resonance Tuning	910 GHz	900 GHz	960 GHz
Estimated Electric Power Requirement to Shift one FSR	320 mW	380 mW	460 mW

3.3 Characterization of On-chip Microheater Reliability

To ensure the repeatability of our experiments, the heater reliability is as important as the heater efficiency. During the characterization of resonance frequency tuning efficiency, two different types of heater failure are observed. We test the heater reliability based on these two types of heater failure and proposed approaches to avoid heater damage in frequency comb demonstrations.

3.3.1 Failure of On-chip Microheater: Type I

During the operation of on-chip heater, two types of microheater failure are observed. The first type of heater failure occurs immediately after applying a relative high voltage (or current) to the microheater. The major cause is the excessive current density in the thin metal layer.

To investigate the limitation of current density, the current density for a given electric power (P_E) is derived below. The current density δ is inverse proportional to the ring heater width (W_h) as shown in Eq. 3.9. Here I , S_h and H_h represents current, ring heater cross section area, ring heater height, respectively.

$$\delta = \frac{I}{S} = \frac{I}{H_h \cdot W_h} \quad (3.9)$$

When a current I is applied to heater, the corresponding electric power can be calculated in Eq. 3.10, where ρ , L_h is the resistance of the metal heater, heater length, respectively.

$$P_E = I^2 \cdot R = (\delta \cdot S_h)^2 \cdot \rho \frac{L_h}{S_h} = \delta^2 \cdot \rho \cdot L_h \cdot S_h = \delta^2 \cdot \rho \cdot L_h \cdot H_h \cdot W_h \quad (3.10)$$

For a given electric power, the wider waveguide provide lower current density in the ring heater part. If we assume the SiN waveguide absorb same ratio of the generated heat during the heating process, the wider ring heater is harder to break for a given tuning range compared to a narrower ring heater. Therefore, wider ring heater is desired to protect the microheater for a large tuning range.

3.3.2 Failure of On-chip Microheater: Type II

The second type of microheater failure occurs after a longtime heating. The heater gradually degrades during the heating process with same amount of applied voltage(or current). Fig. 3.10 is an experimental observation of the degradation process of a 600 nm thick Pt heater applied with ~ 600 mW electric power. The heating time is listed below corresponding images.

Under the optical microscope, the damaged parts turns from bright yellow to black. During the heating process, the ratio of damaged parts keep increasing until 200 minutes later. After that, the measured resistance of micro-heater becomes infinity. Meanwhile, the resonance frequency shift is monitored via automatic linear transmission scans (every 10 minutes). As shown in Fig. 3.11, start from 40 minutes, the thermal tuning range keeps dropping while the same voltage is applied.

This heater failure is presumed to be caused by electron migration.

Heater Degradation Process

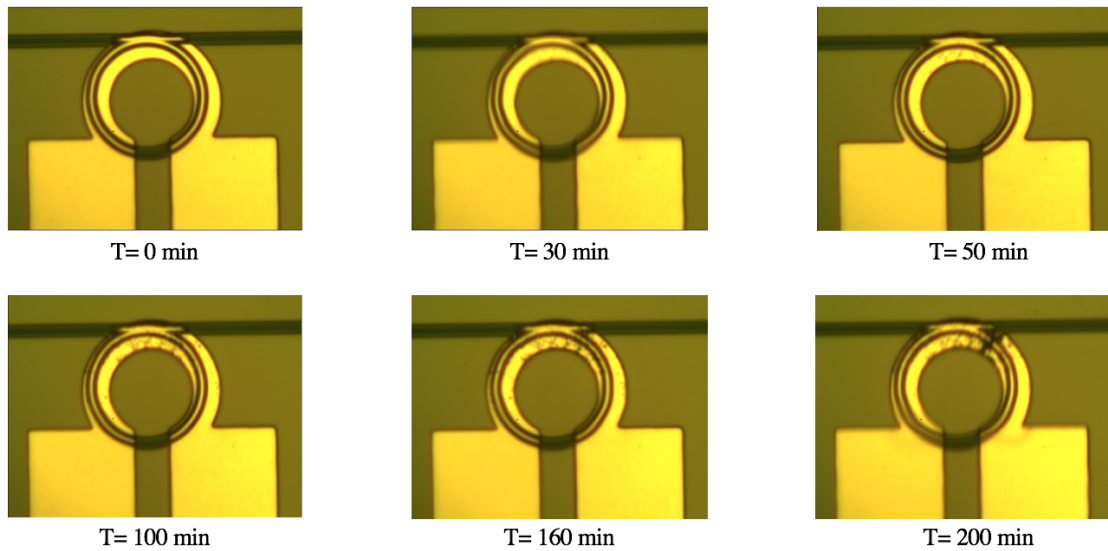


Figure 3.10. Degradation of Microheater While Heating

3.3.3 Approaches to Increase Heater Reliability

For long-term usage of thermal tuning, 200 minutes is not an acceptable duration. To avoid heater degradation, two approaches are proposed.

Firstly, we prepare several test heater structure during the device design. The test structures are used to search the broken boundaries of the microheater to serve as a calibration tool to obtain the long-term heating damage boundary. Then we use the microheater under the damage threshold.

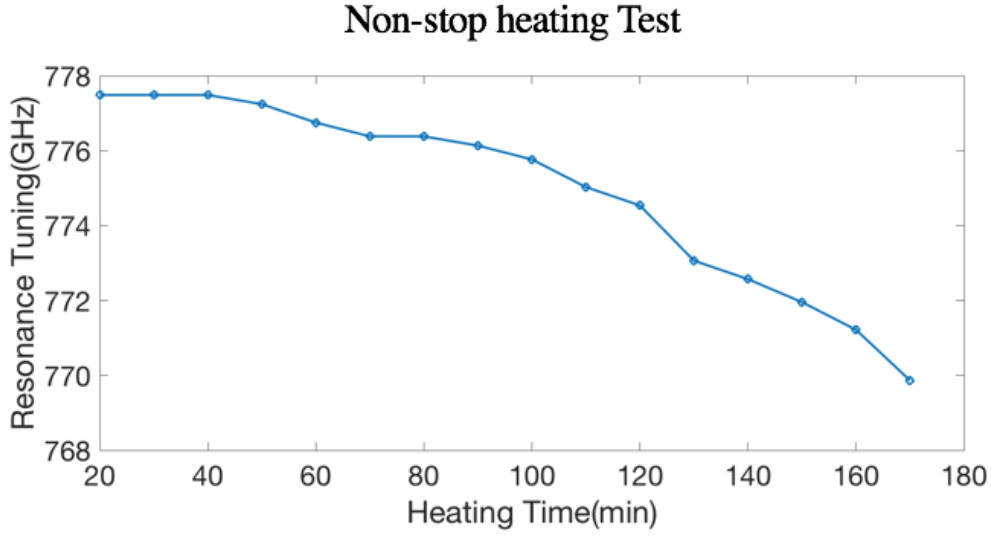


Figure 3.11. Corresponding Thermal Tuning Range During the Degradation of Microheater

Secondly, in the design perspective, simulation and design can be applied to help reduce the require tuning range of microheater. For example, if we need the microheater to align the resonance frequencies of two microring resonators, we optimize the offset between two reonances modes from the two rings and minimize the required thermal tuning range.

Additionally, the overlap parts between SiN waveguide and microheater are observed to be broken more frequently. We optimize the microheater structure to reduce the risk of extra factor of heater failure.

3.3.4 Improvement of Heater Uniformity

The heater in Fig. 3.3 is the optical image of fabricated on-chip heater (corresponding to the layout in Fig. 3.3). In this pattern, the heater covers a segment of the bus waveguide.

A transition part is crossing the bus waveguide to connect ring heater and contact pads. The top surface of top cladding layer contains nonuniform section due to the underneath core waveguide as shown in Fig. 3.12. The "bump-like" structure causes the nonuniform

thickness in the deposited metal and results in the extra bend. Therefore, the overlap region can cause additional risk of burning the heater.

To eliminate the addition risk of heater damage, the overlap between SiN waveguide and microheater need to be minimized. A revised version of microheater layout is shown in Fig. 3.13. The microheater is rotated with 180 degree and a segment of ring heater has been removed.

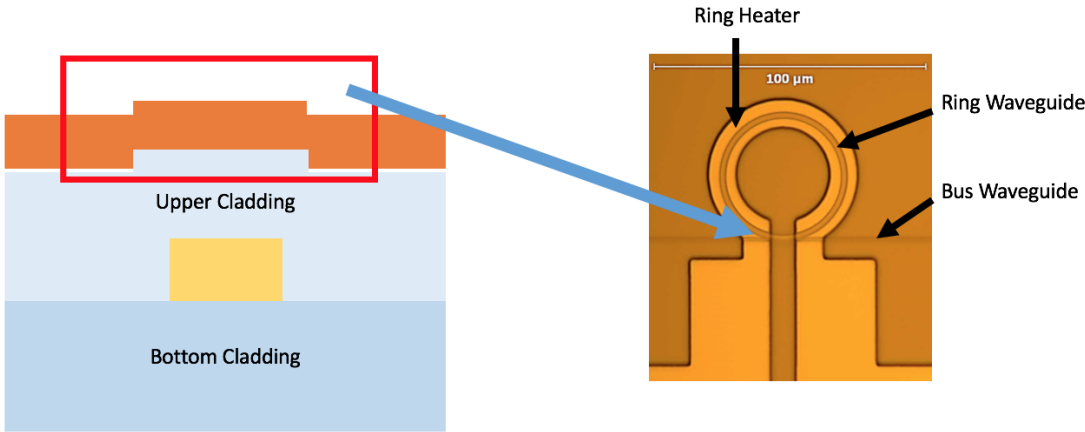


Figure 3.12. Scheme of Heater Metal Deposition

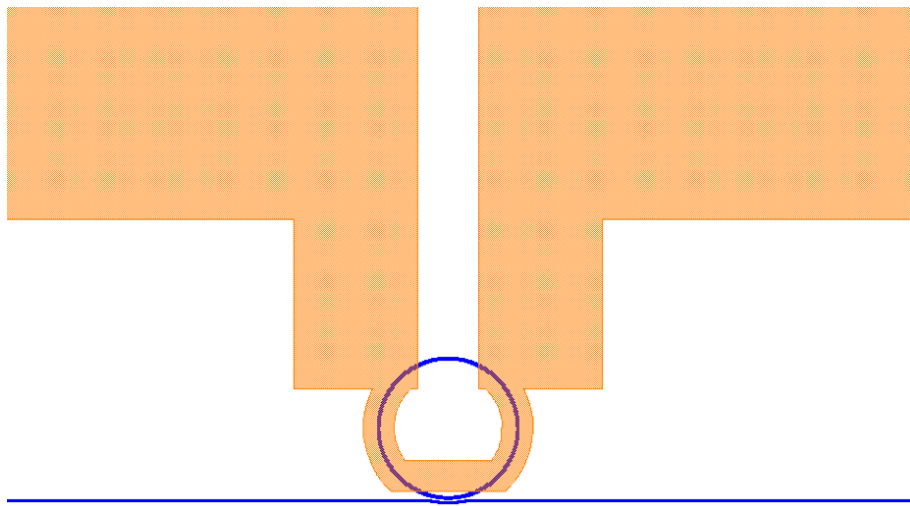


Figure 3.13. Revised Microheater Design to Minimize Overlap Between SiN Waveguide and Heater

4. DISPERSION ENGINEERING FOR OCTAVE-SPANNING SOLITON GENERATION

In previous Chapter, we investigated the coherent frequency comb states of dark pulse in the normal dispersion regime. In this Chapter, we will discuss the coherent comb state in the anomalous dispersion regime, bright solitons. In particular, this chapter focuses on the approach to extend the comb bandwidth to an octave to enable fully stabilization of the Kerr microcombs.

In addition, a broadband comb source would be beneficial for various applications such as dual-comb spectroscopy [56] and metrology [1].

4.1 Stabilization of Kerr Frequency Comb

Kerr microcomb is a promising candidate to serve as a reference source due to its low phase noise feature and compact size. However, when a microcomb is free-running, the dithering of frequency comb lines restrains the comb from serving as a precise reference in the applications like atomic clocks.

The frequencies of Kerr comb lines (f_m or f_n) can be written as Eq. 4.1 or Eq. 4.2; where m and n are integers represent mode numbers.

$$f_m = f_{pump} \pm m \cdot f_{rep} \quad (4.1)$$

$$f_n = f_{ceo} + n \cdot f_{rep} \quad (4.2)$$

These two equations indicate two approaches of comb stabilization; stabilize the pump and repetition rate or stabilize the offset frequency and repetition rate. In particular, f_{ceo} is able to be locked without addition bulk optical sources via the f-2f self-referencing, which paves a way for fully integrated stable frequency comb.

4.1.1 f-2f Self-referencing

The f-2f self-referencing requires the bandwidth of a frequency comb to be ultra broad to span an octave. The octave-spanning comb contains two comb lines (f_1 and f_2), where $2f_1 \sim f_2$. A beat note can be generated between $2f_1$ and f_2 via the second harmonic generation (SHG) process. If we write f_1 and f_2 in the format of Eq. 4.2, the beat note frequency can be derived as Eq. 4.3 to Eq. 4.5. M_1 and M_2 represents the mode numbers for f_1 and f_2 .

$$f_1 = M_1 \times f_{rep} + f_{ceo} \quad (4.3)$$

$$f_2 = M_2 \times f_{rep} + f_{ceo} \quad (4.4)$$

When $2M_1 = M_2$, the beat note is equal to f_{ceo} . If f_{ceo} is electronically detectable, we can lock the beat note (f_{f-2f}) to lock the f_{ceo} .

$$f_{f-2f} = 2 \cdot f_1 - f_2 = (2M_1 - M_2) \times f_r + f_{ceo} \quad (4.5)$$

4.1.2 Towards the on-chip f-2f Self-referencing

Based on the calculation results in previous section, we can summarize the requirements of achieving f-2f self-referencing.

The first requirement is the comb bandwidth. The frequency comb need to span at least one octave, which provides the comb lines with two times difference in the frequency.

Second, the amplitude of the comb lines at f_1 and f_2 need to be large enough to guarantee enough signal to noise ratio (SNR) of the f-2f beat note to feed in the locking feedback loop.

Third, the frequency of beat signal need to be small enough for electronic detection.

In the anomalous dispersion regime, 1 THz spacing octave-spanning comb have been demonstrated with pump near 1550 nm [57]–[59], 1.3 μm [59] and 1 μm [60] based on SiN

microresonators. The octave-spanning bright soliton in Ref.[58] has been employed in the optical-frequency synthesizer construction [61].

4.2 Design for Octave-spanning Bandwidth

4.2.1 Kerr Comb Bandwidth

The bandwidth of Kerr frequency comb is inverse proportional to the square root of group velocity dispersion of the ring waveguide as described in Eq. 4.6 [62]. Here, Δf_{BW-3dB} , γ , P_{in} , F represent 3 dB bandwidth, nonlinear coefficient, input power and cavity finesse, respectively.

A small group velocity dispersion (GVD) is needed at the pump frequency to achieve ultra-broad bandwidth. The waveguide dispersion is determined by material dispersion and waveguide dimension. Therefore, during the device design, we can optimize the GVD by selecting proper waveguide parameters for microrings.

$$\Delta f_{BW-3dB} = \frac{0.315}{1.763} \sqrt{\frac{2\gamma P_{in} F}{\pi|\beta_2|}} \quad (4.6)$$

4.2.2 Ring Waveguide Design Parameters

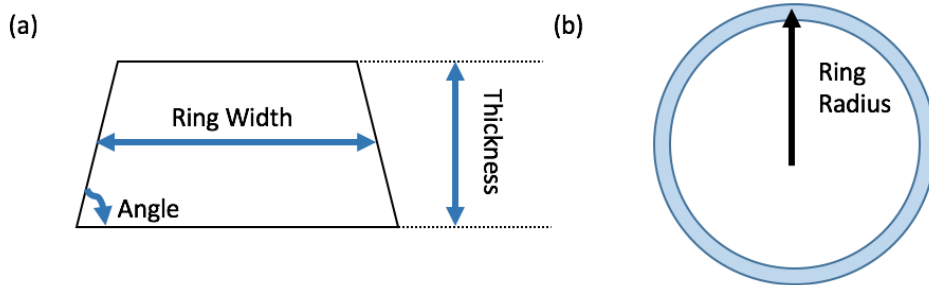


Figure 4.1. Examples of Important Parameters of Ring Waveguide in Device Design. (a) Example of waveguide core. (b) Definition of ring radius.

Fig. 4.1 shows an example of the waveguide parameters we can control in the device design; ring waveguide width (w_{ring}), waveguide height (h_{ring}), ring radius (r_{ring}) and sidewall angle (a_{ring}). In this thesis, the ring width is defined as the median of the trapezoid. The ring radius (r_{ring}) is the distance from ring center to middle of the ring waveguide.

4.2.3 Ring Waveguide Simulation for GVD Optimization

To optimize the GVD for pump wavelength, numerical simulation is performed by a commercial Finite-Difference Eigenmode (FDE) solver (Lumerical MODE).

A trapezoid SiN core embedded in SiO₂ cladding is defined in the simulation with four variables; w_{ring} , h_{ring} , r_{ring} and a_{ring} . Propagate constant (β) and waveguide effective index can be solved in the simulation. Then the group velocity dispersion (D_2) can be retrieved for a given waveguide dimension via sweeping the wavelength of propagating light.

To investigation the relationship between dispersion and waveguide dimension, we plot a map of D_2 for different waveguide dimensions (See Fig. 4.2). In this map, the D_2 is calculated for fundamental TE mode (TE₀). Here we use 200 μm ring radius and the pump wavelength is 1550 nm. For 200 μm ring radius, the bending effect can be ignored. The color bar represents the value of D_2 (ps/km/nm).

The blue side represents normal dispersion regime ($D_2 < 0$) and the red side represents anomalous dispersion regime ($D_2 > 0$). For octave-spanning soliton generation, we need to choose the regime with positive low dispersion such as 720 nm thick and 2500 nm wide. However, the wide waveguide supports higher mode propagation and can introduce mode-interaction, which is unfavorable for a dispersion sensitive soliton generation process due to the potential change to the local dispersion of the fundamental mode.

For the value of D_2 , we want it to be as small as possible for large comb bandwidth. However, if we select a waveguide dimension makes D_2 to be zero. Due to the uncertainty in the wafer thickness in the fabrication process, the dispersion of ring waveguide has the risk to fall into the normal dispersion regime. Therefore, the target value of D_2 is typically between 10 to 30 ps/nm/km.

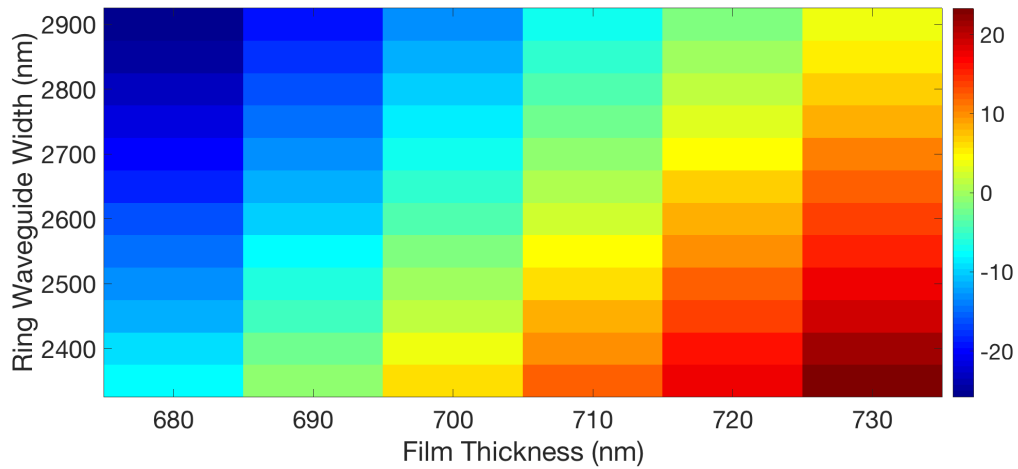


Figure 4.2. Map for GVD Value vs. SiN Waveguide dimension for Waveguide with large bending radius. The intensity color plot represents GVD, D (ps/nm/km).

4.2.4 Ring Waveguide Cross Section Dimensions

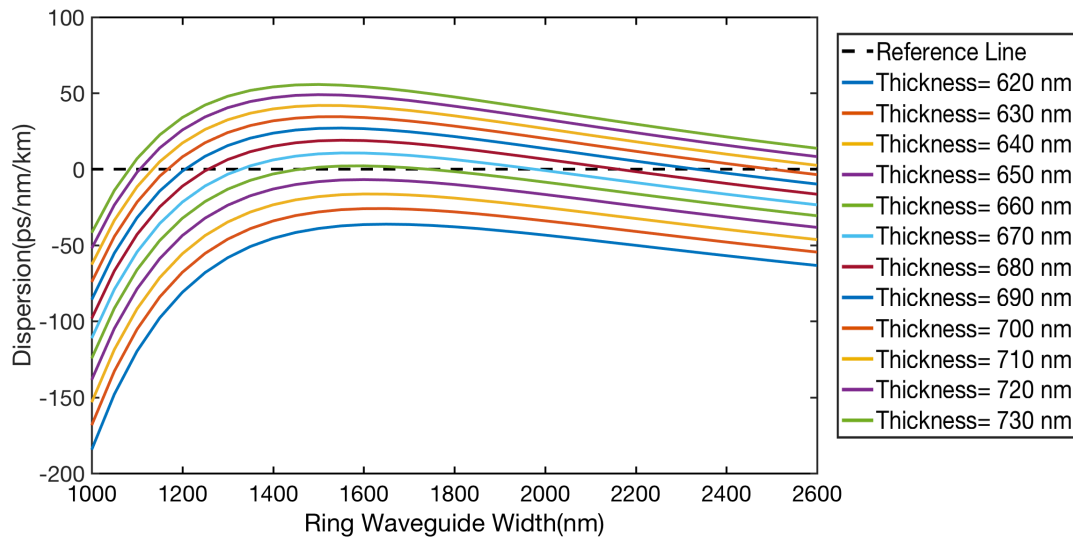


Figure 4.3. D_2 for Different Film Thickness and Ring Waveguide Widths

As Fig. 4.3 suggests, if we want to fit in the targeted D_2 value, we would need to choose either very wide waveguide ($> 2 \mu\text{m}$) or very narrow waveguide ($< 1.3 \mu\text{m}$) for thick wave-

uide (thickness > 700 nm). For thinner waveguide, the optimized ring widths are between $1.4 \mu\text{m}$ and $1.8 \mu\text{m}$.

The narrow waveguides cause additional loss due to the worse light confinement, which increase the comb generation threshold. As mentioned previously, the wider waveguide can bring in mode-interaction between TE₀ and TE₁. The mode-interaction can modify the local dispersion, which can ruin the dispersion engineering.

Therefore, a single mode or close to single mode ring waveguide is preferred to achieve octave-spanning soliton. It is desired to choose a waveguide width containing low group velocity dispersion and being close to single-mode.

4.2.5 Ring Radius

In the ring waveguide design, typically we try to avoid using small ring radius since it would have extra loss induced by waveguide bending.

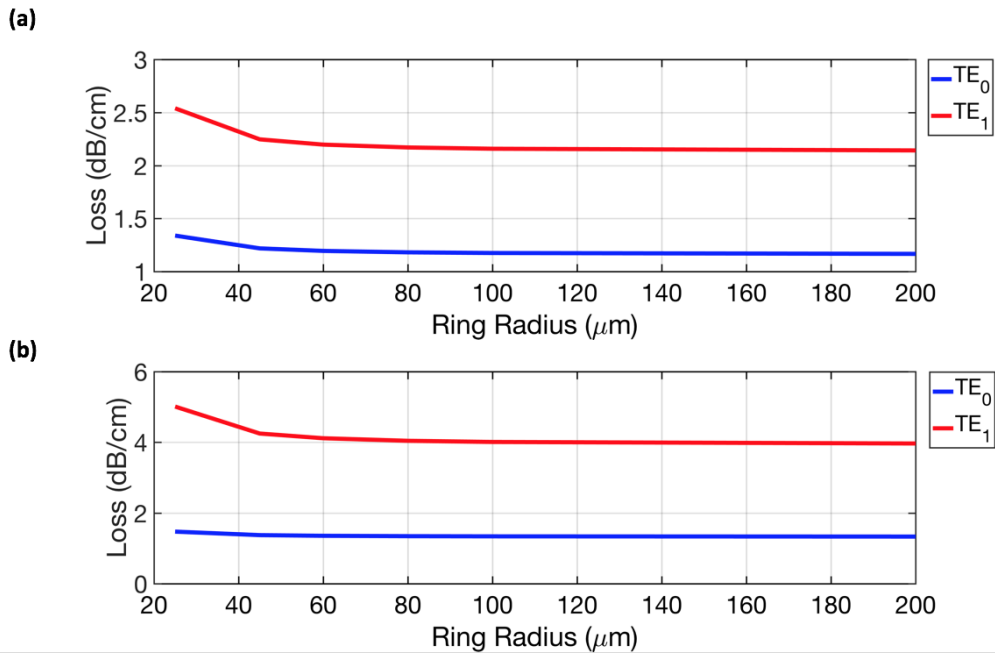


Figure 4.4. Waveguide Loss Comparison Between TE₀ mode and TE₁ mode. (a) Ring Waveguide Dimension (740 nm (thick) \times 2000 nm (wide)) (b) Ring Waveguide Dimension (740 nm (thick) \times 1600 nm (wide))

On the other hand, bending effects induced propagation loss is significant higher for higher order mode compared to fundamental mode for small radius ring. Hence, the small radius rings are easier to become single-mode waveguide compared to large radius rings.

When there is no bending or the bending radius is large (See Fig. 4.4), the loss difference between TE_0 mode and TE_1 mode is not radius-dependent when the ring radius is larger than $60 \mu\text{m}$. However, when the ring radius is below $60 \mu\text{m}$, the TE_1 mode has extra loss compared to TE_0 mode. When the bend waving radius is $25 \mu\text{m}$, TE_1 has significant higher loss compared to TE_0 mode. For the waveguide width smaller ring width, the extra loss of TE_1 is even higher as shown in Fig. 4.4 (a) and Fig. 4.4(b).

If we plot a similar dispersion map as Fig. 4.5 with $45 \mu\text{m}$ ring radius and Fig. 4.6 with $25 \mu\text{m}$ ring radius, the low pump dispersion can be achieved with around $1.7 \mu\text{m}$ for $45 \mu\text{m}$ ring radius and $1.6 \mu\text{m}$ for $25 \mu\text{m}$ ring radius.

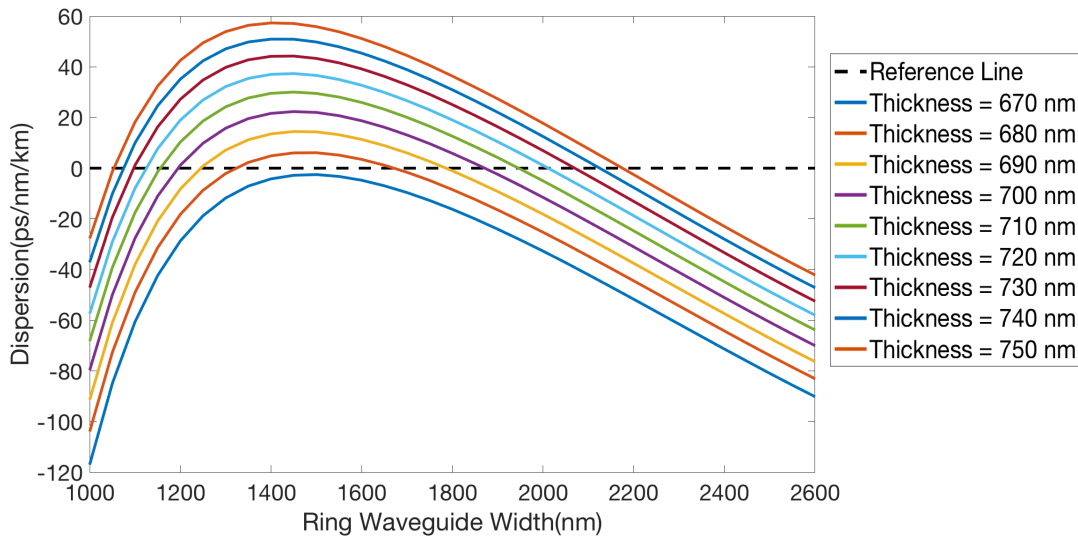


Figure 4.5. Map for GVD Value vs. SiN Waveguide dimension for Waveguide with $45 \mu\text{m}$ ring radius. The intensity color plot represents GVD, D (ps/nm/km).

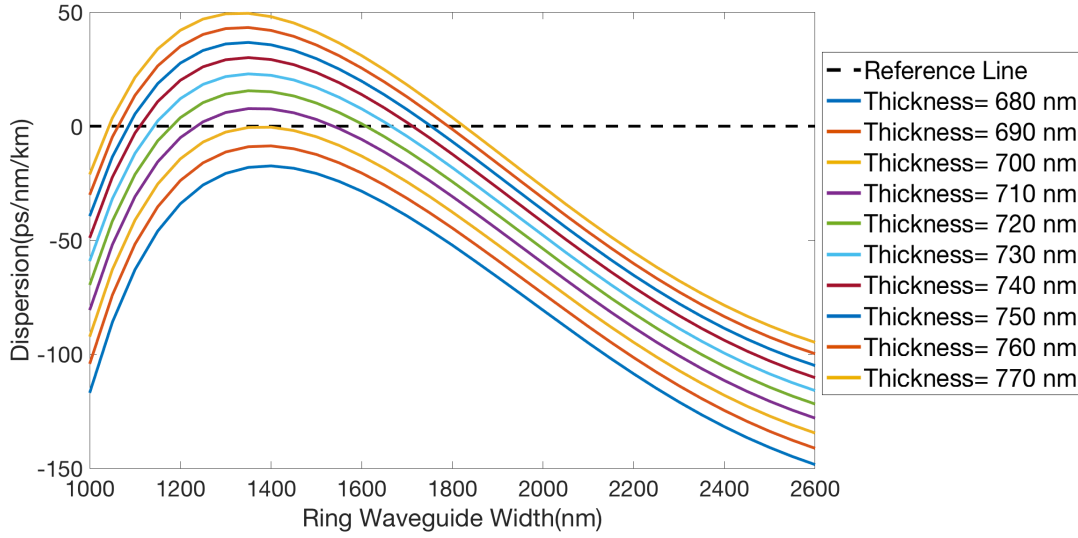


Figure 4.6. Map for GVD Value vs. SiN Waveguide dimension for Waveguide with $25 \mu\text{m}$ ring radius. The intensity color plot represents GVD, D ($\text{ps}/\text{nm}/\text{km}$).

4.2.6 Summary

To achieve low pump dispersion, the choice of waveguide dimensions are narrowed to a small range for both straight and bending waveguides. The choices are list as below.

- For large bending radius waveguide, the SiN film thickness need to be between 680 nm to 700 nm and the ring width is between $1.4 \mu\text{m}$ and $1.8 \mu\text{m}$.
- For small ring radius waveguide, the thickness is between 720 nm to 750 nm and the ring width is around $1.6 \mu\text{m}$

4.3 Dispersive Wave Generation to Enhance Comb Line Amplitude

The enhancement of the comb line amplitudes around f_1 and f_2 for f-2f locking replies on the dispersive wave generation. Fig. 4.7(a) is the spectrum of a soliton without dispersive wave, which has a sech-squared spectral envelope shape. To boost comb lines at f_1 and f_2 , dispersive wave (DW) is introduced near the edge of spectrum in Fig. 4.7(b).

4.3.1 Dispersive Wave for f-2f self-referencing

To attain optimized enhancement in self-referencing signal, the DW generation frequencies should match with f_1 and f_2 via dispersion engineering. Therefore, the prediction of the dispersive wave frequencies is critical to the octave-spanning frequency comb generation.

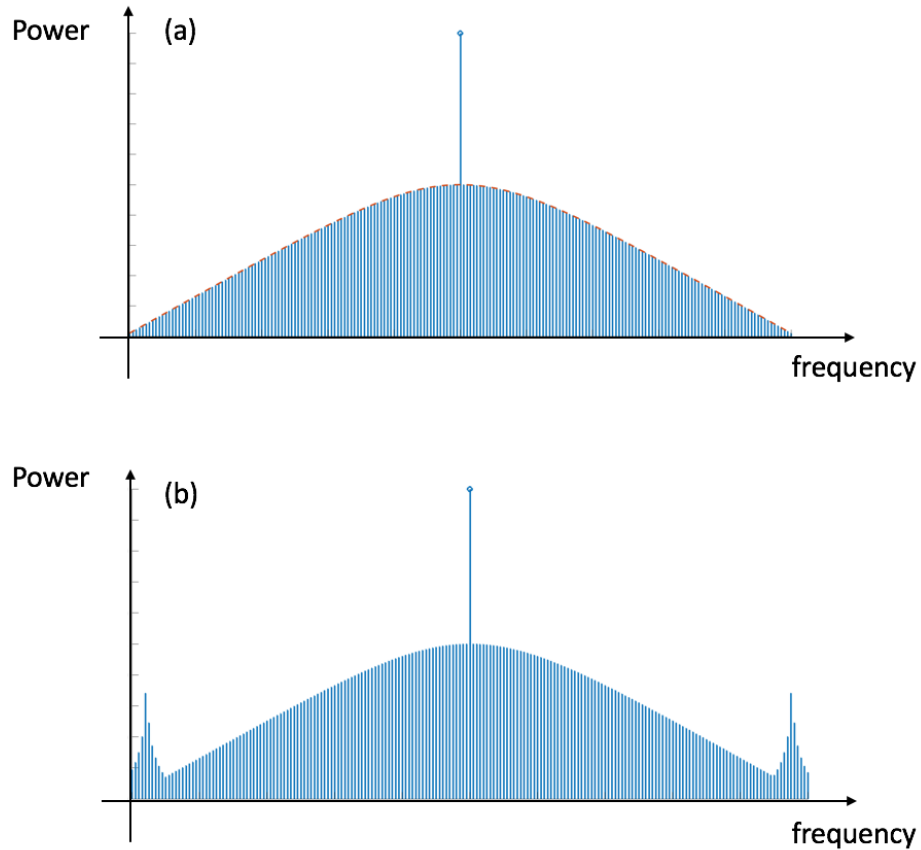


Figure 4.7. Optical Spectra of Bright Soliton with or without Dispersive Wave. (a) Bright soliton without dispersive wave (b) Bright soliton with dispersive wave.

4.3.2 Dispersive Wave Generation in Ring Resonator

The dispersive waves are generated at the frequencies forcing the phase mismatch to be zero. The phase mismatch could be written as Eq. 4.7. Here, ϕ_{PM} , γ , P_0 are the phase mismatching value, nonlinear coefficient, pulse peak power, respectively.

$$\phi_{PM} = \beta(\omega) - \beta(\omega_0) - \beta_1 \cdot (\omega - \omega_0) - \gamma P_0 \quad (4.7)$$

In the previous sections, only second order dispersion term (β_2) is considered since the higher order dispersion is negligible. However, when we push β_2 to low value to achieve broad bandwidth, higher order dispersion terms can not be ignored, especially in the modes far away from pump. The nonlinear phase, γP_0 , is much smaller compared to other terms, so the equation can be modified into Eq. 4.8, which only includes dispersion terms.

$$\phi_{PM} = \beta(\omega) - \beta(\omega_0) - \beta_1 \cdot (\omega - \omega_0) = \sum_{k=2}^{\infty} \frac{\beta_k}{k!} (\omega - \omega_0)^k \quad (4.8)$$

Or in micresonators, Eq. 4.8 can be written as below since only resonances are allowed to propagate in the ring waveguide.

$$D_{int}(\mu) = \omega_\mu - \omega_p - D_1\mu \quad (4.9)$$

In Eq. 4.9, D_{int} is the offset between resonance frequency (ω_μ) of μ th mode from pump resonance ω_p and equidistant grid. The grid track ($D_1/2\pi$) is defined as the FSR of the pump resonance [59].

When the dispersion terms cancel out each other at a mode μ_{DW} , the phase mismatching is zero and the dispersive waves can be generated.

4.3.3 Effect of Refractive Index

Before we discuss the choice of waveguide dimension, we investigate the effect of non-accurate refractive index of SiN and SiO₂ to see the requirement of precision of refractive index.

Fig. 4.8 shows the phase-matching condition based on two waveguide simulations. In those two simulations, the waveguide dimension parameters, ring waveguide radii and SiN refractive indices are same and the only difference is the refractive index of SiO₂ cladding. It suggests using different SiO₂ refractive index dataset can result in a shift of 50 nm in the lower wavelength dispersive wavelength.

A similar comparison is made with different SiN refractive index (see Fig. 4.9). The dispersive wave has around 120 nm offset in the simulation.

These large offsets suggest we need an accurate refractive index of our material. Therefore, in the waveguide optimization process, we use the commercial measured refractive index of our SiN, top cladding SiO₂ and bottom cladding SiO₂.

4.3.4 Waveguide Design for Dispersive Wave Generation

After figuring out the material refractive indices, we optimize the SiN waveguide cross section to generate dispersive wave at target wavelengths (1000 nm and 2000 nm)

We choose the waveguide dimension which pushes the pump dispersion close to zero based on the dispersion map like Fig. 4.3 and Fig. 4.9 and make a dispersive wave map.

For example, if we choose the bending waveguides around 740 nm thick and 1600 nm wide and sweep the ring width in the simulation, the dispersive wave can be achieved around 1000 nm and 2000 nm as shown in Fig. 4.10. This figure shows the optimized waveguide dimension in the simulation.

During the device fabrication, the thickness of SiN film is hard to control precisely and the thickness across the whole wafer is non-uniform. So we also do a phase-matching condition calculation for the thickness around 740 nm to check the dispersive wave frequencies for the thickness slightly away from the 740 nm. Fig. 4.11 shows the calculation results of 745 nm thick SiN film. The simulation result suggests we can compensate the offset in thickness by modifying the optimized ring waveguide width to shift the dispersive wave to the right position.

If we choose the large radius waveguides with 680 nm and 690 nm film thickness, in the low pump dispersion window, no longer wavelength dispersive waves are generated and the shorter wavelength dispersive waves are far below 1000 nm.

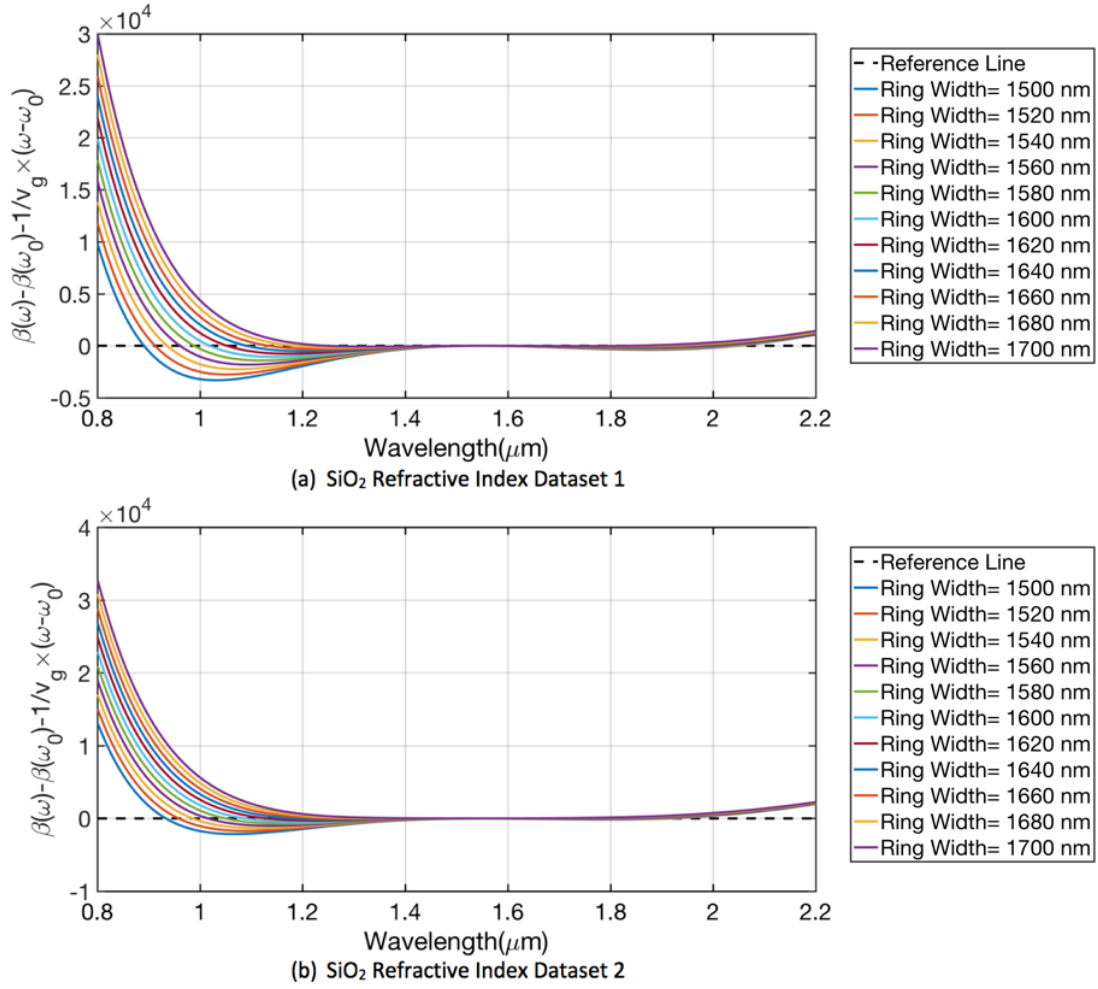


Figure 4.8. Phase Matching Condition for Simulations with Different SiO₂ Refractive Index

Therefore, we choose the small radius ring resonator for the octave-spanning comb generation. The ring radius is around 25 μm and the waveguide cross section is around 740 nm \times 1600 nm.

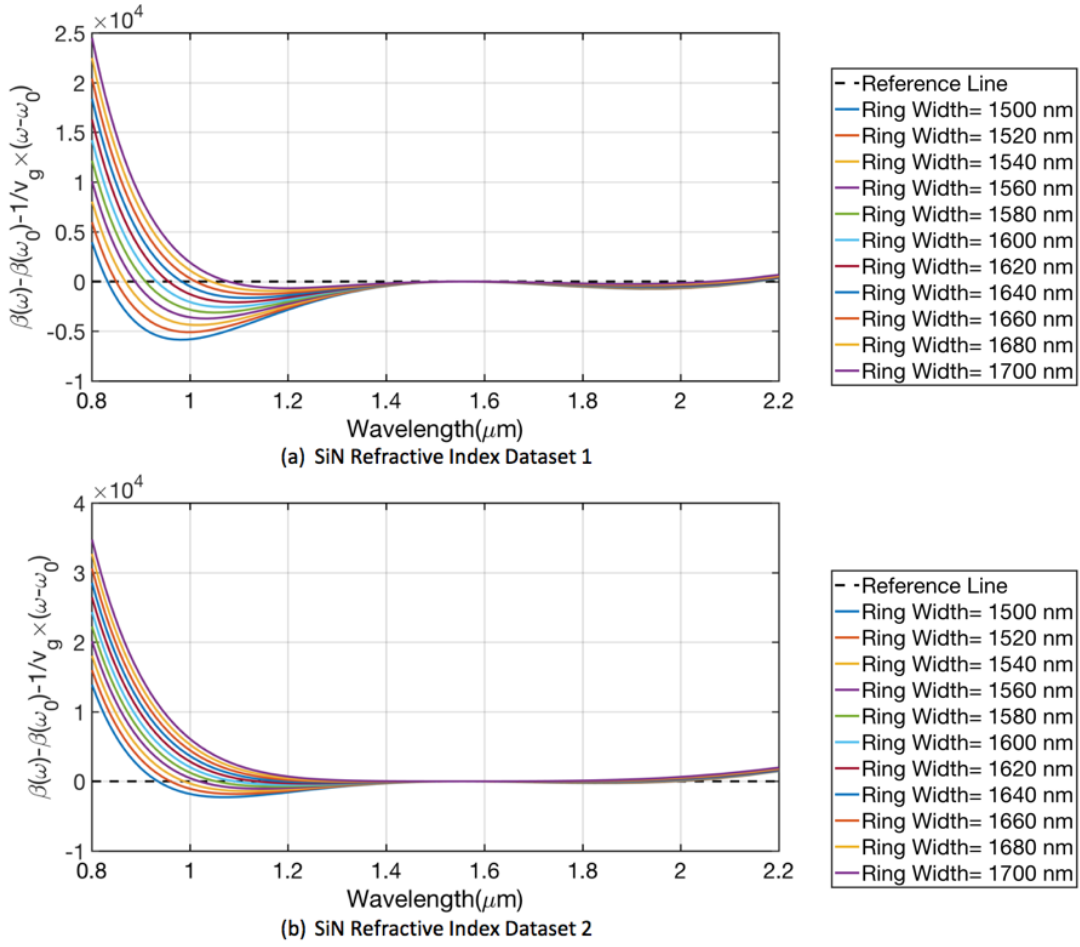


Figure 4.9. Phase Matching Condition for Simulations with Different SiN Refractive Index

4.4 Design for Low Carrier Offset Frequency

4.4.1 Waveguide Design Targeting Low Carrier Offset Frequency

Since the f-2f beat note is determined by f_{ceo} , low f_{ceo} is required to reduce the difficulty of locking. However, for the large FSR rings, it is very difficult since the f_{ceo} can be any value between 0 and $f_r/2$. In our case for a FSR of 900 GHz, f_{ceo} can fall anywhere between 0 and 450 GHz.

Therefore, in the waveguide design, we minimize the value of f_{ceo} based on the simulation to optimize the design parameters.

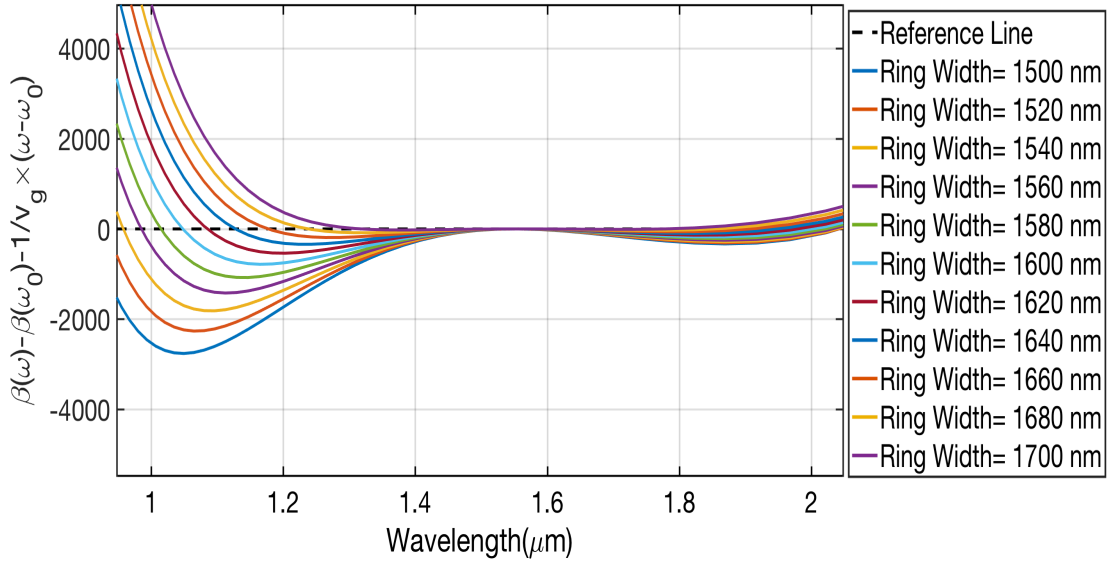


Figure 4.10. Phase Matching Condition Sweep for Dispersive Wave Generation around 740 nm thick and 1600 nm wide SiN Waveguide.

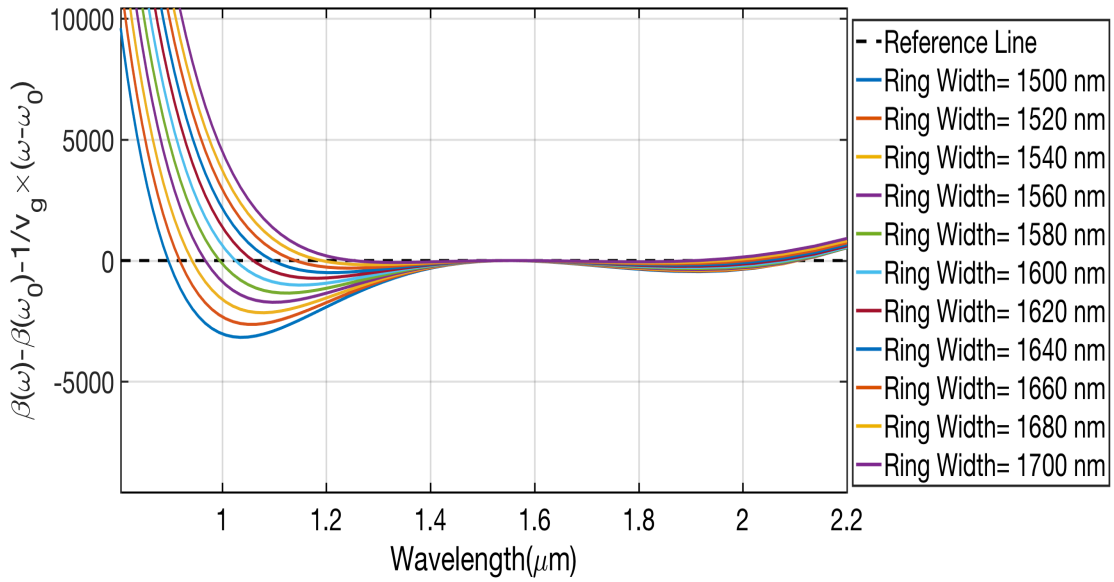


Figure 4.11. Phase Matching Condition Sweep for Dispersive Wave Generation around 745 nm thick and 1600 nm wide SiN Waveguide.

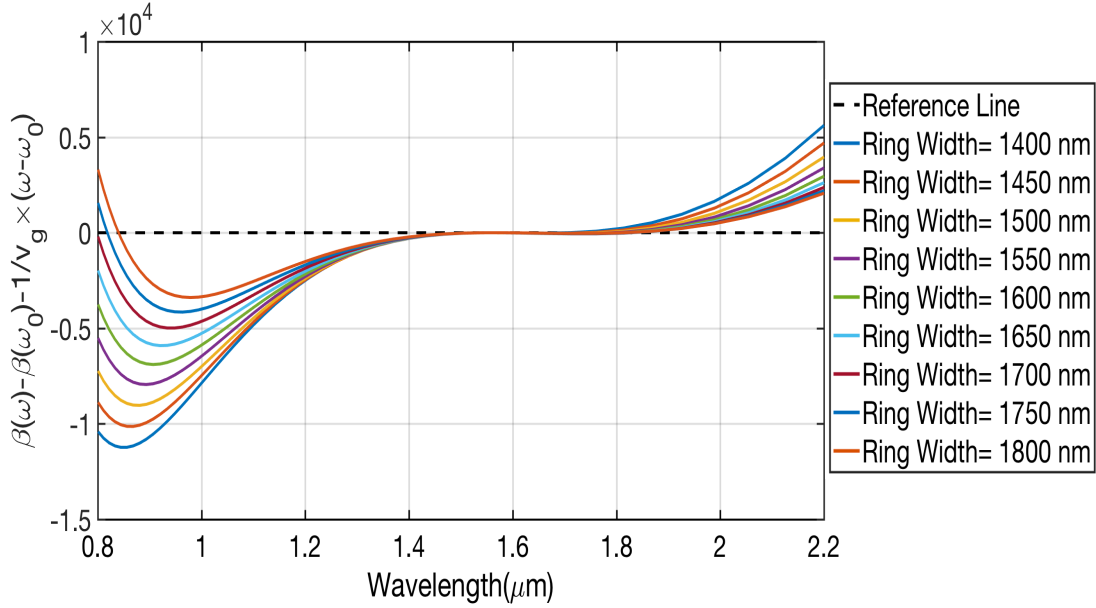


Figure 4.12. Phase Matching Condition Sweep for Dispersive Wave Generation for 680 nm thick waveguide with large bending radius

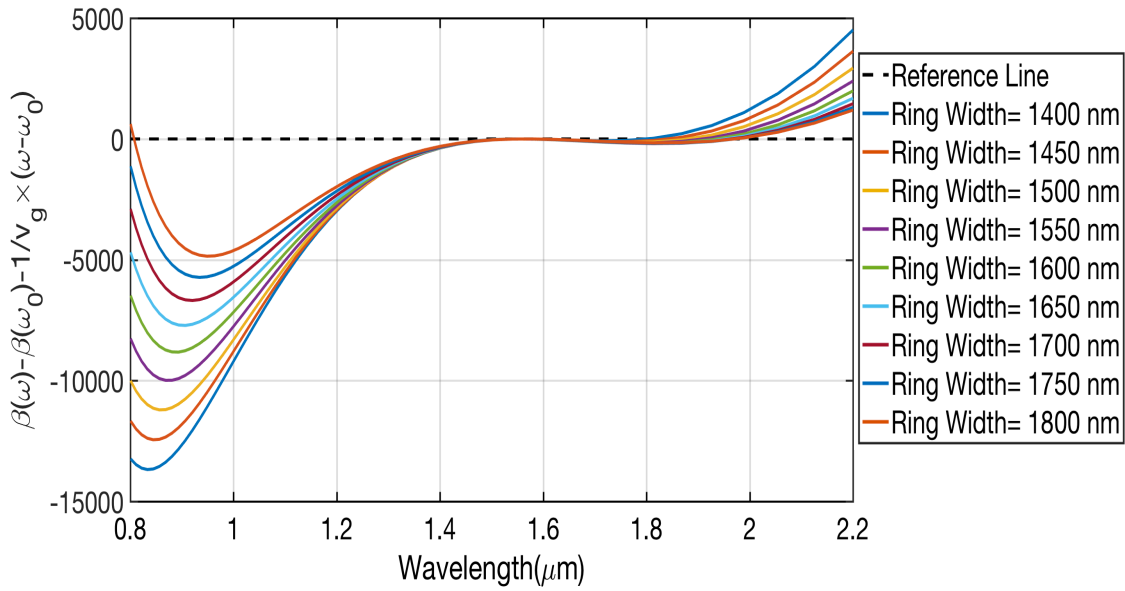


Figure 4.13. Phase Matching Condition Sweep for Dispersive Wave Generation for 690 nm thick waveguide with large bending radius .

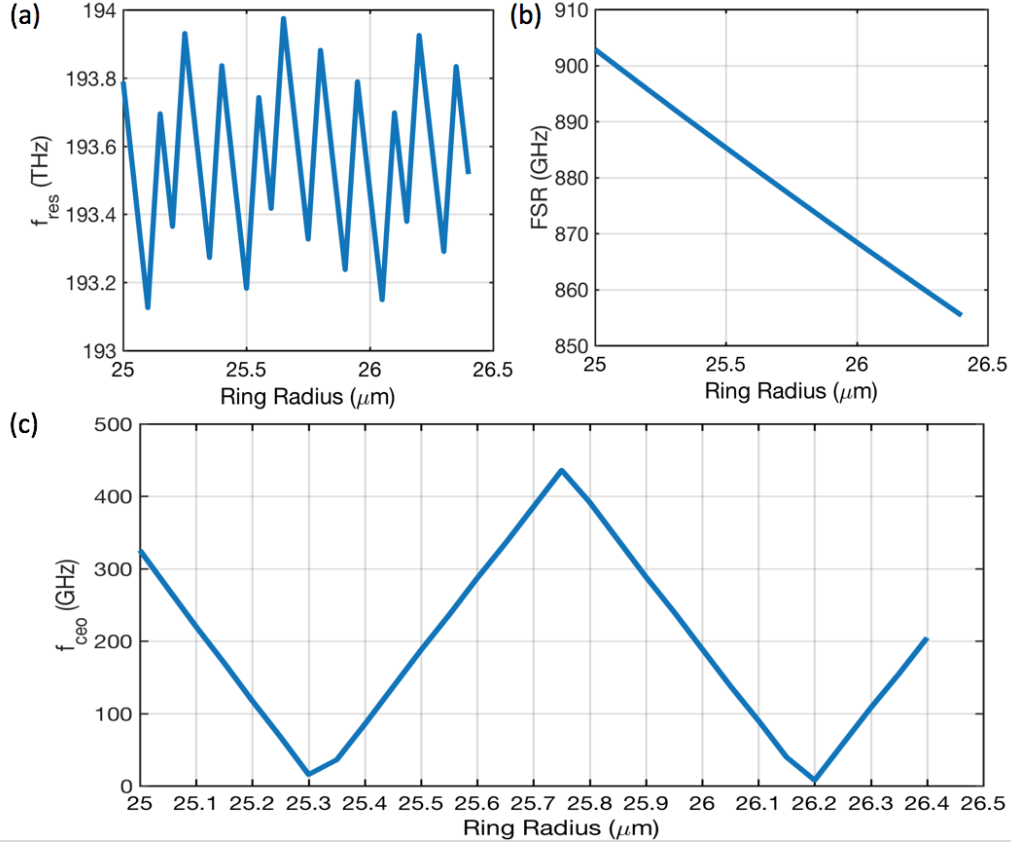


Figure 4.14. Simulated Pump Parameters vs. Ring Radius. (a) Resonance Frequency of the Mode Closest to 1550 nm vs. Ring Radius. (b) FSR of corresponding resonance vs. Ring Radius. (c) Carrier offset frequency vs. Ring Radius.

Because the ring waveguide width and film thickness have been determined based on dispersion engineering. We control the ring radius to modify offset frequency. The ring radius modifies resonance frequency as well as FSR simultaneously and results in the shift in f_{ceo} .

The resonance frequency can be calculated via Eq. 3.1 based on the simulated frequency-dependent effective index. After retrieving the resonance frequency, the corresponding repetition rate can be calculated via corresponding group index based on Eq. 1.1.

An example is given as Fig. 4.14 for a waveguide with $743 \text{ nm} \times 1610 \text{ nm}$ cross section. While varying the ring radius, we choose the mode closest to 1550 nm as our pump resonance and calculate corresponding resonance frequency, mode number and FSR. Here, the mode

number can be different in each radius to approach target pumping wavelength (1550 nm). Fig. 4.14(a)(b) illustrate the simulated f_{res} and FSR when the ring radius is varied from 25 μm to 26.5 μm . Fig. 4.14(c) shows the calculated carrier offset frequency vs. ring radius.

To minimize the f_{ceo} in the simulated waveguide dimension, the ring radius should be chosen around 25.3 μm or 26.2 μm as Fig. 4.14(c) indicating.

4.4.2 Offset Between Simulated and Experimental Device Parameters

Although we try to minimize f_{ceo} and tune the dispersive wave frequency to the desired positions in the design, the fabricated devices can still have a big offset to the design value. The offset can be introduced in the fabrication process by the factors as following.

1. SiN film nonuniformity across the wafer
2. Ring waveguide width offset resulted from e-beam lithography error bar and corresponding ring radius uncertainty
3. Refractive Index nonuniformity across the wafer
4. Offset between measure refractive index and real refractive index due to measurement error bar and extra high temperature annealing process in the fabrication

Additionally, any change of the pump frequency and repetition rate in the soliton generation process shift the carrier offset frequency. The changes are mainly due to the reasons as following [27].

1. Resonance frequency shift and repetition rate change due to thermal heating induced by intracavity power.
2. Repetition Rate shift due to detuning change
3. Repetition Rate shift due to pump power change

For example, Table. 4.1 lists the simulated repetition rate and measured repetition rate of solitons generated on SiN microring resonator with around 25 μm ring radius. All the

devices in this table are fabricated on the same wafer with different ring widths (w_{ring}), chip location-based film thicknesses (h_{ring}) and designed ring radius (r_{ring}). The simulated repetition rates ($f_{rep-simlated}$) are calculated based on simulated group index and ring radius. The measured repetition rates ($f_{rep-measured}$) are measured by electro-optic down conversion after soliton generation.

Table 4.1. Comparison of Designed and Measured Repetition Rate of Microring Resonator with $\sim 25 \mu\text{m}$ Radius

Device	w_{ring} (nm)	h_{ring} (nm)	r_{ring} (μm)	$f_{rep-simlated}$ (GHz)	$f_{rep-measured}$ (GHz)
$C_{25}D_{20}$	1610	738	25.309	891.499	894.180
$C_{25}D_{24}$	1620	738	25.374	889.281	892.001
$C_{25}D_{25}$	1620	738	25.374	889.281	891.923
$C_{45}D_{14}$	1660	736	25.497	889.219	887.828
$C_{46}D_{15}$	1600	736	25.860	872.611	875.847
$C_{46}D_{18}$	1600	736	25.940	869.993	872.637
$C_{46}D_{19}$	1600	736	25.940	869.993	872.682
$C_{46}D_{20}$	1600	736	25.940	869.993	872.480

4.5 Design Parameter Sensitivity for Dispersion Engineering

4.5.1 Parameter Sensitivity in the device design

To investigate the effect of important design parameters on the device performance, we conduct several simulations to evaluate the parameter sensitivity. Ring waveguide width, SiN film thickness, ring radius are simulated with 10 m (5 nm) step to investigate the influence on the dispersive wave frequencies (low frequency side DW 1 and high frequency side DW 2), pump frequency (f_{res}), repetition rate (f_{rep}) and carrier offset frequency (f_{ceo}). In each simulation, other parameters are kept same.

For example, to evaluate the parameter sensitivity of ring width. In the waveguide simulation, a serials of ring widths with 10 nm step is swept while the film thickness, ring radius, chip temperature are using the same value. The pump frequency is calculated for a fixed mode number to compare the frequency shift. The repetition rate and carrier offset frequency are calculated corresponding to this pump frequency. The dispersive wave fre-

quencies at both low frequency side (DW1) and high frequency side (DW2) are calculated to obtain the dispersive wave frequency shift. For better accuracy, the pump related parameters (f_{res} , f_{rep} and f_{ceo}) are simulated with a fine sweep around pump wavelength (1550 nm) while the dispersive wave frequencies are simulated in a large band (800 nm to 2200 nm).

The summarized parameter sensitivity is listed as below for a 25 μm radius ring waveguide with 740 nm thick and 1600 nm wide cross section.

Table 4.2. Parameters Sensitivity. DW 1: Dispersiv Wave 1. DW 2:Dispersive Wave 2.

Waveguide Parameters	f_{DW1}	f_{DW2}	f_{res}	f_{rep}	f_{ceo}
Waveguide Width Per 10 nm	+1 THz	-4.7 THz	-54 GHz	+40 MHz	67 GHz
Film Thickness Per 5 nm	-6 THz	+7 THz	-100 GHz	-60 MHz	92 GHz
Ring Radius Per 10 nm	+128 GHz	+0.22 THz	-66 GHz	-355 MHz	10.4 GHz
Temperature(Per Degree)	-16 GHz	+30 GHz	-2.6 GHz	-14 MHz	400 MHz

4.5.2 Compensations for the Offset Between Simulation and Fabrication

As shown in Table 4.2, the dispersive wave frequencies and f_{ceo} are very sensitive to the design parameters. Therefore, we need compensate the offset to achieve our target. There are typically two approaches; sweeping the design parameters in the design and dynamic thermal tuning.

The direction of offsets in the fabrication are unknown. Therefore, we need to take both shifting directions of the parameters into consideration. For ring waveguide width and ring radius, which are defined in the waveguide pattern layouts, we could do a fine sweep to hit the correct value.

For the film thickness, the effect of non-uniformity can be reduced by creating a thickness map as Fig. 4.15. The local thicknesses are measured across the wafer for each chip. Then we optimize the design parameters (ring waveguide width and ring radius) according to the local chip thickness.

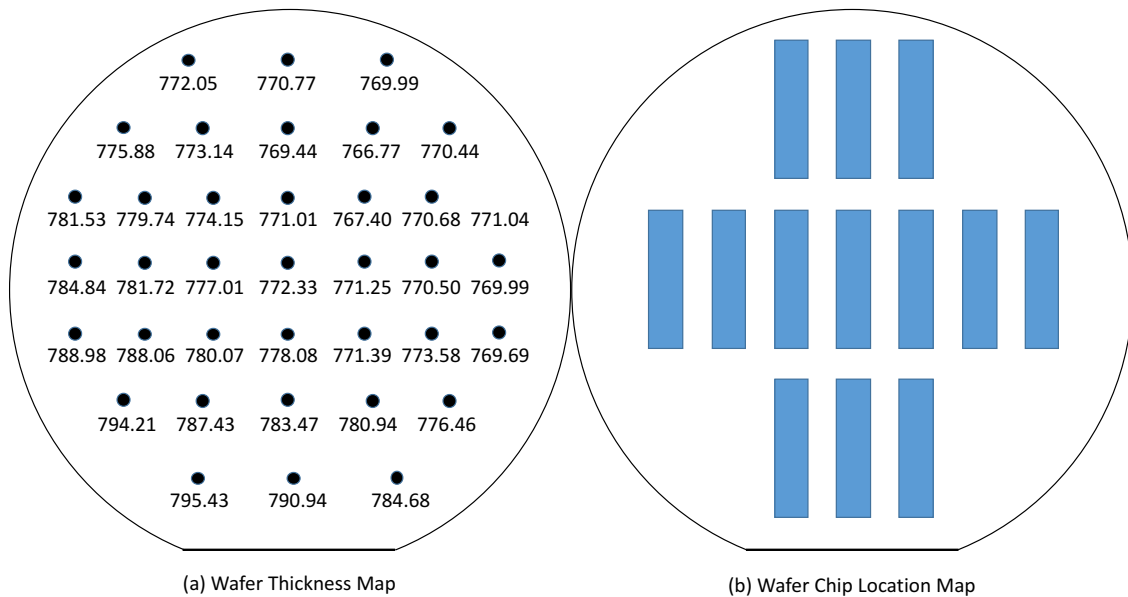


Figure 4.15. SiN Wafer Thickness Map. (a) Measured thickness across the wafer (b) Chip Distribution Locations on the SiN wafer. The thickness map is measured by Abdullah Al Noman

Another approach is tuning the f_{pump} and f_{rep} via on-chip heater to compensate the difference. As shown in Chapter 3, we can tune the carrier offset frequency by the thermal tuning.

4.6 Realization of Octave-spanning Kerr Soliton

In this section, we will discuss the demonstration of the on-chip octave-spanning soliton with SiN microring resonator with cladding.

4.6.1 Device for Octave-spanning Frequency Comb Generation

For a target wafer thickness, 740 nm, we sweep the ring waveguide from 1560 nm to 1640 nm with a 20 nm step. The ring radius of ring 1 is chosen to be 25.322 μm and 26.249 μm for low carrier offset frequency.

A pulley shape bus waveguide, where the bus waveguide in the bus-ring coupling regime is also a bending waveguide is used to enhance the coupling efficiency of 1 μm and 2 μm light [63].

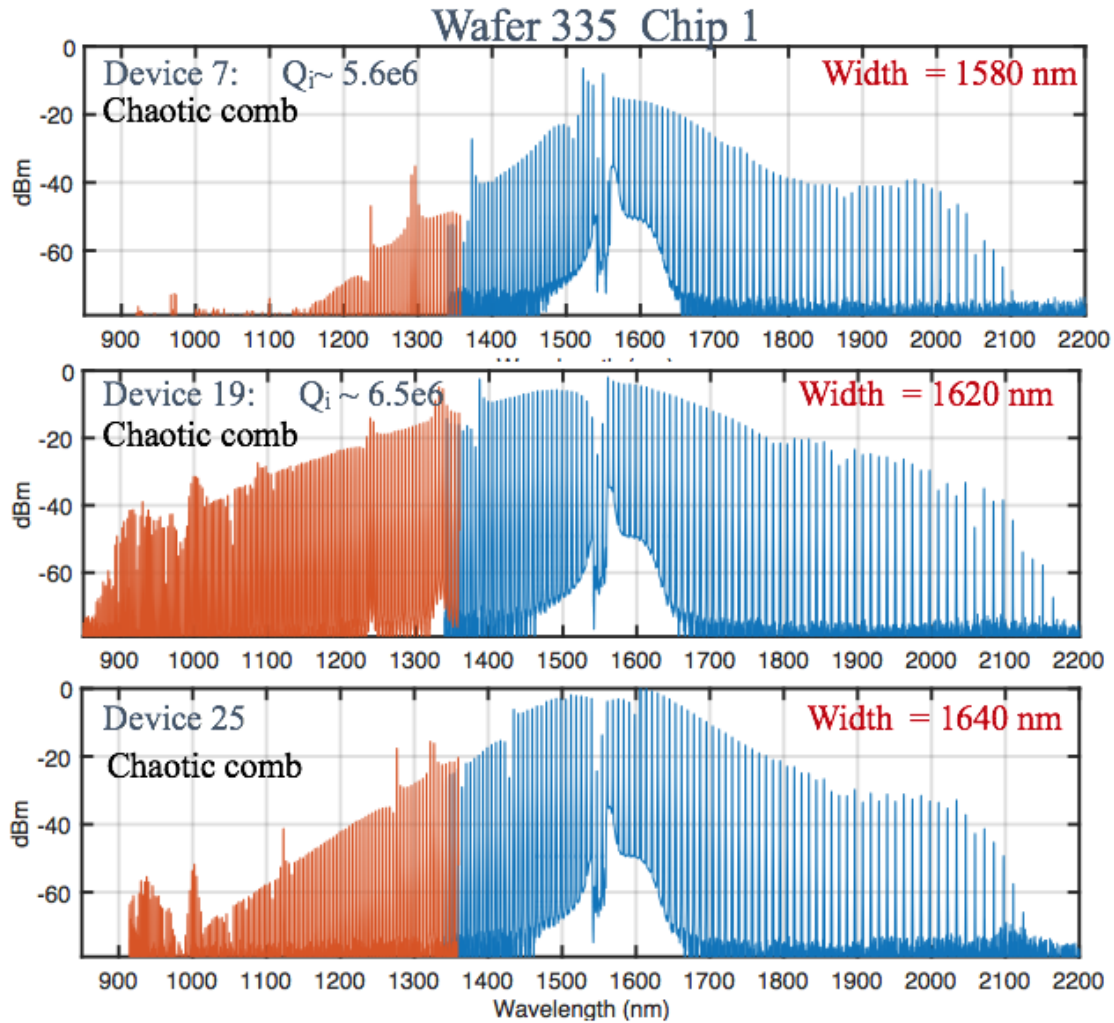


Figure 4.16. Chaotic Broadband Frequency Comb Generated on SiN Microring Resonators Wafer 335. The devices are fabricate by Zhichao Ye (Chalmers University of Technology). (Image courtesy: Mohammed S. Alshaykh)

Two sets of SiN microring resonators are fabricated on two wafers (wafer 335 and wafer 343) of the same film thickness. To verify the bandwidth of frequency comb, the chaotic combs are generated on the devices. Fig. 4.16 shows a series of comb generated with different ring widths. The comb bandwidth is very sensitive to the ring waveguide width variation.

The soliton steps are measured to be several tens of nanoseconds for the octave-spanning combs.

In Fig. 4.16, the pumps are attenuated by a coarse wavelength division multiplexing (CWDM). The red and blue parts represent the optical spectrum traces taken from two different OSAs due to the large bandwidth. To calibrate the sensitivity difference between the OSAs, the traces are taken with around 150 nm overlap section.

4.6.2 Octave-spanning Soliton Generation

To access the stable soliton regime, a fast pump tuning method is used to access the soliton [64]. The continuous-wave (CW) pump is modulated via a single-sideband (SSB) modulator to suppress the pump and enhance the sideband. Then the sideband is swept by a voltage-controlled oscillator with a ramp generated by an arbitrary waveform generator.

The octave-spanning solitons are generated on several devices with ring width of 1620 nm or 1640 nm as shown in Fig. 4.17.

Although the comb bandwidths in Fig. 4.17 are achieved to be one octave, the optical power of comb lines at dispersive wave are relative small (around -50 dBm at low wavelength side). To increase the power of dispersive wave, additional fabrication is performed with lower film thickness to achieve maximum -32 dBm at low wavelength dispersive wave (see Fig. 4.18).

4.7 Discussion

In this Chapter, we achieved octave-spanning soliton generation on the SiN microring resonators via optimizing the waveguide design parameters based on dispersion engineering. The octave-spanning solitons can be utilized in applications like atomic clock to provide a fully-stabilized frequency comb source if we could lock the repetition rate and carrier offset frequency of the soliton. However, the repetition rate of the achieve octave-spanning soliton is about 900 GHz, which is far beyond the detection range of electronic equipment. Therefore, we would discuss the approaches of divide the large repetition rate of an octave-spanning comb to a detectable range in the following chapters.

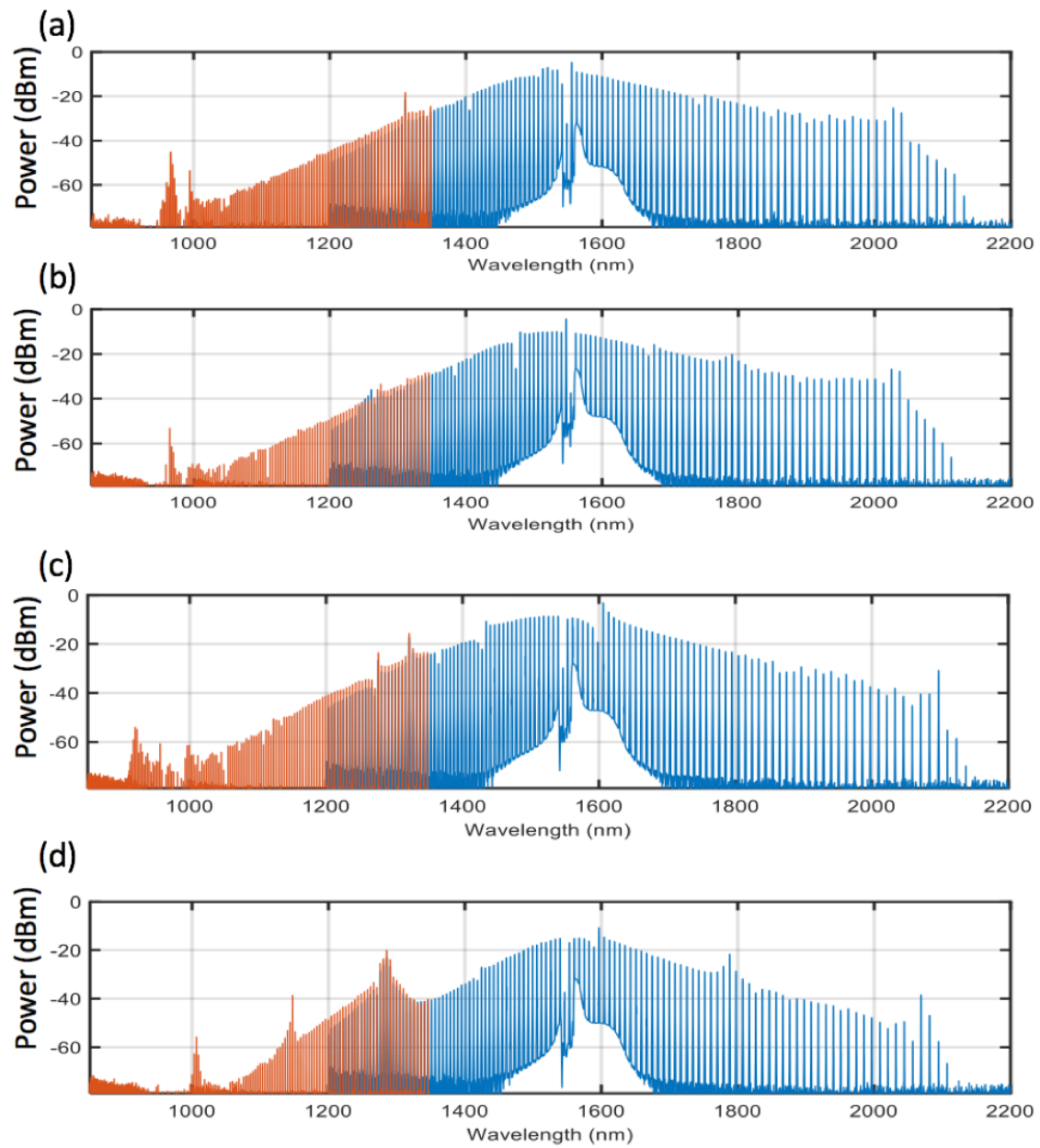


Figure 4.17. Octave-spanning Solitons Generated on Various of SiN Devices (Image courtesy: Nathan O'Malley)

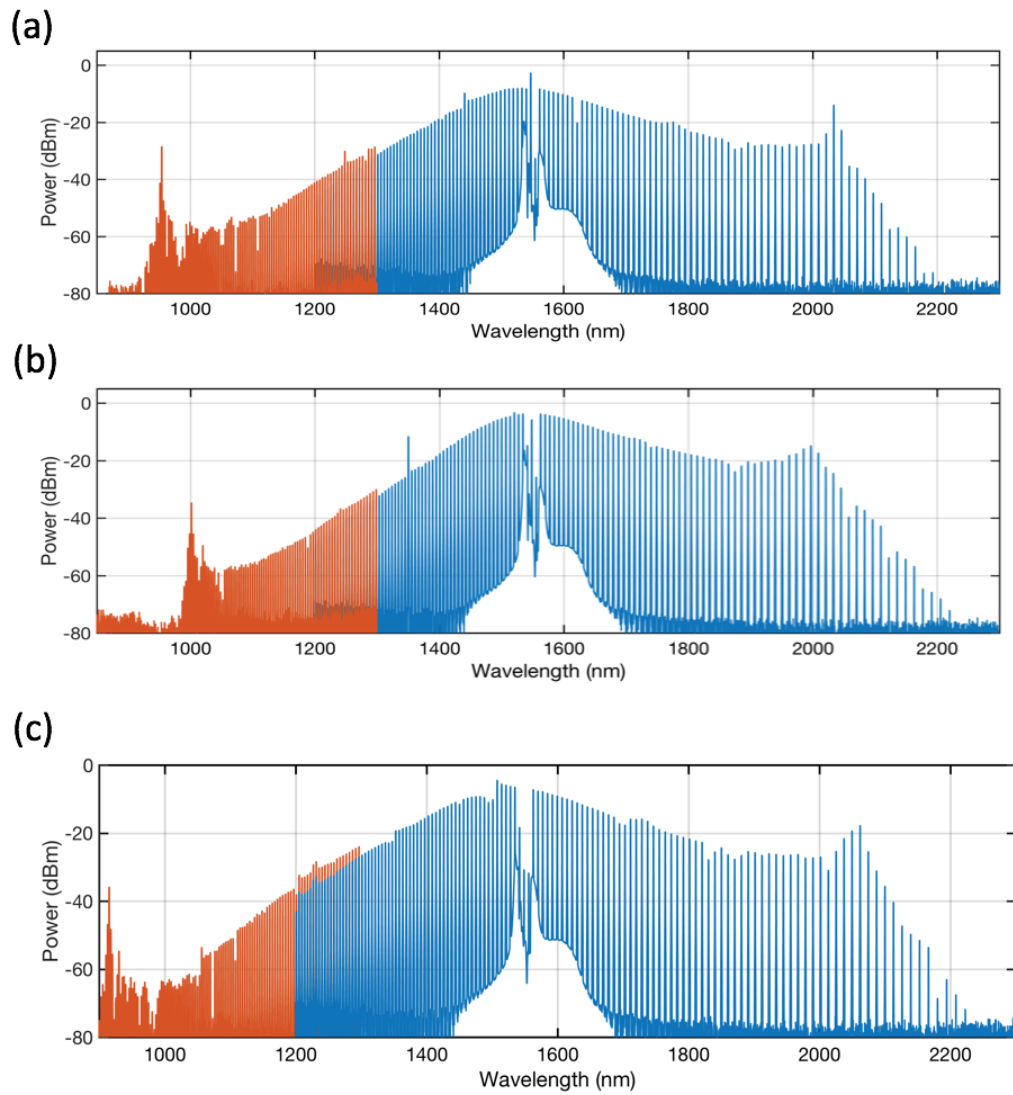


Figure 4.18. Octave-spanning Solitons Generated on Various of SiN Devices around Succeeded Parameters in Last Fabrication Run (Devices Fabricated by Marcello Girardi)

5. OPTICAL DIVISION OF OCTAVE-SPANNING SOLITON ON AN ALL-SILICON NITRIDE PLATFORM

In chapter 4, the on-chip octave-spanning soliton is achieved via dispersion engineering on the SiN microrings. However, the repetition rate of octave-spanning comb is far beyond the electronic detection range, which prohibits the locking of the repetition rate of the frequency comb. A divided version of the large repetition rate is desired towards the stabilization of the comb¹.

5.1 Optical Division of a Large Repetition Rate Comb

5.1.1 Conventional Optical Division Methods

In conventional schemes, large repetition rate of a frequency comb can be divided via electro-optic modulation or mixing with a stabilized low repetition rate fiber frequency comb as shown in Fig. 5.1. Fig. 5.1(a) shows EO comb lines generated from Kerr comb lines (red) overlap with each other and provide a readable beat note. Fig. 5.1(b) represents the beat between large repetition rate Kerr comb (blue) and a small repetition rate fiber comb (red).

However, those methods include large volume components that prevent them from using outside of the laboratory.

5.1.2 Integrated Optical Division Methods

Instead of fiber frequency comb, a low repetition rate Kerr frequency soliton can serve as the auxiliary comb with much a more compact size and lower power requirements.

However, as the comb generation threshold power is proportional to $\frac{1}{f_{rep} \cdot Q^2}$. Ultra-high Q is required to compensate the significant decreasing f_{rep} in the FSR of the rings. In 2019, NIST reported a measurement of the repetition rate of a THz octave-spanning soliton in a SiN microring via the beat signal with a 22 GHz narrow bandwidth soliton in a silica whispering-gallery-mode (WGM) microresonator [66] since WGM microresonator has an ultra high Q \sim 360 million. This frequency division scheme provided a route for an on-chip

¹The results shown in this chapter was published in [65]

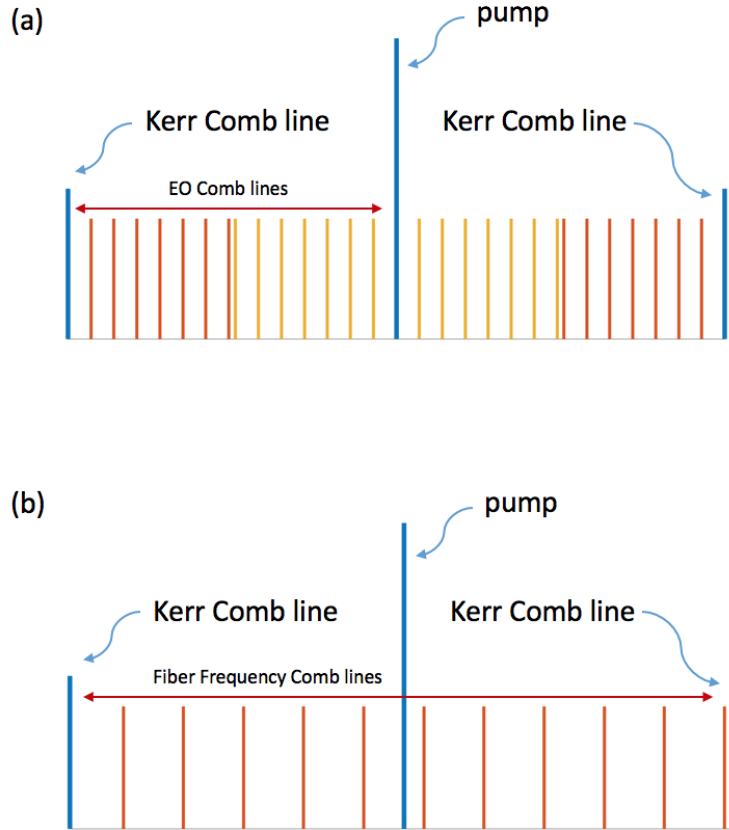


Figure 5.1. Conventional Schemes of Optical Division. (a) Electro-optic modulation of a frequency comb via a low repetition rate RF modulation signal. (b) Beat frequency comb with a low repetition rate fiber-based frequency comb

stable frequency source. However, the two devices are fabricated with different material and require different pumping wavelength. Those requirements significantly increase the complexity of integration.

5.1.3 Integrated Optical Division on All-SiN Platform

Thanks to the development in the ultralow-loss SiN waveguide fabrication process, the high Q small FSR SiN microring resonators are realized [67] to overcome the requirement for high pump power to excite low repetition rate solitons.

We demonstrate the on-chip optical division, to the best of our knowledge, the first use of a auxiliary soliton microcomb to read out the repetition rate of an octave-spanning

soliton fully based in silicon nitride (SiN). The octave-spanning ring and the auxiliary ring are fabricated on the films of same thickness. For the integration purpose in the future, both rings can be fabricated on the same chip. The common platform provides a potential small footprint, homogeneous way of integrated optical division of a large repetition rate octave-spanning soliton, which reduces the fabrication cost and difficulty in the integration.

Additionally, the octave-spanning comb and the auxiliary comb is able to share the common pump laser via thermal tuning as shown in Fig. 5.2.

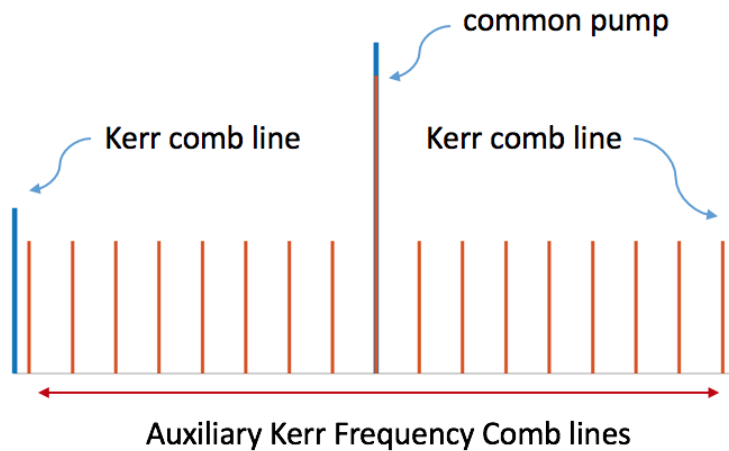


Figure 5.2. Overlap for Octave-spanning Comb and Auxiliary Comb with Common Pump

Compared to using two independent CW pump lasers, the common pump approach has the benefits as below.

1. Only one laser is need in the photonic integrated circuits
2. No need to lock the two independent laser frequencies
3. The beat note between two Kerr combs are symmetric on both sides of the pump, which could provide twice the beat signal power

5.2 Optical Division Scheme with a Low Repetition Rate Auxiliary Ring

5.2.1 Retrieving Large Repetition Rate via Beat Signal

In this chapter, a low repetition rate (f_l) Kerr frequency comb (comb 1), is used as an auxiliary ring to read out the repetition rate (f_o) of octave-spanning comb (comb 2). f_l is chosen as 25 GHz, which is within the common detect bandwidth of photodiode.

If we combine comb 1 and comb 2, two beat notes, f_{b1} and f_{b2} can be detected by a 25 GHz bandwidth photodetector. The first beat, f_{b1} is the repetition rate of the low repetition rate comb, which can be detected directly by sending the frequency comb to a fast photodiode as Eq. 5.1.

$$f_{b1} = f_l \quad (5.1)$$

The second beat is the overlap beat between two Kerr combs, which can be calculated as Eq. 5.2. N is a integer number representing the number of comb lines of comb 1 between two consecutive comb lines from comb 2.

$$f_{b2} = f_o - N \cdot f_l \quad (5.2)$$

After obtaining the value of f_{b1}, f_{b2} and N from measurement, f_o can be calculated as Eq. 5.3.

$$f_o = f_{b2} + N \cdot f_{b1} \quad (5.3)$$

As with any optical heterodyne measurement, there is a +/- ambiguity in the overlap beat. This ambiguity can be resolved by dithering the repetition rate of the 25 GHz comb via pump power control.

5.3 Devices for Optical Division

5.3.1 Device1: Octave-spanning Device

The 900 GHz octave-spanning soliton is generated on one of the SiN devices mentioned in section 4.6. The SiN film thickness and ring waveguide width are carefully dispersion

engineered to achieve dispersive wave generate at $1\ \mu\text{m}$ ($2\ \mu\text{m}$) as well as low pump dispersion at the same time.

The waveguide dimension for octave-spanning device (ring 1) is $740\ \text{nm} \times 1640\ \text{nm}$. The film thickness is chosen as $740\ \text{nm}$ for low local dispersion at pump wavelength $\sim 1550\ \text{nm}$ for $25\ \mu\text{m}$ ring radius. The ring width is chosen as $1.64\ \mu\text{m}$ to achieve dispersive wave generation around $1\ \mu\text{m}$ and $2\ \mu\text{m}$. The intrinsic Q of ring 1 is 4×10^6 .

As shown in Fig. 5.3 left, a integrated heater ($200\ \text{nm}$ Platinum) is deposited on top of the cladding to enable thermal tuning to align the pump resonances of two rings. The heater width is $10\ \mu\text{m}$.

5.3.2 Device2: 25 GHz Device

Fig. 5.3 right is the device 2 for low repetition rate auxiliary soliton (Designed by our collaborator Zhichao Ye from Chalmers University of Technology).

The low repetition rate comb need only span the C band, which is easy to realize with thick films that result in anomalous dispersion, provided that sufficiently high Q is available. Therefore, to explore the possibility of integrated both devices on same chip to realize μm scale small footprint, the thickness of device 2 is chosen to be same as device 1.

On the other hand, the requirement in terms of Q factor for device 2 is much higher compared to device 1 since the comb generation threshold power is proportional to $\frac{1}{f_{rep} \cdot Q^2}$.

Except for precise control and optimizing the fabrication process to reduce waveguide scattering-induced loss, special bending design is also included to reduce straight-bend waveguide transition loss and mode coupling between fundamental mode and higher order mode [68].

Here we include platinum integrated heater on device 2 as well to add extra tunability of the solitons. In the experiment, one of the on-chip heater is used to align the resonance frequency of both rings allowing the single CW pump. The second heater can be used to tune the carrier offset frequency.

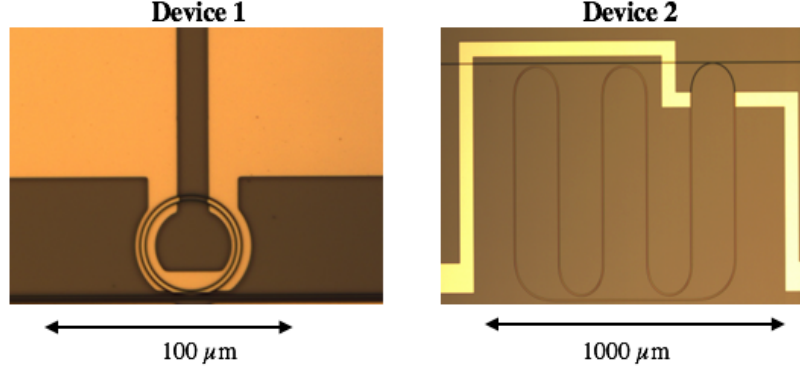


Figure 5.3. Image of SiN Microring Resonator for Optical Division of Octave-spanning Soliton Fabricated by Zhichao Ye. Left: Device 1 (900 GHz SiN Microring). Right: Device 2 (25 GHz SiN Microring) [65].

5.4 Demonstration of Optical Division of 900 GHz Octave-spanning soliton with a 25 GHz soliton

5.4.1 Simultaneous Soliton Generation via Fast Pump Tuning

Similar methods with a rapid pump frequency tuning as chapter 4 is used to generate solitons. This time, the modulated pump is split into two paths via a 50:50 fiber optic coupler. Each path is routed through an erbium-doped fiber amplifier (EDFA) to provide high pump power for SiN microrings as shown in Fig. 5.4. Polarization controllers are placed before each ring to control the polarization of each route independently.

At room temperature, device 1 is pumped with ~ 840 mW input power (at amplifier) at ~ 1548.3 nm. Device 2 is pumped with ~ 580 mW input power (at amplifier) at 1548.45 nm. To simultaneously pump the both devices with a common CW laser, 12 mW electric power is applied on the microheater of device 1 to align the resonances on the two devices. Thermo-electric cooling control is installed on the sample mount of both devices to control the chip temperature. The AWG sweep function is tailored to sit the modulated pump in soliton generation range of both devices.

The optical spectra of generated solitons are shown in Fig. 5.5 for device 1 and device 2. The spectra are taken at the reflecting port of CWDM (DWDM) to suppress the strong

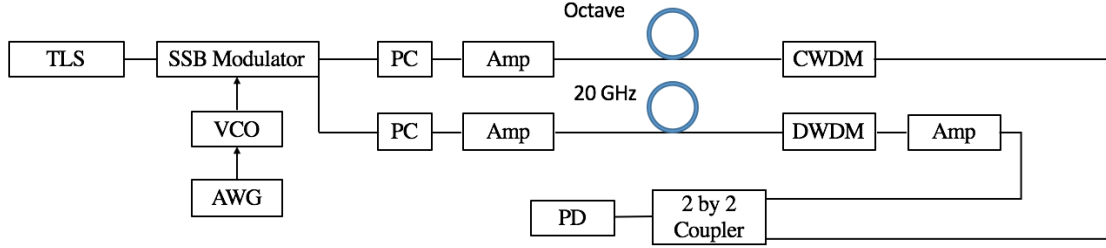


Figure 5.4. Set-up for optical division with a low repetition rate micro-comb. TLS: tunable laser. SSB: single-sideband. VCO: voltage control oscillator. AWG: arbitrary waveform generator. PC: polarization controller. Amp: optical amplifier. CWDM: coarse wavelength division multiplexer. DWDM: dense wavelength division multiplexer.

pump line. Since the bandwidth of octave spanning soliton is beyond the span of one OSA, Fig. 5.5.a is combined by two spectra taken by two OSAs with different recording range with a overlap recording window to calibrate the power sensitivity sensitivity between two OSAs.

The octave-spanning comb (Fig. 5.5.Blue) spans from 1000 nm to 2000 nm with relatively weak dispersive waves.

It is worth noting the comb power of 25 GHz soliton is much lower compared to 900 GHz soliton. It is due to the denser comb lines and a much weaker coupling between bus waveguide and ring waveguide in the 25 GHz ring.

5.4.2 Overlap Beat Detection

Due to the low power levels of the 25 GHz soliton comb, comb 2 is amplified by a EDFA before optically combining with the octave comb via a 50:50 2 by 2 optical fiber coupler. A fast photodiode is used to record the overlap beat as well as the beat note of 25 GHz microcomb(Fig. 5.5a) at the same time.

Here, the second overlap beat is shown in Fig. 5.6b) because the first overlap beat is attenuated by CWDM. So the Eq. 5.3 can be modified as $f_o = f_{b2}/2 + N \cdot f_{b1}$.

The relatively broad beat in 5.6b is presumed to be caused by the drifting of the unlocked combs' repetition rates.

In this case, $f_{b1}=24.93928$ GHz and $f_{b2}=-1.043$ GHz. The sign of overlap beat, f_{b2} , is obtained when dithering the repetition rate of 25 GHz soliton via modifying the pump power. The mode number N is 36 counted from optical spectrum overlapping as shown in Fig. 5.5. Therefore, the repetition rate of octave-spanning comb can be calculated as below.

$$f_o = 36 \times 24.93928 \text{ GHz} - 1.043 \text{ GHz}/2 = 897.2926 \text{ GHz} \quad (5.4)$$

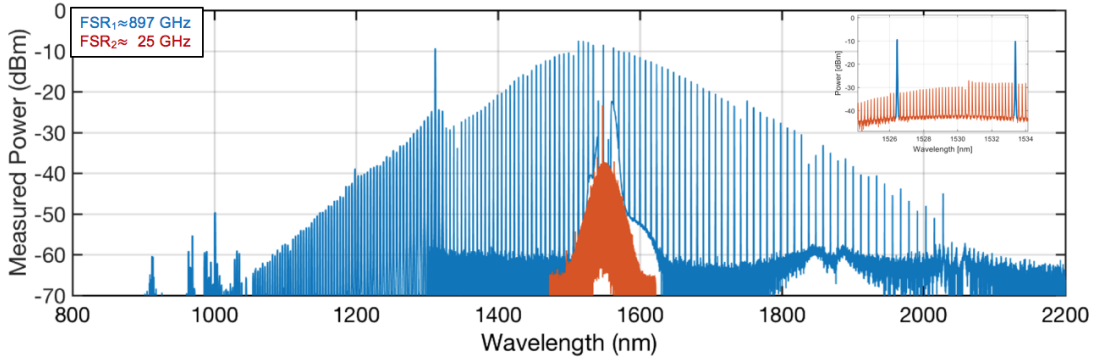


Figure 5.5. Optical Spectra of Simultaneous Pumping Solitons. Blue: Octave-spanning soliton. Red: Low repetition rate soliton

To justify the repetition rate measurement, the repetition rate is measured via electro-optic (EO) modulation method as mentioned in [69].

5.4.3 Verification of Repetition Rate via Electric-optic Modulation

A consecutive of two amplified Kerr comb lines at the reflecting ports of CWDM (DWDM) are selected via bandpass filter and sent to a EO comb generator [70] after going through an amplifier.

Each sideband serves as a pump source to generate EO comb lines with the spacing of modulation frequency.

Only overlapping lines between two generated EO comb lines are picked up via a programmable wave shaper and sent to a photodiode to avoid unwanted signal induced noise.

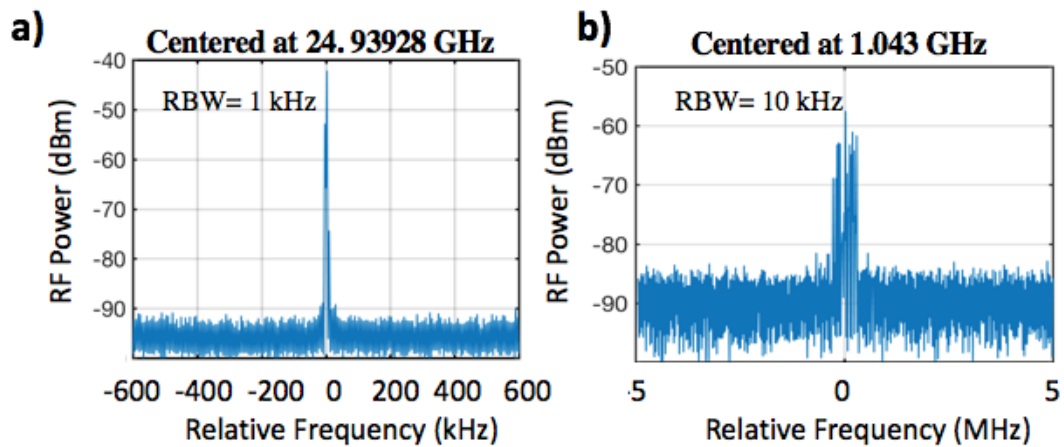


Figure 5.6. Electric Spectra of Beat notes. a) Measurement of repetition rate of 25 GHz soliton b) Measurement of overlap beat note between Octave-spanning soliton and 25 GHz soliton [65].

Then the overlap beat frequency can be read via an electric spectrum analyzer as shown in Fig. 5.7.

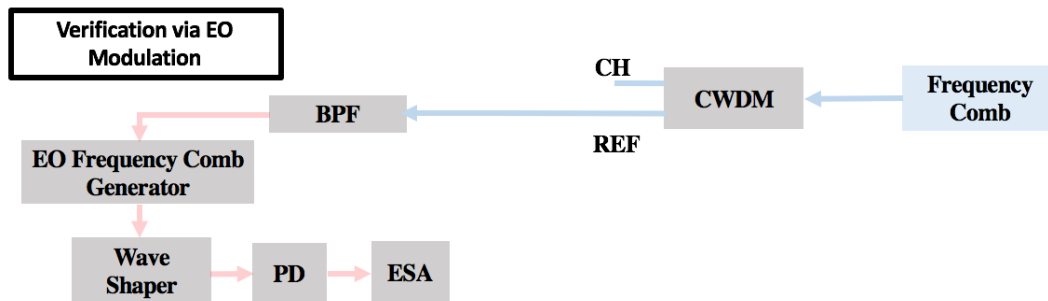


Figure 5.7. Set-up for EO Comb Verification. CH: channel port of CWDM. REF: reflecting port of CWDM. BPF: bandpass filter. PD: photodetector. ESA: electric spectrum analyzer.

In this scheme, the spacing between two Kerr comb sidebands can be calculated as Eq. 5.5. Where f_{EOb} , N_2 and f_{EOm} are EO comb beat frequency, the number of EO comb lines between two Kerr comb lines and the EO comb repetition rate, respectively.

$$f_o = f_{EOb} + N_2 \cdot f_{EOm} \quad (5.5)$$

Here, the EO comb is driven at 17 GHz. The number of modes between two Kerr comb lines is 53. The overlap frequency of EO comb is measured to be -3.708 GHz (the sign is obtained via dithering the EO comb modulation frequency).

Hence, the repetition rate of octave-spanning soliton is measured to be 897.292 GHz as Eq. 5.6.

$$f_o = -3.708 \text{ GHz} + 53 \times 17 \text{ GHz} = 897.292 \text{ GHz} \quad (5.6)$$

The two measurements agree at ~ 1 MHz level, which justify the optical division via a low repetition rate soliton [65].

5.5 Summary

In this Chapter, a 900 GHz octave-spanning soliton and a 25 GHz soliton are simultaneous generated on all-SiN platform with a common pump source. The beat note between two solitons provides a on-chip divided version of large repetition rate of octave-spanning.

We retrieve the repetition rate of the generated octave-spanning soliton, and verify the results by EO comb modulation.

6. OPTICAL DIVISION OF OCTAVE-SPANNING SOLITON WITH A VERNIER BROADBAND SOLITON

In this chapter, we will discuss an alternative scheme for on-chip optical division of a large repetition rate octave-spanning comb, where the auxiliary ring is a large FSR microring. The large FSR reduces the requirement of quality factor of the ring waveguide and the devices' footprint for the whole system compared to using a small FSR auxiliary ring ¹.

6.1 Optical Division with a Vernier Soliton

6.1.1 Retrieve Repetition Rate via Beat Notes

In this scheme, both rings have large FSR around 900 GHz with a small difference (df_{rep}) around 20 GHz as Eq. 6.1, where f_{rep1} and f_{rep2} are the repetition rates of ring 1 and ring 2, respectively.

$$df_{rep} = f_{rep1} - f_{rep2} \quad (6.1)$$

When both rings share a common pump (f_{pump}), the combs' first sidebands will generate a beat note with frequency df_{rep} . As the combs' sidebands gradually walk off and finally overlap M_v modes away from the pump at frequency $f_{overlap1} = f_{pump} \pm M_v \times f_{rep1}$ for comb 1 and $f_{overlap2} = f_{pump} \pm (M_v + 1) \times f_{rep2}$ for comb 2 to generate a overlap beat (f_{bover}) as shown in Fig. 6.1.

Fig. 6.1 (a) and Fig. 6.1(b) are the two overlap points between two combs. The overlap beats can be derived as below (assuming we measure at the low wavelength side).

$$f_{overlap1} = f_{pump} + M_v \times f_{rep1} \quad (6.2)$$

$$f_{overlap2} = f_{pump} + (M_v + 1) \times f_{rep2} \quad (6.3)$$

$$f_{bover} = f_{overlap1} - f_{overlap2} = M_v \times f_{rep1} - (M_v + 1) \times f_{rep2} \quad (6.4)$$

¹The results shown in this chapter was published in [69]

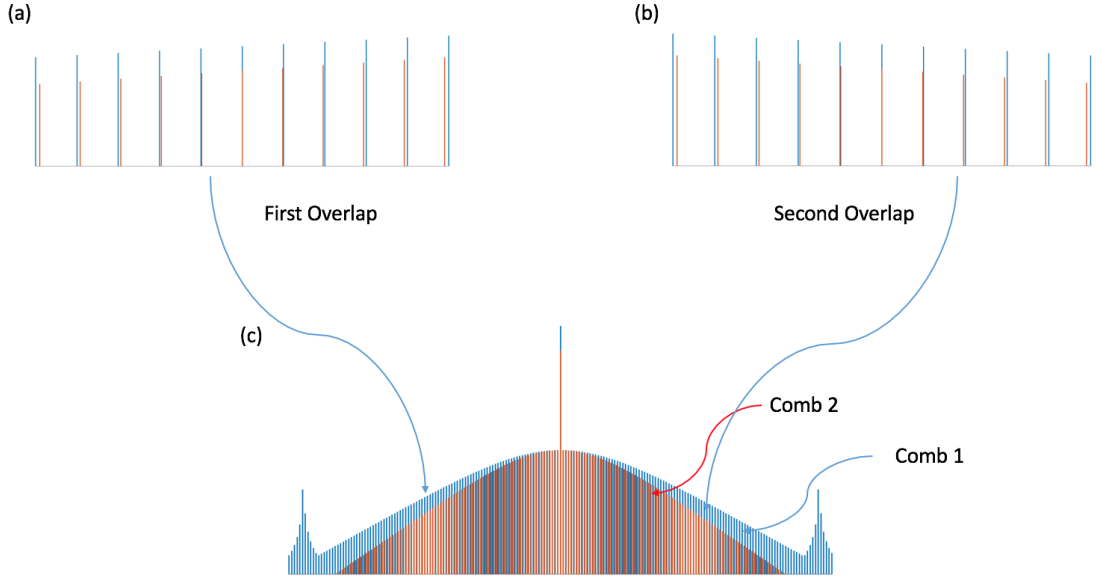


Figure 6.1. Vernier Approach of Optical Division. Blue: Comb 1 (Octave-spanning comb). Red: Comb 2 (Auxiliary Comb) (a) Low frequency overlap between two combs. (b) High frequency overlap between two combs. (c) Optical spectra example of two combs

Combining Eq. 6.1 and Eq. 6.4, the repetition rate of ring 1 and ring 2 can be derived as the following equations based on the value of two beat notes.

$$f_{rep1} = (M_v + 1) \cdot df_{rep} - f_{bover} \quad (6.5)$$

$$f_{rep2} = M_v \cdot df_{rep} - f_{bover} \quad (6.6)$$

6.1.2 Choice of Repetition Rate Difference

Since the overlap locations ($f_{overlap1}$ and $f_{overlap2}$) are determined by mode number M_v , which is the closest integer to f_{rep1}/df_{rep} , the choice of df_{rep} is the key point to make the two required beat notes detectable.

When df_{rep} is too large, f_{rep1} is beyond the detection range. When df_{rep} is too small, overlap location will be far away from pump, which increases the requirement for comb

bandwidth. As shown in Fig. 6.2, the overlap frequency at longer wavelength side will fall beyond 2000 nm when df_{rep} is smaller than 17 GHz.

To meet the abovementioned requirements, we choose the repetition rate difference to be 20 GHz (for 900 GHz octave-spanning comb), which is reachable by fast photodetector. Also, the overlap frequency is anticipated to locate around 1280 nm and 2000 nm if the pumping wavelength is around 1550 nm, which are both reachable for an octave-spanning comb. Due to the limitation of our current photodetector, we detect the overlap beat ~ 1280 nm.

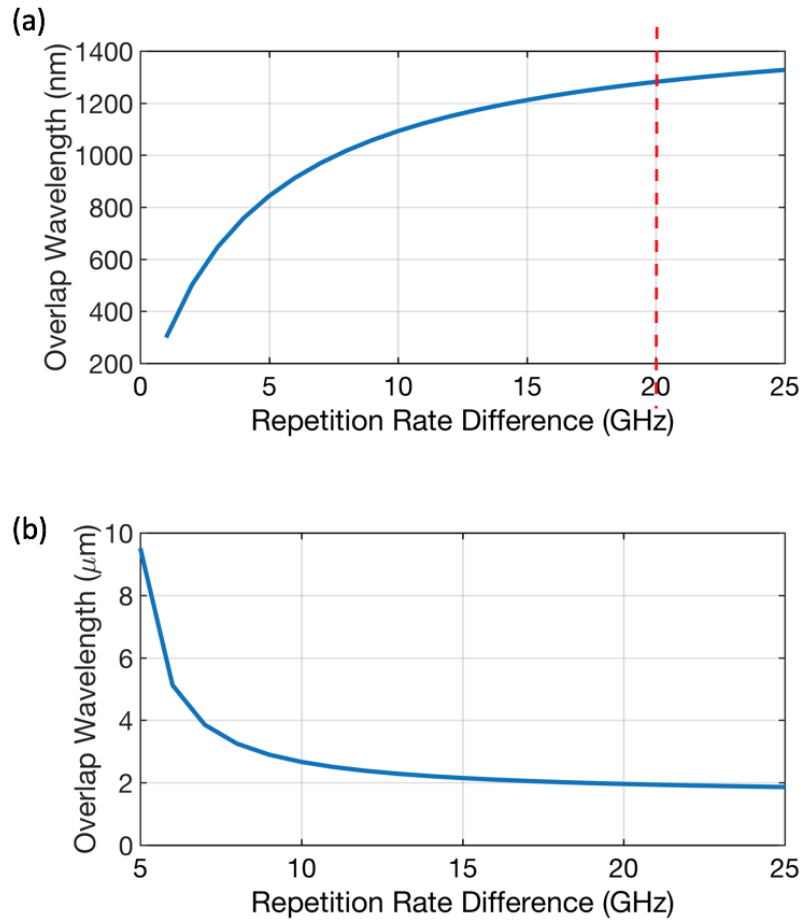


Figure 6.2. Repetition Rate Difference vs. Overlap Wavelength. The red dash line is the repetition rate we choose.

6.2 Device Design for Vernier Pairs

6.2.1 Requirements for Vernier Pairs

To resolve the repetition rate via Vernier scheme, we need to design two rings to meet the following requirements.

1. Ring 1 supports octave-spanning soliton generation
2. Ring 1 has low carrier offset frequency
3. Ring 2 supports broadband soliton generation (1200 nm to 2000 nm)
4. FSRs of the two rings exhibit 20 GHz offset
5. The overlap beat is less than 1.5 GHz
6. The resonance frequency of two rings are close to each other

The first two points are aiming at locking the f_{ceo} via f-2f self-referencing to fully stabilize the comb 1. The third to fifth points are requirements for a detectable overlap beat note. The fifth requirement is due to the bandwidth limitation of our current photodetector. The sixth point is to limit the tuning range of on-chip heater for better heater reliability and lower electric power usage. It is worth mentioning, the bandwidth of ring 2 is not required to span an octave.

The main ring is designed to support octave-spanning solitons generation via dispersion engineering as mentioned in Chapter 4.

We would focus on the design for the Vernier ring in this chapter.

6.2.2 Waveguide Dimension for Vernier Pairs

The Vernier ring (ring 2) design is based on the choice of octave-spanning ring (ring 1). For ring 2, the film thickness is chosen to be same as the film thickness of ring 1 to enable fabrication on the same wafer and homogeneous integration. We can use ring width and ring radius of ring 2 as the tuning knobs to meet other requirements.

Since the SiN Waveguide dimension of ring 2 also needs to support large bandwidth frequency comb generation. The ring width of ring 2 is chosen to be similar as the ring 1 to achieve broad bandwidth.

6.2.3 Ring Radius for Vernier Ring

As mentioned in Fig. 4.14, the theoretical resonance frequency and FSR can be calculated by Eq. 3.1 and Eq. 1.1 based on waveguide simulation.

Since the ring radius of ring 1 is optimized to achieve low offset frequency, the repetition rate of ring 1 is fixed. Then the repetition rate of ring 2 can only be within a certain range to provide 20 GHz beat note. In our case, we limit the df_{rep} to be within $\pm 1\%$ away from 20 GHz due to the limitation of an external locking cavity.

For a given waveguide dimension and ring radius of ring 1, the ring waveguide width and radius of ring 2 is optimized to satisfy the requirements mentioned in section 6.2.1.

For example, if we want to design an auxiliary ring for the ring 1 with a 738 nm thick and 1620 nm wide waveguide cross section. The ring radius of ring 1 is chosen to be 25.294 μm to attain low carrier offset frequency and the corresponding repetition rate is 892.567 GHz. Then the auxiliary ring FSR should be around 872.567 GHz. We sweep around this repetition rate to search a f_{rep2} to minimize the overlap beat frequency and find corresponding ring radius of ring 2.

The corresponding candidates are listed in Fig. 6.3 as Device 2 A to Device 2 C with different ring waveguide widths of ring 2. As shown in the Fig. 6.3, Device 2 A is the best candidate to meet all the requirements. So the radius of ring 2 is chosen as 25.868 μm and the ring waveguide width is 1580 nm.

6.3 Vernier Soliton Generation

Before we generate the soliton on the fabricated devices, we need to test the microheater reliability to ensure the feasibility of sharing common pump for two Vernier Solitons.

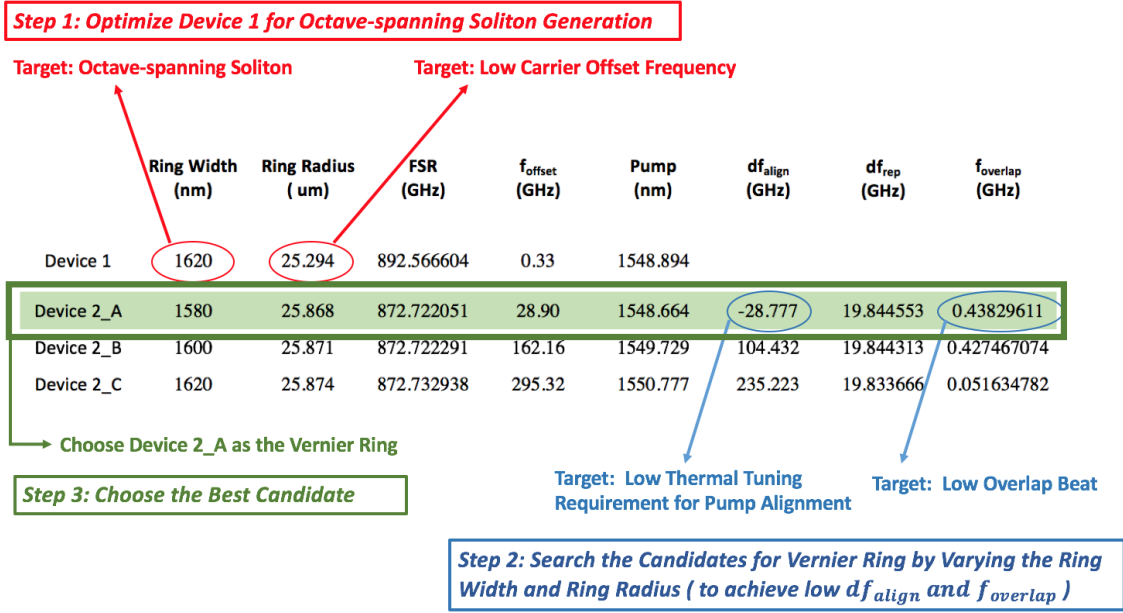


Figure 6.3. Choosing the Design Parameters of Vernier Pairs when Device 1 is chosen as $738 \text{ nm} \times 1620 \text{ nm}$. The device 1 is designed for octave-spanning soliton generation. The device 2 is designed for a corresponding Vernier ring.

6.3.1 Heater Parameters Characterization

The microheater is a 200 nm thin platinum layer deposited on top of microring as shown in Fig. 6.4. The design parameters and resistances are listed in Table 6.1. Wide ring heater width is to increase the maximum tolerant current by enlarging the heater cross section. Due to the temperature-dependent feature of Pt's resistance, the heater resistance is measured at different voltage applied to heater.

Table 6.1. Parameters of On-chip Heater

Heater Thickness	200 nm
Heater Width	$10 \mu\text{m}$
Heater Resistance (0 Volts)	19.9Ω
Heater Resistance (4.2 Volts)	30.9Ω

After testing the resistance of microheater, the reliability test is performed to avoid heater failure during the experimental demonstration. The resonance frequency is measured while

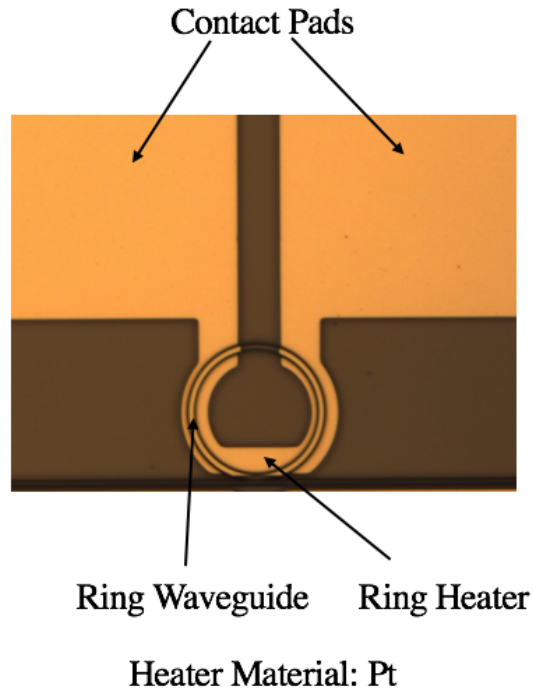


Figure 6.4. SiN Microring With Platinum Heater Fabricated by Zhichao Ye (Chalmers University of Technology)

linear transmission scan while the heater is applied with different DC voltage. The resonance frequency shift and corresponding electric power are recorded until heater failure.

For type I heater failure, which is immediately failure occurs after the resonance tuning over 1089 GHz with 730 mW electric power.

For type II heater failure, which is long term heating, the resonance can achieve 800 GHz shift with 530 mW electric power.

The heater testing indicates the upper bound of applied electric power during experiments. To protect heater, the electric power applied to the heater is kept below 300 mW. In the Vernier optical division demonstration, we applied around 170 mW to shift the resonance of the auxiliary ring about 250 GHz to pump simultaneously via a common pump.

6.3.2 Simultaneous Soliton Generation

Similar to the previous Chapter, the two microresonator is simultaneous pumped by a VCO controlled SSB modulated continuous-wave laser at ~ 1548.3 nm. After the combs (comb 1 and comb 2) are generated, a series of optical fiber circuits are served as filter and combiner to select the beat notes as shown in Fig. 6.5.

The upper part of experiment set-up diagram shows the measurement of the df_{rep} . The pump residues and the closet sidebands (+1 and -1 modes) are separated from both combs by the channel ports of CWDMs. A two by two optical fiber coupler is used to mix the sidebands from two Kerr solitons to provide df_{rep} beat signal. To avoid saturation of the photodetector, a waveshaper is used to suppress the pump signal. Then a fiber amplifier is used to provide enough power for photodetector.

The lower part of the experiment set-up show the detection of overlap beat and the verification of Vernier approach via EO modulation. The comb lines around overlap points are filtered out by the reflection port of CWDM and a $1.4 \mu\text{m}/1.5 \mu\text{m}$ WDM. The combined signal (via a two by two coupler) is then measured via a photodetector with a low noise amplifier.

To verify the Vernier measurement results, each Kerr comb is modulated via EO modulation to measure the repetition rate independently.

6.3.3 Measurement of Overlap Beat

The measurement results are shown in Fig. 6.6[69]. The main soliton (ring 1) has an octave-spanning spectrum covering 960 nm to 2080 nm. The spectrum of the auxiliary soliton (ring 2) is broad enough to observe two comb-line pairs overlapping at 1281 nm and 1956 nm, respectively. By detecting the beat between the first sideband pairs, we measure a frequency repetition difference δf_{rep} of 19.5 GHz. The beat note frequency at ~ 1281 nm is measured to be 466.67 MHz. The main comb repetition rate then is $f_{rep1} = 46 \cdot \delta f_{rep} \pm f_{overlap}$, which gives either 897.467 GHz or 896.533 GHz. The $M_2 = 46$ factor and the sign ambiguity (i.e. $\pm f_{overlap}$) can be determined from the optical spectra traces. Alternatively, they can be determined by detecting the beat frequency between the sideband pair adjacent to the

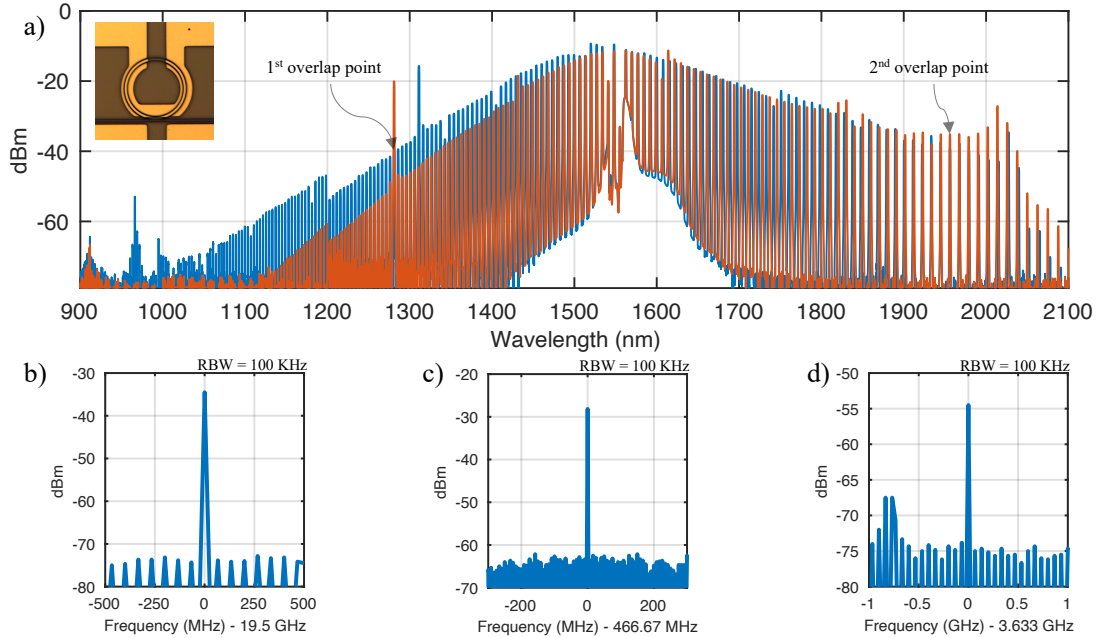


Figure 6.6. Measurement Results of Vernier Solitons. a) the optical spectra of two Vernier solitons (blue: comb 1, red: comb 2) b) electrical spectrum of df_{rep} . c) Electrical spectrum of the overlap beat d) Overlap beat of the EO comb verification[69]

6.4 Discussion

6.4.1 Comparison Between Two Optical Division Schemes

In chapter 5 and chapter 6, we discussed two approaches of optical division of a 900 GHz octave-spanning comb. These two approaches both use an auxiliary soliton on all-SiN platform and generate two solitons with a common pump. The differences are the repetition rate and comb bandwidth requirements of the auxiliary ring as shown in Fig. 6.7.

Device Preparation: For scheme I (see Fig. 6.7(a)), the requirements for fabrication is much higher than scheme 2 to achieve ultra low loss waveguide to reduce requirements for pump power. But there is no requirements for dispersion or particular ring radius for auxiliary. For scheme 2 (see Fig. 6.7(b)), the requirements for device design and fabrication of auxiliary ring are same as the main ring (octave-spanning device). But extra efforts of ring radius optimization are required to provide detectable beat signals.

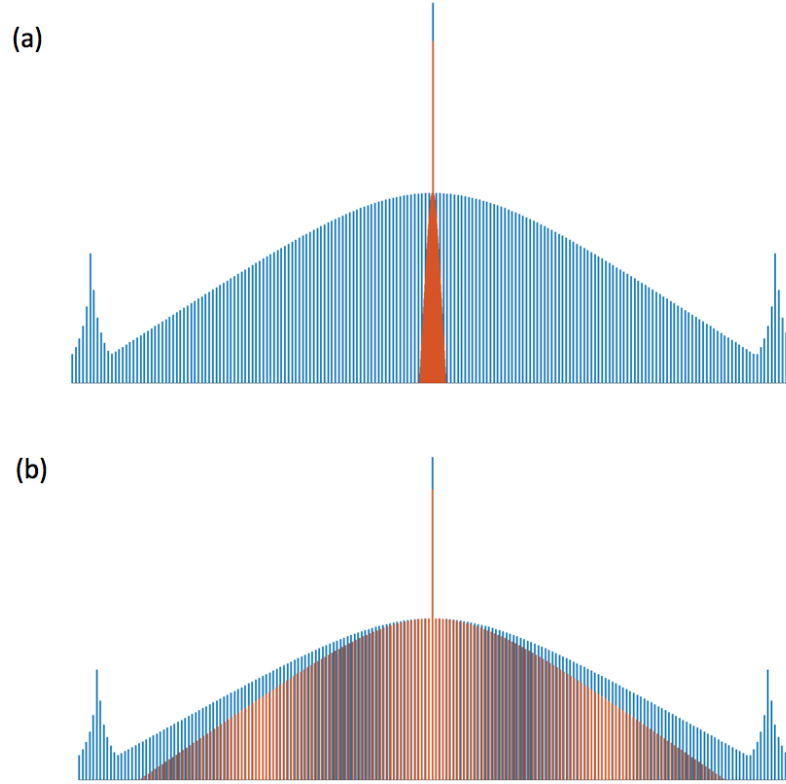


Figure 6.7. Two Schemes of Optical Division. a) Optical division with a low repetition rate narrow soliton. b) Optical division with a high repetition rate broadband soliton. Blue: Comb 1 (Octave-spanning Comb). Red: Comb 2 (Auxiliary Comb).

Simultaneous Soliton Generation: Both schemes using a fast pump sweeping method to achieve soliton generation. The CW pump is modulated by a SSB driven by a VCO. The VCO is controlled by a arbitrary waveform generate to set the sweep frequency. Due to the differences in the cavity quality factor and thermal coefficients between 900 GHz ring (~ 4 million Intrinsic Q) and 25 GHz ring (~ 16 million intrinsic Q), the optimization of sweep frequency to achieve common pump is harder for scheme 1 than scheme 2.

Beat Note Detection: since the beat note of scheme 1 is within C band, the power amplifier and fast photodetector are easy to find and provide enough power for the beat signal. However, for scheme 2, the overlap beat is either near 1280 nm or 2000 nm. The choice of measuring equipment is limited.

Overall, both optical division schemes have pros and cons. The selection is dependent on the availability of equipment and requirements of specific applications.

7. SUMMARY

7.1 Summary

In this thesis, we discuss the design and characterization of SiN microring resonators to achieve coherent frequency combs in both normal and anomalous dispersion regimes to fulfil the requirements of various applications.

The comb power conversion efficiency of normal dispersion dark pulse is investigated to meet the requirements of high optical power of individual comb lines and low pump power of on-chip coherent comb source for long-haul communications or RF filtering. Then we discussed the methods to generate breathing dark pulse to investigate the approach to avoid breather.

Then the thermo-optic effects in the SiN microring resonators are studied to provide a way of understanding and effectively taking advantage of the thermal tuning of a ring resonator. The thermal tuning can be used in on-chip integration to align a fixed wavelength laser pump frequency to a microring resonance frequency. Also, the thermal tuning can adjust the frequency comb repetition rate and offset frequency to meet the reach a target comb spacing or a small offset frequency for feedback locking. The experimental characterization of the microheater tuning efficiency is then discussed. To enable the long-term usage of microheater in the applications, we investigate the reliability of the microheater to find the limitation of on-chip thermal tuning.

Then we focus on the route towards a fully-stabilized frequency comb source by achieving octave-spanning solitons based on SiN microresonators. We used dispersion engineering to achieve 900 GHz repetition rate octave-spanning solitons. To enable the locking of high repetition rate, we demonstrated two approaches of on-chip optical division of the 900 GHz octave-spanning soliton on an all-SiN platform to pave a path on integrated stabilized frequency comb sources.

7.2 Outlook

We plan on realizing the fully stabilization of the generated octave-spanning solitons by locking both the repetition rate and carrier offset frequency simultaneously. A divided version of repetition rate of the 900 GHz octave-spanning soliton will be locked by the approaches discussed in the last two chapters. The carrier offset frequency will be locked via the $f-2f$ self-referencing approach.

The stabilized frequency comb can provide low-noise and stable frequencies components at desired wavelength with the flexibility enabled by thermal tuning.

REFERENCES

- [1] T. Udem, R. Holzwarth, and T. W. Hänsch, “Optical frequency metrology,” *Nature*, vol. 416, no. 6877, p. 233, 2002. DOI: <https://doi.org/10.1038/416233a>.
- [2] P. Del’aye, A. Schliesser, O. Arcizet, T. Wilken, R. Holzwarth, and T. J. Kippenberg, “Optical frequency comb generation from a monolithic microresonator,” *Nature*, vol. 450, no. 7173, pp. 1214–1217, 2007. DOI: <https://doi.org/10.1038/nature06401>.
- [3] S. A. Diddams, T. Udem, J. Bergquist, E. Curtis, R. Drullinger, L. Hollberg, W. M. Itano, W. Lee, C. Oates, K. Vogel, *et al.*, “An optical clock based on a single trapped $^{199}\text{Hg}^+$ ion,” *Science*, vol. 293, no. 5531, pp. 825–828, 2001. DOI: <https://doi.org/10.1126/science.1061171>.
- [4] A. Fülöp, M. Mazur, A. Lorences-Riesgo, T. A. Eriksson, P.-H. Wang, Y. Xuan, D. E. Leaird, M. Qi, P. A. Andrekson, A. M. Weiner, *et al.*, “Long-haul coherent communications using microresonator-based frequency combs,” *Optics Express*, vol. 25, no. 22, pp. 26 678–26 688, 2017. DOI: <https://doi.org/10.1364/OE.25.026678>.
- [5] J. Pfeifle, V. Brasch, M. Laueremann, Y. Yu, D. Wegner, T. Herr, K. Hartinger, P. Schindler, J. Li, D. Hillerkuss, *et al.*, “Coherent terabit communications with microresonator kerr frequency combs,” *Nature photonics*, vol. 8, no. 5, p. 375, 2014. DOI: <https://doi.org/10.1038/nphoton.2014.57>.
- [6] P. Marin-Palomo, J. N. Kemal, M. Karpov, A. Kordts, J. Pfeifle, M. H. Pfeiffer, P. Trocha, S. Wolf, V. Brasch, M. H. Anderson, *et al.*, “Microresonator-based solitons for massively parallel coherent optical communications,” *Nature*, vol. 546, no. 7657, p. 274, 2017. DOI: <https://doi.org/10.1038/nature22387>.
- [7] X. Xue, Y. Xuan, H.-J. Kim, J. Wang, D. E. Leaird, M. Qi, and A. M. Weiner, “Programmable single-bandpass photonic rf filter based on kerr comb from a microring,” *Journal of Lightwave Technology*, vol. 32, no. 20, pp. 3557–3565, 2014. DOI: <https://doi.org/10.1109/JLT.2014.2312359>.
- [8] V. Supradeepa, C. M. Long, R. Wu, F. Ferdous, E. Hamidi, D. E. Leaird, and A. M. Weiner, “Comb-based radiofrequency photonic filters with rapid tunability and high selectivity,” *Nature Photonics*, vol. 6, no. 3, p. 186, 2012. DOI: <https://doi.org/10.1038/nphoton.2011.350>.

- [9] P. Trocha, M. Karpov, D. Ganin, M. H. P. Pfeiffer, A. Kordts, S. Wolf, J. Krockenberger, P. Marin-Palomo, C. Weimann, S. Randel, W. Freude, T. J. Kippenberg, and C. Koos, “Ultrafast optical ranging using microresonator soliton frequency combs,” *Science*, vol. 359, no. 6378, pp. 887–891, 2018. DOI: [10.1126/science.aao3924](https://doi.org/10.1126/science.aao3924). eprint: <https://www.science.org/doi/pdf/10.1126/science.aao3924>. [Online]. Available: <https://www.science.org/doi/abs/10.1126/science.aao3924>.
- [10] M.-G. Suh and K. J. Vahala, “Soliton microcomb range measurement,” *Science*, vol. 359, no. 6378, pp. 884–887, 2018. DOI: [10.1126/science.aao1968](https://doi.org/10.1126/science.aao1968). eprint: <https://www.science.org/doi/pdf/10.1126/science.aao1968>. [Online]. Available: <https://www.science.org/doi/abs/10.1126/science.aao1968>.
- [11] D. J. Jones, S. A. Diddams, J. K. Ranka, A. Stentz, R. S. Windeler, J. L. Hall, and S. T. Cundiff, “Carrier-envelope phase control of femtosecond mode-locked lasers and direct optical frequency synthesis,” *Science*, vol. 288, no. 5466, pp. 635–639, 2000. DOI: <https://doi.org/10.1126/science.288.5466.635>.
- [12] D. E. Spence, P. N. Kean, and W. Sibbett, “60-fsec pulse generation from a self-mode-locked ti: Sapphire laser,” *Optics letters*, vol. 16, no. 1, pp. 42–44, 1991. DOI: <https://doi.org/10.1364/OL.16.000042>.
- [13] K. Tamura, E. Ippen, H. Haus, and L. Nelson, “77-fs pulse generation from a stretched-pulse mode-locked all-fiber ring laser,” *Optics letters*, vol. 18, no. 13, pp. 1080–1082, 1993. DOI: <https://doi.org/10.1364/OL.18.001080>.
- [14] Z. Sun, T. Hasan, F. Torrisi, D. Popa, G. Privitera, F. Wang, F. Bonaccorso, D. M. Basko, and A. C. Ferrari, “Graphene mode-locked ultrafast laser,” *ACS nano*, vol. 4, no. 2, pp. 803–810, 2010. DOI: <https://doi.org/10.1021/nn901703e>.
- [15] P. Grellu and N. Akhmediev, “Dissipative solitons for mode-locked lasers,” *Nature photonics*, vol. 6, no. 2, p. 84, 2012. DOI: <https://doi.org/10.1038/nphoton.2011.345>.
- [16] D. Armani, T. Kippenberg, S. Spillane, and K. Vahala, “Ultra-high-q toroid microcavity on a chip,” *Nature*, vol. 421, no. 6926, p. 925, 2003. DOI: <https://doi.org/10.1038/nature01371>.
- [17] M. Soltani, S. Yegnanarayanan, and A. Adibi, “Ultra-high q planar silicon microdisk resonators for chip-scale silicon photonics,” *Optics express*, vol. 15, no. 8, pp. 4694–4704, 2007. DOI: <https://doi.org/10.1364/OE.15.004694>.
- [18] H. Lee, T. Chen, J. Li, K. Y. Yang, S. Jeon, O. Painter, and K. J. Vahala, “Chemically etched ultrahigh-q wedge-resonator on a silicon chip,” *Nature Photonics*, vol. 6, no. 6, p. 369, 2012. DOI: <https://doi.org/10.1038/nphoton.2012.109>.

- [19] J. S. Levy, A. Gondarenko, M. A. Foster, A. C. Turner-Foster, A. L. Gaeta, and M. Lipson, “Cmos-compatible multiple-wavelength oscillator for on-chip optical interconnects,” *Nature photonics*, vol. 4, no. 1, p. 37, 2010. DOI: <https://doi.org/10.1038/nphoton.2009.259>.
- [20] A. G. Griffith, R. K. Lau, J. Cardenas, Y. Okawachi, A. Mohanty, R. Fain, Y. H. D. Lee, M. Yu, C. T. Phare, C. B. Poitras, *et al.*, “Silicon-chip mid-infrared frequency comb generation,” *Nature communications*, vol. 6, no. 1, pp. 1–5, 2015. DOI: <https://doi.org/10.1038/ncomms7299>.
- [21] Y. Wang, B. F. Jones, and D. Wang, “Early-career setback and future career impact,” *Nature communications*, vol. 10, no. 1, pp. 1–10, 2019. DOI: <https://doi.org/10.1038/s41467-019-08969-6>.
- [22] H. Jung, C. Xiong, K. Y. Fong, X. Zhang, and H. X. Tang, “Optical frequency comb generation from aluminum nitride microring resonator,” *Optics letters*, vol. 38, no. 15, pp. 2810–2813, 2013. DOI: <https://doi.org/10.1364/OL.38.002810>.
- [23] Y. Xuan, Y. Liu, L. T. Varghese, A. J. Metcalf, X. Xue, P.-H. Wang, K. Han, J. A. Jaramillo-Villegas, A. Al Noman, C. Wang, *et al.*, “High-q silicon nitride microresonators exhibiting low-power frequency comb initiation,” *Optica*, vol. 3, no. 11, pp. 1171–1180, 2016. DOI: <https://doi.org/10.1364/OPTICA.3.001171>.
- [24] A. S. Raja, A. S. Voloshin, H. Guo, S. E. Agafonova, J. Liu, A. S. Gorodnitskiy, M. Karpov, N. G. Pavlov, E. Lucas, R. R. Galiev, *et al.*, “Electrically pumped photonic integrated soliton microcomb,” *Nature communications*, vol. 10, no. 1, pp. 1–8, 2019. DOI: <https://doi.org/10.1038/s41467-019-08498-2>.
- [25] Z. Ye, K. Twayana, P. A. Andrekson, *et al.*, “High-q Si_3N_4 microresonators based on a subtractive processing for kerr nonlinear optics,” *Optics express*, vol. 27, no. 24, pp. 35 719–35 727, 2019. DOI: <https://doi.org/10.1364/OE.27.035719>.
- [26] X. Ji, S. Roberts, M. Corato-Zanarella, and M. Lipson, “Methods to achieve ultra-high quality factor silicon nitride resonators,” *APL Photonics*, vol. 6, no. 7, p. 071 101, 2021. DOI: [10.1063/5.0057881](https://doi.org/10.1063/5.0057881). eprint: <https://doi.org/10.1063/5.0057881>. [Online]. Available: <https://doi.org/10.1063/5.0057881>.
- [27] C. Bao, Y. Xuan, D. E. Leaird, S. Wabnitz, M. Qi, and A. M. Weiner, “Spatial mode-interaction induced single soliton generation in microresonators,” *Optica*, vol. 4, no. 9, pp. 1011–1015, Sep. 2017. DOI: [10.1364/OPTICA.4.001011](https://doi.org/10.1364/OPTICA.4.001011). [Online]. Available: <http://www.osapublishing.org/optica/abstract.cfm?URI=optica-4-9-1011>.
- [28] A. Weiner, *Ultrafast optics*. John Wiley & Sons, 2011, vol. 72, ISBN: 978-0-4714-1539-8.

- [29] F. Ferdous, H. Miao, D. E. Leaird, K. Srinivasan, J. Wang, L. Chen, L. T. Varghese, and A. M. Weiner, “Spectral line-by-line pulse shaping of on-chip microresonator frequency combs,” *Nature Photonics*, vol. 5, no. 12, pp. 770–776, 2011. DOI: <https://doi.org/10.1038/nphoton.2011.255>.
- [30] A. B. Matsko, A. A. Savchenkov, V. S. Ilchenko, D. Seidel, and L. Maleki, “Hard and soft excitation regimes of kerr frequency combs,” *Phys. Rev. A*, vol. 85, p. 023830, 2 Feb. 2012. DOI: [10.1103/PhysRevA.85.023830](https://doi.org/10.1103/PhysRevA.85.023830). [Online]. Available: <https://link.aps.org/doi/10.1103/PhysRevA.85.023830>.
- [31] Y. Liu, Y. Xuan, X. Xue, P.-H. Wang, S. Chen, A. J. Metcalf, J. Wang, D. E. Leaird, M. Qi, and A. M. Weiner, “Investigation of mode coupling in normal-dispersion silicon nitride microresonators for kerr frequency comb generation,” *optica*, vol. 1, no. 3, pp. 137–144, 2014. DOI: <https://doi.org/10.1364/OPTICA.1.000137>.
- [32] S.-P. Yu, E. Lucas, J. Zang, and S. B. Papp, “Dark- and bright-pulse states in photonic crystal ring resonators,” in *Conference on Lasers and Electro-Optics*, Optical Society of America, 2021, FTu4E.7. DOI: [10.1364/CLEO_QELS.2021.FTu4E.7](https://doi.org/10.1364/CLEO_QELS.2021.FTu4E.7). [Online]. Available: http://www.osapublishing.org/abstract.cfm?URI=CLEO_QELS-2021-FTu4E.7.
- [33] W. Liang, A. A. Savchenkov, V. S. Ilchenko, D. Eliyahu, D. Seidel, A. B. Matsko, and L. Maleki, “Generation of a coherent near-infrared kerr frequency comb in a monolithic microresonator with normal gvd,” *Opt. Lett.*, vol. 39, no. 10, pp. 2920–2923, May 2014. DOI: [10.1364/OL.39.002920](https://doi.org/10.1364/OL.39.002920). [Online]. Available: <http://www.osapublishing.org/ol/abstract.cfm?URI=ol-39-10-2920>.
- [34] S. Coen, H. G. Randle, T. Sylvestre, and M. Erkintalo, “Modeling of octave-spanning kerr frequency combs using a generalized mean-field lugiato-lefever model,” *Opt. Lett.*, vol. 38, no. 1, pp. 37–39, Jan. 2013. DOI: [10.1364/OL.38.000037](https://doi.org/10.1364/OL.38.000037). [Online]. Available: <http://www.osapublishing.org/ol/abstract.cfm?URI=ol-38-1-37>.
- [35] T. Herr, V. Brasch, J. D. Jost, C. Y. Wang, N. M. Kondratiev, M. L. Gorodetsky, and T. J. Kippenberg, “Temporal solitons in optical microresonators,” *Nature Photonics*, vol. 8, no. 2, p. 145, 2014. DOI: <https://doi.org/10.1038/nphoton.2013.343>.
- [36] P.-H. Wang, J. A. Jaramillo-Villegas, Y. Xuan, X. Xue, C. Bao, D. E. Leaird, M. Qi, and A. M. Weiner, “Intracavity characterization of micro-comb generation in the single-soliton regime,” *Optics express*, vol. 24, no. 10, pp. 10890–10897, 2016. DOI: <https://doi.org/10.1364/OE.24.010890>.
- [37] X. Yi, Q.-F. Yang, K. Y. Yang, M.-G. Suh, and K. Vahala, “Soliton frequency comb at microwave rates in a high-q silica microresonator,” *Optica*, vol. 2, no. 12, pp. 1078–1085, 2015. DOI: <https://doi.org/10.1364/OPTICA.2.001078>.

- [38] M. Yu, Y. Okawachi, A. G. Griffith, M. Lipson, and A. L. Gaeta, “Mode-locked mid-infrared frequency combs in a silicon microresonator,” *Optica*, vol. 3, no. 8, pp. 854–860, 2016. DOI: <https://doi.org/10.1364/OPTICA.3.000854>.
- [39] M. H. P. Pfeiffer, A. Kordts, V. Brasch, M. Zervas, M. Geiselmann, J. D. Jost, and T. J. Kippenberg, “Photonic damascene process for integrated high-q microresonator based nonlinear photonics,” *Optica*, vol. 3, no. 1, pp. 20–25, Jan. 2016. DOI: [10.1364/OPTICA.3.000020](https://doi.org/10.1364/OPTICA.3.000020). [Online]. Available: <http://www.osapublishing.org/optica/abstract.cfm?URI=optica-3-1-20>.
- [40] C. Wang, C. Bao, Y. Xuan, K. Han, D. E. Leaird, M. Qi, and A. M. Weiner, “Normal dispersion high conversion efficiency kerr comb with 50 ghz repetition rate,” in *CLEO: Science and Innovations*, 2017, SW4N–5. DOI: https://doi.org/10.1364/CLEO_SI.2017.SW4N.5.
- [41] M. Xue, “Chemical and biomedical sensors using two dimensional materials,” Masters of Science in Electrical Engineering and Computer Science, Sep. 2019. [Online]. Available: <https://dspace.mit.edu/handle/1721.1/124282>.
- [42] B. Y. Kim, Y. Okawachi, J. K. Jang, M. Yu, X. Ji, Y. Zhao, C. Joshi, M. Lipson, and A. L. Gaeta, “Turn-key, high-efficiency kerr comb source,” *Opt. Lett.*, vol. 44, no. 18, pp. 4475–4478, Sep. 2019. DOI: [10.1364/OL.44.004475](https://doi.org/10.1364/OL.44.004475). [Online]. Available: <http://www.osapublishing.org/ol/abstract.cfm?URI=ol-44-18-4475>.
- [43] X. Xue, P.-H. Wang, Y. Xuan, M. Qi, and A. M. Weiner, “Microresonator kerr frequency combs with high conversion efficiency,” *Laser & Photonics Reviews*, vol. 11, no. 1, p. 1 600 276, 2017. DOI: <https://doi.org/10.1002/lpor.201600276>.
- [44] Ó. B. Helgason, Z. Ye, K. Twayana, P. A. Andrekson, J. Schröder, and V. Torres-Company, “Dark-pulse kerr combs in linearly coupled microring structures,” in *2020 Conference on Lasers and Electro-Optics (CLEO)*, 2020, pp. 1–2.
- [45] S. Ramelow, A. Farsi, S. Clemmen, J. S. Levy, A. R. Johnson, Y. Okawachi, M. R. E. Lamont, M. Lipson, and A. L. Gaeta, “Strong polarization mode coupling in microresonators,” *Opt. Lett.*, vol. 39, no. 17, pp. 5134–5137, Sep. 2014. DOI: [10.1364/OL.39.005134](https://doi.org/10.1364/OL.39.005134). [Online]. Available: <http://www.osapublishing.org/ol/abstract.cfm?URI=ol-39-17-5134>.
- [46] T. Herr, V. Brasch, J. D. Jost, I. Mirgorodskiy, G. Lihachev, M. L. Gorodetsky, and T. J. Kippenberg, “Mode spectrum and temporal soliton formation in optical microresonators,” *Phys. Rev. Lett.*, vol. 113, p. 123 901, 12 Sep. 2014. DOI: [10.1103/PhysRevLett.113.123901](https://doi.org/10.1103/PhysRevLett.113.123901). [Online]. Available: <https://link.aps.org/doi/10.1103/PhysRevLett.113.123901>.

- [47] C. Bao, J. A. Jaramillo-Villegas, Y. Xuan, D. E. Leaird, M. Qi, and A. M. Weiner, “Observation of fermi-pasta-ulam recurrence induced by breather solitons in an optical microresonator,” *Phys. Rev. Lett.*, vol. 117, p. 163 901, 16 Oct. 2016. DOI: [10.1103/PhysRevLett.117.163901](https://doi.org/10.1103/PhysRevLett.117.163901). [Online]. Available: <https://link.aps.org/doi/10.1103/PhysRevLett.117.163901>.
- [48] M. Yu, J. K. Jang, Y. Okawachi, A. G. Griffith, K. Luke, S. A. Miller, X. Ji, M. Lipson, and A. L. Gaeta, “Breather soliton dynamics in microresonators,” *Nature communications*, vol. 8, p. 14 569, 2017. DOI: <https://doi.org/10.1038/ncomms14569>.
- [49] E. Lucas, M. Karpov, H. Guo, M. Gorodetsky, and T. Kippenberg, “Breathing dissipative solitons in optical microresonators,” *Nature communications*, vol. 8, no. 1, p. 736, 2017. DOI: <https://doi.org/10.1038/s41467-017-00719-w>.
- [50] C. Bao, Y. Xuan, C. Wang, A. Fülöp, D. E. Leaird, V. Torres-Company, M. Qi, and A. M. Weiner, “Observation of breathing dark pulses in normal dispersion optical microresonators,” *Phys. Rev. Lett.*, vol. 121, p. 257 401, 25 Dec. 2018. DOI: [10.1103/PhysRevLett.121.257401](https://doi.org/10.1103/PhysRevLett.121.257401). [Online]. Available: <https://link.aps.org/doi/10.1103/PhysRevLett.121.257401>.
- [51] X. Xue, Y. Xuan, C. Wang, P.-H. Wang, Y. Liu, B. Niu, D. E. Leaird, M. Qi, and A. M. Weiner, “Thermal tuning of kerr frequency combs in silicon nitride microring resonators,” *Optics express*, vol. 24, no. 1, pp. 687–698, 2016. DOI: <https://doi.org/10.1364/OE.24.000687>.
- [52] C.-L. Tien and T.-W. Lin, “Thermal expansion coefficient and thermomechanical properties of SiN_x thin films prepared by plasma-enhanced chemical vapor deposition,” *Appl. Opt.*, vol. 51, no. 30, pp. 7229–7235, Oct. 2012. DOI: [10.1364/AO.51.007229](https://doi.org/10.1364/AO.51.007229). [Online]. Available: <http://www.osapublishing.org/ao/abstract.cfm?URI=ao-51-30-7229>.
- [53] A. Arbabi and L. L. Goddard, “Measurements of the refractive indices and thermo-optic coefficients of Si_3N_4 and SiO_x using microring resonances,” *Opt. Lett.*, vol. 38, no. 19, pp. 3878–3881, Oct. 2013. DOI: [10.1364/OL.38.003878](https://doi.org/10.1364/OL.38.003878). [Online]. Available: <http://www.osapublishing.org/ol/abstract.cfm?URI=ol-38-19-3878>.
- [54] S. G. Johnson and J. D. Joannopoulos, “Block-iterative frequency-domain methods for maxwell’s equations in a planewave basis,” *Opt. Express*, vol. 8, no. 3, pp. 173–190, Jan. 2001. DOI: [10.1364/OE.8.000173](https://doi.org/10.1364/OE.8.000173). [Online]. Available: <http://www.osapublishing.org/oe/abstract.cfm?URI=oe-8-3-173>.
- [55] C. M. Herzinger, B. Johs, W. A. McGahan, J. A. Woollam, and W. Paulson, “Ellipsometric determination of optical constants for silicon and thermally grown silicon dioxide via a multi-sample, multi-wavelength, multi-angle investigation,” *Journal of Applied Physics*, vol. 83, no. 6, pp. 3323–3336, 1998. DOI: [10.1063/1.367101](https://doi.org/10.1063/1.367101). eprint: <https://doi.org/10.1063/1.367101>. [Online]. Available: <https://doi.org/10.1063/1.367101>.

- [56] M.-G. Suh, Q.-F. Yang, K. Y. Yang, X. Yi, and K. J. Vahala, “Microresonator soliton dual-comb spectroscopy,” *Science*, vol. 354, no. 6312, pp. 600–603, 2016. DOI: [10.1126/science.aah6516](https://doi.org/10.1126/science.aah6516). eprint: <https://www.science.org/doi/pdf/10.1126/science.aah6516>. [Online]. Available: <https://www.science.org/doi/abs/10.1126/science.aah6516>.
- [57] Y. Okawachi, K. Saha, J. S. Levy, Y. H. Wen, M. Lipson, and A. L. Gaeta, “Octave-spanning frequency comb generation in a silicon nitride chip,” *Opt. Lett.*, vol. 36, no. 17, pp. 3398–3400, Sep. 2011. DOI: [10.1364/OL.36.003398](https://doi.org/10.1364/OL.36.003398). [Online]. Available: <http://www.osapublishing.org/ol/abstract.cfm?URI=ol-36-17-3398>.
- [58] Q. Li, T. C. Briles, D. A. Westly, T. E. Drake, J. R. Stone, B. R. Ilic, S. A. Diddams, S. B. Papp, and K. Srinivasan, “Stably accessing octave-spanning microresonator frequency combs in the soliton regime,” *Optica*, vol. 4, no. 2, pp. 193–203, Feb. 2017. DOI: [10.1364/OPTICA.4.000193](https://doi.org/10.1364/OPTICA.4.000193). [Online]. Available: <http://www.osapublishing.org/optica/abstract.cfm?URI=optica-4-2-193>.
- [59] M. H. P. Pfeiffer, C. Herkommer, J. Liu, H. Guo, M. Karpov, E. Lucas, M. Zervas, and T. J. Kippenberg, “Octave-spanning dissipative kerr soliton frequency combs in si₃n₄ microresonators,” *Optica*, vol. 4, no. 7, pp. 684–691, Jul. 2017. DOI: [10.1364/OPTICA.4.000684](https://doi.org/10.1364/OPTICA.4.000684). [Online]. Available: <http://www.osapublishing.org/optica/abstract.cfm?URI=optica-4-7-684>.
- [60] S.-P. Yu, T. C. Briles, G. T. Moille, X. Lu, S. A. Diddams, K. Srinivasan, and S. B. Papp, “Tuning kerr-soliton frequency combs to atomic resonances,” *Phys. Rev. Applied*, vol. 11, p. 044017, 4 Apr. 2019. DOI: [10.1103/PhysRevApplied.11.044017](https://doi.org/10.1103/PhysRevApplied.11.044017). [Online]. Available: <https://link.aps.org/doi/10.1103/PhysRevApplied.11.044017>.
- [61] D. T. Spencer, T. Drake, T. C. Briles, J. Stone, L. C. Sinclair, C. Fredrick, Q. Li, D. Westly, B. R. Ilic, A. Bluestone, *et al.*, “An optical-frequency synthesizer using integrated photonics,” *Nature*, vol. 557, no. 7703, pp. 81–85, 2018. DOI: [10.1038/s41586-018-0065-7](https://doi.org/10.1038/s41586-018-0065-7).
- [62] S. Coen and M. Erkintalo, “Universal scaling laws of kerr frequency combs,” *Optics letters*, vol. 38, no. 11, pp. 1790–1792, 2013. DOI: <https://doi.org/10.1364/OL.38.001790>.
- [63] G. Moille, Q. Li, T. C. Briles, S.-P. Yu, T. Drake, X. Lu, A. Rao, D. Westly, S. B. Papp, and K. Srinivasan, “Broadband resonator-waveguide coupling for efficient extraction of octave-spanning microcombs,” *Opt. Lett.*, vol. 44, no. 19, pp. 4737–4740, Oct. 2019. DOI: [10.1364/OL.44.004737](https://doi.org/10.1364/OL.44.004737). [Online]. Available: <http://www.osapublishing.org/ol/abstract.cfm?URI=ol-44-19-4737>.
- [64] T. C. Briles, J. R. Stone, T. E. Drake, D. T. Spencer, C. Frederick, Q. Li, D. A. Westly, B. R. Ilic, K. Srinivasan, S. A. Diddams, *et al.*, “Kerr-microresonator solitons for accurate carrier-envelope-frequency stabilization,” *arXiv preprint arXiv:1711.06251*, 2017.

- [65] C. Wang, N. P. O'Malley, Z. Ye, M. S. Alshaykh, M. Girardi, A. A. Noman, D. E. Leaird, M. Qi, V. Torres-Company, and A. M. Weiner, "Optical division of an octave-spanning comb on an all-silicon nitride platform," in *2021 IEEE Photonics Conference (IPC)*, 2021, pp. 1–2. DOI: [10.1109/IPC48725.2021.9592941](https://doi.org/10.1109/IPC48725.2021.9592941).
- [66] Z. L. Newman, V. Maurice, T. Drake, J. R. Stone, T. C. Briles, D. T. Spencer, C. Fredrick, Q. Li, D. Westly, B. R. Ilic, *et al.*, "Architecture for the photonic integration of an optical atomic clock," *Optica*, vol. 6, no. 5, pp. 680–685, 2019. DOI: <https://doi.org/10.1364/OPTICA.6.000680>.
- [67] Z. Ye, F. Lei, K. Twayana, M. Girardi, P. A. Andrekson, and V. Torres-Company, "Integrated, ultra-compact high-q silicon nitride microresonators for low-repetition-rate soliton microcombs," *arXiv preprint arXiv:2108.07495*, 2021.
- [68] Z. Ye, F. Lei, K. Twayana, M. Girardi, P. A. Andrekson, *et al.*, "25 ghz soliton microcombs in high-q si3n4 racetrack-shaped microresonators," in *CLEO: QELS_Fundamental Science*, 2020, JTh2F–29. DOI: https://doi.org/10.1364/CLEO_AT.2020.JTh2F.29.
- [69] M. S. Alshaykh, C. Wang, N. P. O alley, Z. Ye, A. Al Noman, D. E. Leaird, M. Qi, A. M. Weiner, *et al.*, "Optical dual-comb vernier division of an octave-spanning kerr microcomb," in *CLEO: Science and Innovations*, 2021, SW2H–7. DOI: https://doi.org/10.1364/CLEO_SI.2021.SW2H.7.
- [70] A. Metcalf, F. Quinlan, T. M. Fortier, S. A. Diddams, and A. M. Weiner, "Broadly tunable, low timing jitter, high repetition rate optoelectronic comb generator," *Electronics letters*, vol. 51, no. 20, pp. 1596–1598, 2015. DOI: <https://doi.org/10.1049/el.2015.1367>.

PUBLICATIONS

1. Xue, Xiaoxiao, Yi Xuan, Cong Wang, Pei-Hsun Wang, Yang Liu, Ben Niu, Daniel E. Leaird, Minghao Qi, and Andrew M. Weiner. "Thermal tuning of Kerr frequency combs in silicon nitride microring resonators." *Optics express* 24, no. 1 (2016): 687-698.
2. Xue, Xiaoxiao, Yi Xuan, Cong Wang, Pei-Hsun Wang, Yang Liu, Daniel E. Leaird, Minghao Qi, and Andrew M. Weiner. "Offset frequency tuning of a microcomb with an integrated microheater." In *2016 Conference on Lasers and Electro-Optics (CLEO)*, pp. 1-2. IEEE, 2016.
3. Xue, Xiaoxiao, Yi Xuan, Pei-Hsun Wang, Yang Liu, Jose A. Jaramillo-Villegas, Cong Wang, Daniel E. Leaird, Minghao Qi, and Andrew M. Weiner. "Reciprocal waveforms at through and drop ports in microcomb generation." In *CLEO: Science and Innovations*, pp. SM4I-5. Optical Society of America, 2016.
4. Kim, Sangsik, Kyunghun Han, Cong Wang, Jose A. Jaramillo-Villegas, Xiaoxiao Xue, Yi Xuan, Andrew M. Weiner, and Minghao Qi. "Frequency comb generation in 300 nm-thick Si₃N₄ concentric-ring-resonators." In *Integrated Photonics Research, Silicon and Nanophotonics*, pp. IM2A-3. Optical Society of America, 2016.
5. Jaramillo-Villegas, Jose A., Cong Wang, Pei-Hsun Wang, Chengying Bao, Yi Xuan, Kyunghun Han, Daniel E. Leaird, Minghao Qi, and Andrew M. Weiner. "Experimental characterization of pump power and detuning in microresonator frequency combs." In *Latin America Optics and Photonics Conference*, pp. LTh3B-2. Optical Society of America, 2016.
6. Xuan, Yi, Yang Liu, Leo T. Varghese, Andrew J. Metcalf, Xiaoxiao Xue, Pei-Hsun Wang, Kyunghun Han, Jaramillo-Villegas, Jose A., Abdullah Al Noman, Cong Wang, Sangsik Kim, Min Teng, Yun Jo Lee, Ben Niu, Li Fan, Jian Wang, Daniel E. Leaird, Andrew M. Weiner, and Minghao Qi. "High-Q silicon nitride microresonators exhibiting low-power frequency comb initiation." *Optica* 3, no. 11 (2016): 1171-1180

7. Bao, Chengying, Yi Xuan, Cong Wang, Jose A. Jaramillo-Villegas, Daniel E. Leaird, Minghao Qi, and Andrew M. Weiner. "Soliton repetition rate in a silicon-nitride microresonator." *Optics letters* 42, no. 4 (2017): 759-762.
8. Wang, Cong, Chengying Bao, Yi Xuan, Kyunghun Han, Daniel E. Leaird, Minghao Qi, and Andrew M. Weiner. "Normal dispersion high conversion efficiency Kerr comb with 50 GHz repetition rate." In *CLEO: Science and Innovations*, pp. SW4N-5. Optical Society of America, 2017.
9. Bao, Chengying, Yi Xuan, Cong Wang, Jose A. Jaramillo-Villega, Daniel E. Leaird, Minghao Qi, and Andrew M. Weiner. "Dispersion immune change of soliton repetition rate in a silicon-nitride microresonator." In *CLEO: Science and Innovations*, pp. JTh2A-120. Optical Society of America, 2017.
10. Kim, Sangsik, Kyunghun Han, Cong Wang, Jose A. Jaramillo-Villegas, Xiaoxiao Xue, Chengying Bao, Yi Xuan, Daniel E. Leaird, Andrew M. Weiner, and Minghao Qi. "Dispersion engineering and frequency comb generation in thin silicon nitride concentric microresonators." *Nature communications* 8, no. 1 (2017): 1-8.
11. McKinzie, Keith A., Cong Wang, Abdullah Al Noman, David L. Mathine, Kyunghun Han, Daniel E. Leaird, Maria Anagnosti et al. "Heterogeneously integrated InP widely tunable laser and SiN microring resonator for integrated comb generation." In *2018 Conference on Lasers and Electro-Optics (CLEO)*, pp. 1-2. IEEE, 2018.
12. Bao, Chengying, Yi Xuan, Cong Wang, Attila Fülöp, Daniel E. Leaird, Minghao Qi, and Andrew M. Weiner. "Observation of breathing dark pulses in normal dispersion optical microresonators." *Physical review letters* 121, no. 25 (2018): 257401.
13. Kong, Ziyun, Chengying Bao, Oscar E. Sandoval, Bohao Liu, Cong Wang, Jose A. Jaramillo-Villegas, Minghao Qi, and Andrew M. Weiner. "Characterizing pump line phase offset of a single-soliton Kerr comb by dual comb interferometry." *Optics letters* 44, no. 6 (2019): 1460-1463.

14. McKinzie, Keith A., Cong Wang, Abdullah Al Noman, David L. Mathine, Kyunghun Han, Daniel E. Leaird, Gloria E. Hoefler et al. "InP high power monolithically integrated widely tunable laser and SOA array for hybrid integration." *Optics Express* 29, no. 3 (2021): 3490-3502.
15. Alshaykh, Mohammed S., Cong Wang, Nathan P. O'Malley, Zhichao Ye, Abdullah Al Noman, Daniel E. Leaird, Minghao Qi, and Andrew M. Weiner. "Optical Dual-Comb Vernier Division of an Octave-Spanning Kerr Microcomb." In *CLEO: Science and Innovations*, pp. SW2H-7. Optical Society of America, 2021.
16. Cong Wang, Nathan P. O'Malley, Zhichao Ye, Alshaykh, Mohammed S., Marcello Girardi, Abdullah Al Noman, Daniel E. Leaird, Minghao Qi, and Andrew M. Weiner, "Optical Division of an Octave-Spanning Comb on an All-Silicon Nitride Platform", accepted for IEEE Photonic Conference (IPC), 2021.